Spring 2008

Analysis and Application of Perfectly Matched Layer Absorbing Boundary Conditions for Computational Aeroacoustics

Sarah Anne Parrish
Old Dominion University

ANALYSIS AND APPLICATION OF PERFECTLY MATCHED LAYER ABSORBING BOUNDARY CONDITIONS FOR COMPUTATIONAL AEROACOUSTICS

by

Sarah Anne Parrish
B.S. May 2004, Old Dominion University
M.S. December 2005, Old Dominion University

A Dissertation Submitted to the Faculty of
Old Dominion University in Partial Fulfillment of the
Requirement for the Degree of

DOCTOR OF PHILOSOPHY

MATHEMATICS AND STATISTICS

OLD DOMINION UNIVERSITY
May 2008

Approved by:

Fang Q. Hu (Director)

Oktay Baysal (Member)

D. Glenn Lasseigne (Member)

Li-Shi Luo (Member)

Ruhai Zhou (Member)

ABSTRACT

ANALYSIS AND APPLICATION OF PERFECTLY MATCHED LAYER ABSORBING BOUNDARY CONDITIONS FOR COMPUTATIONAL AEROACOUSTICS

Sarah Anne Parrish
Old Dominion University, 2008
Director: Dr. Fang Q. Hu

The Perfectly Matched Layer (PML) was originally proposed by Berenger as an absorbing boundary condition for Maxwell's equations in 1994 and is still used extensively in the field of electromagnetics. The idea was extended to Computational Aeroacoustics in 1996, when Hu applied the method to Euler's equations. Since that time much of the work done on PML in the field of acoustics has been specific to the case where mean flow is perpendicular to a boundary, with an emphasis on Cartesian coordinates. The goal of this work is to further extend the PML methodology in a two-fold manner: First, to handle the more general case of an oblique mean flow, where mean velocities strike the boundary at an arbitrary angle, and second, to adapt the equations for use in a cylindrical coordinate system. These extensions to the PML methodology are effectively carried out in this dissertation. Perfectly Matched Layer absorbing boundary conditions are presented for the linearized and nonlinear Euler equations in two dimensions. Such boundary conditions are presented in both Cartesian and cylindrical coordinates for the case of an oblique mean flow. In Cartesian coordinates, the PML equations for the side layers and corner layers of a rectangular domain will be derived independently. The approach used in the formation of side layer equations guarantees that the side layers will be perfectly matched at the interface between the interior and PML regions. Because of the perfect matching of the side layers, the equations are guaranteed to be stable. However, a somewhat different approach is used in the formation of the corner layer equations. Therefore, the stability of linear waves in the corner layer is analyzed. The results of the analysis indicate that the proposed corner equations are indeed stable. For the PML equations in cylindrical coordinates, there is no need for separate derivations of side and corner layers, and in this case, the stability of the equations is achieved

through an appropriate space-time transformation. As is shown, such a transformation is needed for correcting the inconsistencies in phase and group velocities which can negatively affect the stability of the equations. After this correction has been made, the cylindrical PML can be implemented without risk of instability. In both Cartesian and cylindrical coordinates, the PML for the linearized Euler equations are presented in primitive variables, while conservation form is used for the nonlinear Euler equations. Numerical examples are also included to support the validity of the proposed equations. Specifically, the equations are tested for a combination of acoustic, vorticity and entropy waves. In each example, high-accuracy solutions are obtained, indicating that the PML conditions are effective in minimizing boundary reflections.

ACKNOWLEDGMENTS

A special thanks to the members of my dissertation committee for their willingness to serve and for contributing their valuable time and input. In particular, thanks to my advisor, Dr. Hu, for all the years of guidance and encouragement. Thanks to the National Science Foundation for their financial support of this work (DMS-0411402). To my family, thanks for all your love and support throughout the years and for always being there when I needed you. Thank you, Lord, for giving me wisdom and for blessing the work of my hands.

TABLE OF CONTENTS

Page

LIST OF FIGURES viii

CHAPTERS

I INTRODUCTION 1
II THE PERFECTLY MATCHED LAYER (PML) METHOD 6
II.1 INTRODUCTION TO PERFECTLY MATCHED LAYERS 6
II.2 THE IMPORTANCE OF DISPERSION RELATIONS 8
II.2.1 ONE-DIMENSIONAL MEAN FLOW 8
II.2.2 TWO-DIMENSIONAL MEAN FLOW 11
III PML IN CARTESIAN COORDINATES FOR OBLIQUE MEAN FLOW 15
III.1 LINEARIZED EULER EQUATIONS 15
III.1.1 PROPOSED PML EQUATIONS 15
III.1.2 THE STABILITY OF CORNER LAYERS 19
III.1.3 NUMERICAL EXAMPLES 22
III.2 NONLINEAR EULER EQUATIONS 27
III.2.1 DERIVATION OF PML EQUATIONS 27
III.2.2 STABILITY ANALYSIS FOR CORNER LAYERS 30
III.2.3 NUMERICAL EXAMPLES 33
IV PML IN CYLINDRICAL COORDINATES 48
IV.1 NONLINEAR EULER EQUATIONS IN CONSERVATION FORM . 48
IV.1.1 PML FORMULATION 48
IV.1.2 NUMERICAL EXAMPLES 55
IV.2 LINEARIZED EULER EQUATIONS IN PRIMITIVE VARIABLES . 62
IV.2.1 DERIVATION OF PML EQUATIONS 62
IV.2.2 NUMERICAL EXAMPLES 66
IV.3 EXTENSION OF CYLINDRICAL PML TO OBLIQUE MEAN FLOW 69
IV.3.1 GENERAL APPROACH 69
IV.3.2 PML FOR NONLINEAR EULER EQUATIONS IN CONSERVATION FORM 71
IV.3.3 PML FOR LINEARIZED EULER EQUATIONS IN PRIMITIVE VARIABLES 74
V CONCLUDING REMARKS 77

BIBLIOGRAPHY 80

VITA 85

LIST OF FIGURES

Figure Page

1. Diagrams of PML configurations for rectangular and circular domains. 7
2. Dispersion relations for mean flow in the x-direction only. 9
3. Dispersion relations after the space-time transformation. 11
4. Dispersion relations for mean flow in both the x- and y-directions. . . 12
5. Proposed x-, y-, and corner layers. 16
6. Contours of maximum imaginary parts, ω_i, of eigenvalues for $\sigma_x = \sigma_y = 2$ over varying Mach numbers. 21
7. Contours of maximum imaginary parts, ω_i, of eigenvalues for $U_0 = V_0 = 0.5$ over varying absorption coefficients. 22
8. Contours of density at times $t = 0$, 70, 100 and 200, showing three initial entropy waves and an initial acoustic wave located at the center, each of which exits the domain with little reflection. 24
9. Top: PML and reference solutions of density at the point $(45, 45)$ as a function of time. 25
10. Reflection coefficients versus time for density ρ along $x = \pm 45$ and $y = \pm 45$ for PML widths $D = 10\Delta x$ and $D = 20\Delta x$ and absorption coefficient parameters $\alpha = 2$ and $\alpha = 3$. 26
11. Schematic of $\mathbf{u}$ components. 28
12. Contours of maximum imaginary parts, ω_i, of eigenvalues for $\sigma_x = \sigma_y = 2$ over varying velocities. 32
13. Contours of maximum imaginary parts, ω_i, of eigenvalues for $U_0 = V_0 = 0.5$ over varying absorption coefficients. 33
14. Isentropic vortex: Contours of v-velocity at times $t = 0, 1.5, 2.0$, and 2.5. 35
15. Top: Solutions of v-velocity at the point (0.9, 0.9) as a function of time. 36
16. Reflection coefficient for v-velocity versus time along $x = \pm 0.9$, $y = \pm 0.9$ for $U_0 = V_0 = 0.5$ and $U'_{\max} = 0.25$. 37
17. Maximum difference between PML and reference solutions of v-velocity versus time along $x = \pm 0.9$, $y = \pm 0.9$ for $U_0 = V_0 = 0.2$ and varying $U'_{\max}$. 38
18. Schematic of overset grids used. 39
19. Flow over a circular cylinder: Contours of density during the formation of the transient pressure pulse. 40
20. Transient pressure pulse: Contours of density at time $t = 6$. 41
21. Vortex shedding: Contours of density at time $t = 30$. 42
22. Vortex shedding: Contours of density at time $t = 35$. 43
23. Vortex shedding: Contours of density at time $t = 150$. 44
24. Top: Time history of v-velocity at the point $(5.8, 5.8)$ for PML of width $D = 40\Delta x$ against a reference solution. 45

25. Maximum differences between PML and reference solutions for v-velocity versus time along $x = 5.8$, $y \in [2, 5.8]$ and $x \in [2, 5.8]$, $y = 5.8$ for PML widths $D = 20\Delta x$, $40\Delta x$, and $60\Delta x$. 46
26. Overset grids include three concentric cylindrical grids. 56
27. Pressure pulse with no mean flow: Pressure contours at times $t = 0, 2, 5$, and 7.5. 57
28. Top: Time history of pressure at a single point for the PML and reference solutions. 58
29. Overset grids include three concentric cylindrical grids with a Cartesian grid in the center. 59
30. Pressure pulse with mean flow: Pressure contours at times $t = 0, 2, 5$, and 8. 60
31. Top: Time history of pressure at a single point for the PML and reference solutions. 61
32. Acoustic, vorticity, and entropy pulses with horizontal mean flow: Density contours at times $t = 0, 4, 6$, and 10. 67
33. Top: Time history of density at the point $(r, \theta) = (4.55, 0)$ for the PML and reference solutions. 68
34. Reflection coefficient for density as a function of time, computed along the points $r = 4.55$, $\theta \in [0, 2\pi)$. 69
35. Mean flow in two dimensions. 70
36. Rotated coordinate system. 71

CHAPTER I

INTRODUCTION

The rise of computers in the mid-twentieth century revolutionized the way the world was run, and the field of mathematics was no exception to the changes. With the increased capabilities of computers, it soon became possible for mathematicians to solve problems that previously remained unsolvable, and a new branch of mathematics was born. In computational mathematics, the focus shifted toward developing new ways for the computer to accommodate mathematical problems. Because mathematics is relevant in practically every scientific discipline, most disciplines have a branch of study devoted exclusively to solving problems computationally. Among these are Computational Chemistry, Computational Biology, Computational Electromagnetics, Computational Fluid Dynamics, and Computational Aeroacoustics. Many fields in which a system can be studied mathematically can also be studied computationally. Often, the approach is to find the governing equations of the physical system, then find numerical solutions to the given equations using computational methods. For example, in Computational Electromagnetics (CEM), which uses numerical methods to solve problems dealing with electromagnetic fields and electromagnetic wave propagation, the solutions to Maxwell's equations are sought numerically. Computational Fluid Dynamics (CFD) uses numerical methods to solve problems involving fluid flows, and in general, solutions to the Navier-Stokes or Euler equations are found. Closely related to CFD is Computational Aeroacoustics (CAA), which focuses not only on the flow fields, but also on the related acoustic fields generated by and interacting with such flows. Again, solutions to the Navier-Stokes or Euler equations are found numerically.

In each of these disciplines, a proper treatment at the boundaries becomes quite relevant to maintaining the accuracy of solutions. First, a treatment at physical boundaries must be designed to mimic actual physical properties on that boundary, as is done, for example, with the no-slip condition [1]. Secondly, a treatment of numerical (nonphysical) boundaries is equally important to maintaining accurate solutions that simulate the actual behavior of the system in the physical world. For example, when an open or infinite physical domain is truncated for numerical

This dissertation follows the style of the *AIAA Journal*.

simulation, the solutions should accurately represent the physical behavior as if no outside surrounding boundaries are present. Without any condition on the boundary, waves would be reflected back into the domain. Therefore, boundary conditions are imposed at the numerical boundary that eliminate any spurious reflections off these numerical boundaries. Such conditions are therefore referred to as nonreflecting boundary conditions.

The importance of boundary conditions in how they affect interior solutions, in particular for nonphysical boundaries, has led to a concentrated study on the boundary conditions themselves. Many types of nonreflecting boundary conditions have been developed, including characteristic boundary conditions [2–7], asymptotic boundary conditions [8–13], absorbing zone boundary conditions [14–23], and more recently, the Perfectly Matched Layer [24–44], which will be the focus of this work.

Characteristic boundary conditions are based on the characteristics of the governing equations [45]. At each boundary, conditions are then given to accommodate either incoming or outgoing waves by separating positive and negative eigenvalues in the eigenvalue diagonal matrix of the characteristic decomposition of the Jacobian matrices of the governing equations. This type of boundary condition is the most commonly used nonreflecting boundary condition for Euler's equations [30]. Early efforts in the application of characteristic boundary conditions can be found in the works of Thompson [2] and Giles [3] in the late 1980's and early 1990's. A significant advancement came from Pionsot and Lele in 1992 [4], in which the work in [2] was generalized for use with the Navier-Stokes equations. Further examples are found in [5–7]. Characteristic boundary conditions work particularly well when waves exit the domain perpendicular to the boundary. Because the conditions are not exact, however, the method can introduce reflection errors [45]. Specifically, the reflection errors for the outgoing acoustic and vorticity waves, respectively, were found in [46] to be

$$R_{\text{acoustic}} = \frac{1 - \cos(\text{Angle of Incidence})}{1 - \cos(\text{Angle of Reflection})} \tag{1}$$

$$R_{\text{vorticity}} = \frac{\sin(\text{Angle of Incidence})}{1 - \cos(\text{Angle of Reflection})} \tag{2}$$

When the angle of incidence is zero, the reflection error is also zero for both acoustic and vorticity waves, and the method is quite accurate. However, an increase in the angle of incidence will cause an increase in the reflection errors, which ultimately

results in a less accurate solution. Therefore, this type of boundary condition is most effective when the mean flow occurs at an angle close to zero or at least small enough to maintain a desired level of accuracy. This restriction on possible mean flow directions is the major limitation of the characteristic boundary condition.

Asymptotic boundary conditions, as given, for example, in [8–13], are formed based on the asymptotic solutions of the governing equations. Numerical boundaries are assumed to be far enough from the source that asymptotic solutions are valid in the region near the boundary. Clearly, one downfall to this method is that the computational domain must be kept large enough to maintain the validity of such an assumption. Often times, this requires the use of a domain that is larger than necessary, resulting in decreased efficiency.

With the absorbing zone technique [14–23], the domain is extended to include an additional surrounding zone, which is designed to decrease the amplitudes of the outgoing waves. In this way, boundary reflections will be minimized. Absorbing zones are alternately referred to as "sponge layers," "exit zones," or "buffer zones" [45]. Various methods of implementation exist for reducing the amplitudes of the outgoing waves. Among them are grid stretching [14–15], numerical filtering [15–17], and artificial dissipation and damping [18–20]. In [21], Bodony has recently given a generalization of Israeli and Orszag's work on dissipation and damping from [18]. Varying the convective mean velocity in the buffer zone has also been used as a means to minimize reflections [22–23]. These methods can also be used in conjunction with one another for improved performance. With absorbing zones, however, solutions must be modified very gradually as the waves exit through the absorbing region. Quick changes to the solutions could result in reflections occurring within the zone itself [45].

The Perfectly Matched Layer (PML) could easily be considered an extension of the absorbing zone technique. With PML, the numerical boundary is surrounded by a nonphysical medium that is designed to absorb the outgoing waves exponentially in time before they have a chance to reflect. Different from the absorbing zone techniques, however, the PML equations reduce to the governing equations on the interface between the interior and PML domains and are transparent to linear waves. They are therefore considered exact in a theoretical sense. Hence, they are appropriately termed "perfectly matched." Because of this, the width of the Perfectly Matched Layer is generally much smaller in comparison to absorbing zones

because a longer absorbing zone is often needed to fully damp the outgoing waves without causing internal reflections [45]. Due to the perfect matching, PML is the first method that can be considered reflectionless in theory. Clearly, errors still arise due to discretizations in time and space. However, because of this improved accuracy at the boundary, smaller overall error is generally observed. Waves are also absorbed independent of frequency and angle of incidence, an advantage over characteristic boundary conditions [29]. A more detailed explanation of the PML method is given in Section II.1.

The goal of this paper is to extend upon the previous capabilities of the Perfectly Matched Layer as an absorbing boundary condition, with specific application to Aeroacoustics problems. Up to this time, the majority of work done involving PML in the field of Aeroacoustics has focused on situations where the mean flow is perpendicular to a boundary, as has been done, for example, in [25–33]. While such work is necessary and useful, it is also important to accommodate the more general case where background flow strikes the boundary at an arbitrary angle. Such a capability is useful, for example, for an airfoil at a nonzero angle of attack. Chapter III presents the PML boundary conditions designed for the case of an oblique background flow. Although several other approaches have arisen in the literature to handle the case involving oblique mean flow, none has been altogether satisfactory. A brief survey of such proposed methods is included in Section II.2.2 to highlight the differences with the approach given in the present work. Of specific importance in the present extension of the PML method is the technique of deriving horizontal and vertical side layers independently. This allows the stability requirements for both horizontal and vertical layers to be met simultaneously. Also of importance is the formation of dynamically stable corner layers, which are necessary for the success of the PML condition when an oblique mean flow is present. Another contribution to current PML formulations in acoustics is the derivation of a PML boundary condition in a cylindrical coordinate system. Most CAA and CFD references on PML include only the construction of PML equations for use in a Cartesian coordinate system. In some physical situations, however, the use of an alternative coordinate system can provide major simplifications to the study of the problem at hand. The cylindrical coordinate system is a commonly used alternative to Cartesian coordinates. Such a system is useful, for example, when dealing with radially symmetric problems. For this reason, the derivation of PML equations in cylindrical coordinates for use with

both primitive and conservation variables is given in Chapter IV. Similar to the PML in Cartesian coordinates, the difficulty in the formation of the cylindrical PML equations lies in maintaining stable solutions for all types of waves. The method presented in this work ensures that the stability requirement on the boundary condition is met. Further, the cylindrical PML will be designed to handle the more general case of mean flow in an arbitrary direction. This generalization is carried out by using a rotation of the original coordinate system.

CHAPTER II

THE PERFECTLY MATCHED LAYER (PML) METHOD

II.1 INTRODUCTION TO PERFECTLY MATCHED LAYERS

As mentioned above, when dealing with physical problems that have open domains, the need is great for highly accurate nonreflecting boundary conditions, particularly in the field of acoustics. Since reflection errors introduced by the truncation of open domains can compromise the accuracy of solutions in the interior, it is vital that reflections at the boundary be eliminated or at least reduced to within an acceptable level of error. Further, as the accuracy of spatial and temporal discretizations continues to improve, it is important that the accuracy of conditions on the boundaries increase accordingly. That in mind, the Perfectly Matched Layer (PML) has been shown effective in eliminating boundary reflections at high levels of accuracy. Therefore, such a method will be the focus of this work as it relates to problems in the field of Aeroacoustics.

The Perfectly Matched Layer was initially proposed by Berenger as an absorbing boundary condition for electromagnetic waves supported by the Maxwell equations [24]. Hu extended the method to the field of acoustics by constructing a PML boundary condition for use with the Euler equations [29–30]. The concept behind the Perfectly Matched Layer method is relatively simple. As is shown in Figure 1, truncated domains are extended on the boundaries to include an artificial, nonphysical domain or "layer" that absorbs incoming waves before they reach the numerical boundary. In essence, waves are damped before they have a chance to be reflected. This is done by introducing new equations in the so-called "perfectly matched layer" or PML region. Such equations will be designed to decrease the amplitude of incoming waves exponentially in time, while matching interior governing equations on the interface between interior and PML domains. Because of the perfect matching on the interface, PML boundary conditions are considered theoretically reflectionless for linear waves [24, 29–30].

The derivation of the PML equations involves little more than a complex change of variable applied on the spatial variable in the frequency domain [36, 38–39, 41]. For example, to design an absorbing layer for truncation in the x-direction, the PML change of variable will take the form

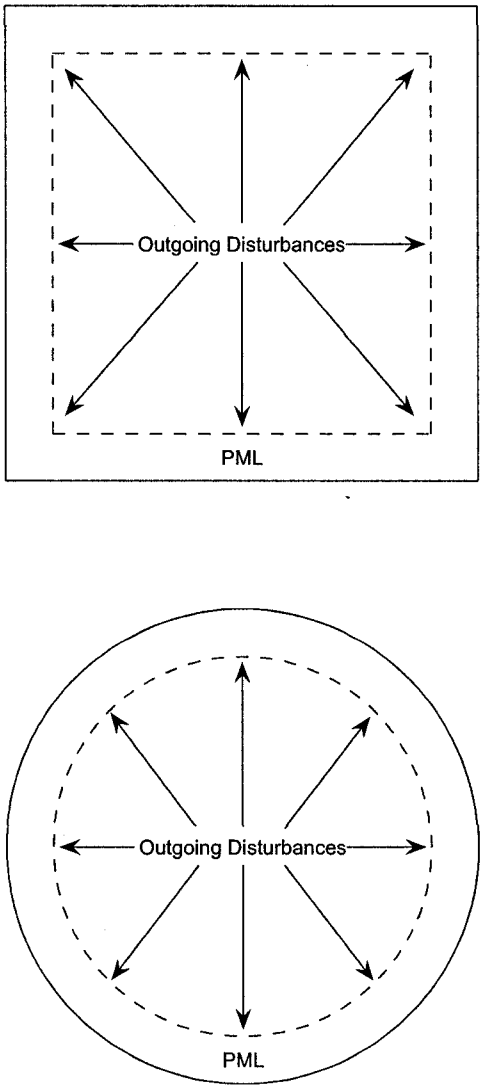

FIG. 1: Diagrams of PML configurations for rectangular and circular domains. Dashed lines indicate the location of the interface between the interior and PML domains.

$$x \rightarrow x + \frac{i}{\omega}\int_{x_0}^{x} \sigma_x \, dx \tag{3}$$

where σ_x, the absorption coefficient, is a positive function of x only in the PML region and zero in the interior region. Such a transformation is applied in the frequency domain, and the resulting equations emerge upon returning to the time domain. As we will see in the next section, however, care must be taken before applying the PML change of variable in order to ensure the numerical stability of the equations. The system will be numerically stable provided there is consistency in phase and group velocities at the time the change of variable is applied [30]. A more thorough examination of this issue is discussed in the following section.

II.2 THE IMPORTANCE OF DISPERSION RELATIONS

II.2.1 ONE-DIMENSIONAL MEAN FLOW

As mentioned previously, to ensure numerical stability, certain conditions must be met before the PML change of variable can be applied. Specifically, there must be consistency in the phase and group velocities. To understand this more clearly, consider the two-dimensional linearized Euler equations in Cartesian coordinates for the case of mean flow in the x-direction:

$$\frac{\partial \mathbf{u}}{\partial t} + \mathsf{A}\frac{\partial \mathbf{u}}{\partial x} + \mathsf{B}\frac{\partial \mathbf{u}}{\partial y} = 0, \tag{4}$$

where

$$\mathbf{u} = \begin{pmatrix} \rho \\ u \\ v \\ p \end{pmatrix}, \; \mathsf{A} = \begin{pmatrix} U_0 & 1 & 0 & 0 \\ 0 & U_0 & 0 & 1 \\ 0 & 0 & U_0 & 0 \\ 0 & 1 & 0 & U_0 \end{pmatrix}, \; \mathsf{B} = \begin{pmatrix} 0 & 0 & 1 & 0 \\ 0 & 0 & 0 & 0 \\ 0 & 0 & 0 & 1 \\ 0 & 0 & 1 & 0 \end{pmatrix} \tag{5}$$

and ρ is density, u and v are velocity components, p is the pressure, and U_0 is the mean flow Mach number in the x-direction. The dispersion relations of linear waves are found to be

$$(\omega - U_0 k_x)^2 - {k_x}^2 - {k_y}^2 = 0 \tag{6}$$

for acoustic waves and

$$\omega - U_0 k_x = 0 \tag{7}$$

for vorticity and entropy waves. Holding k_y constant, we can plot both of these curves for frequency ω as a function of wavenumber k_x, as shown in Figure 2. Since phase

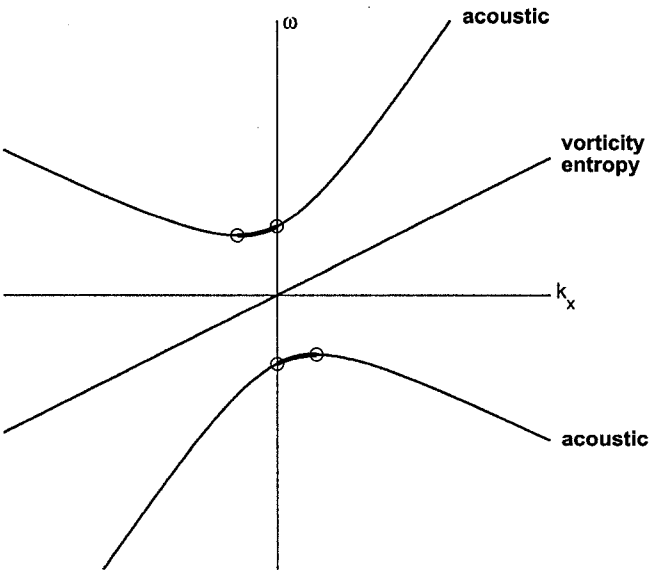

FIG. 2: Dispersion relations for mean flow in the x-direction only. Bold lines indicate inconsistent phase and group velocities.

velocity is the ratio of frequency to wavenumber ($v_p = \frac{\omega}{k_x}$), quadrant numbers will determine the sign of phase velocity, with quadrants I and III representing positive phase velocity, and quadrants II and IV representing negative phase velocity. Alternatively, since group velocity is the change in frequency with respect to the change in wavenumber ($v_g = \frac{d\omega}{dk_x}$), the sign of group velocity will be determined by the sign of the slope at a given point on the curve. The problem arises in quadrants II and IV, where portions of the curves for the acoustic waves have positive slope, i.e., positive group velocity, but reside in quadrants where phase velocity is negative. If this inconsistency remains uncorrected when the PML change of variable is applied, the resulting PML equations will produce exponentially growing solutions, rather than exponentially decaying ones. To see this more clearly, assume the wave solution is of the form

$$\mathbf{u}(x,t) = \mathbf{A}e^{i(k_x x - \omega t)} \tag{8}$$

where $\mathbf{A}$ is constant. Upon making the PML substitution

$$x \rightarrow x + \frac{i}{\omega}\int_{x_0}^{x} \sigma_x \, dx \tag{9}$$

the resulting solution is

$$\mathbf{u}(x,t) = \mathbf{A}e^{-\frac{k_x}{\omega}\int_{x_0}^{x} \sigma_x \, dx} e^{i(k_x x - \omega t)} \tag{10}$$

In the first exponential term, $e^{-\frac{k_x}{\omega}\int_{x_0}^{x} \sigma_x \, dx}$, the sign of $\frac{k_x}{\omega}$ will be determined by the sign of phase velocity, since the two are reciprocals of one another. Similarly, the sign of the integral $\int_{x_0}^{x} \sigma_x \, dx$ will be determined by the sign of the group velocity in the following way: a positive group velocity indicates a right-traveling wave and thus an increase of x in the positive direction. Since σ_x is a positive function, this will also correspond to a positive integral. Conversely, a negative group velocity will result in a decrease in x and ultimately in a negative integral. Therefore, as long as the signs of phase and group velocity are the same, the exponential term will be raised to a negative power and thus will be exponentially decreasing with the increase or decrease in x. However, if the signs of phase and group velocity are opposite, the exponent will be positive, and the term will grow exponentially with the change in x, causing the solution to grow exponentially as well. In such a case, however, a single space-time transformation, namely,

$$t \rightarrow t + \beta_x x \tag{11}$$

is effective in eliminating the inconsistency, where

$$\beta_x = \frac{U_0}{1 - U_0^2} \tag{12}$$

The factor β_x is related to the locations of zero group velocity. After applying this transformation, the updated dispersion relations are given by

$$\left(\frac{1}{1 - U_0^2}\right)\omega^2 - (1 - U_0^2)k_x^2 - k_y^2 = 0 \tag{13}$$

for acoustic waves and

$$\left(\frac{1}{1-U_0^2}\right)\omega - U_0 k_x = 0 \tag{14}$$

for vorticity and entropy waves, and the signs of phase and group velocities become aligned, as shown in Figure 3. The PML change of variable can then be readily applied in the frequency domain without risk of instability.

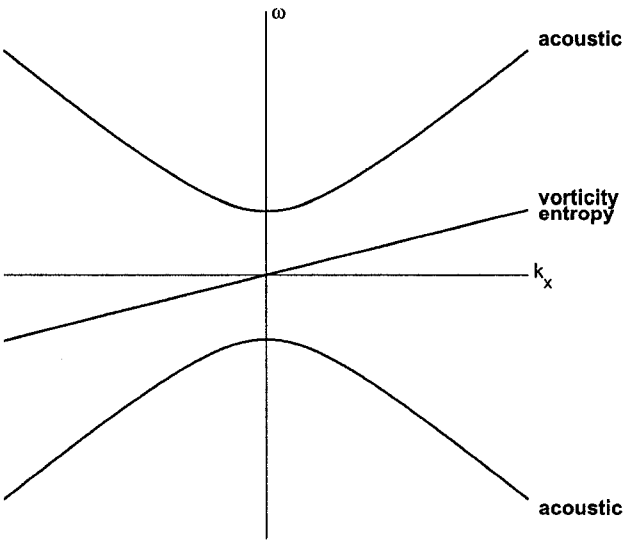

FIG. 3: Dispersion relations after the space-time transformation.

II.2.2 TWO-DIMENSIONAL MEAN FLOW

In the case for mean flow in two dimensions, or oblique mean flow, correcting the inconsistencies in phase and group velocity is not as simple as applying a single space-time transformation, as was the case for flow in only one direction. To see this more clearly, consider again the linearized Euler equations, this time with nonzero mean flow in both the x- and y-directions. The equations remain the same as those given in (4)–(5), with only a modification to the B matrix, now given by

$$\mathsf{B} = \begin{pmatrix} V_0 & 0 & 1 & 0 \\ 0 & V_0 & 0 & 0 \\ 0 & 0 & V_0 & 1 \\ 0 & 0 & 1 & V_0 \end{pmatrix} \tag{15}$$

where V_0 is the mean flow Mach number in the y-direction. This gives rise to a change in the dispersion relations, as terms involving V_0 will now appear. In this case, the dispersion relations are given by

$$(\omega - U_0 k_x - V_0 k_y)^2 - {k_x}^2 - {k_y}^2 = 0 \tag{16}$$

for acoustic waves and

$$\omega - U_0 k_x - V_0 k_y = 0 \tag{17}$$

for vorticity and entropy waves. Again, holding k_y constant, we can plot frequency ω versus wavenumber k_x, as shown in Figure 4. As is seen in the figure, the nonzero V_0

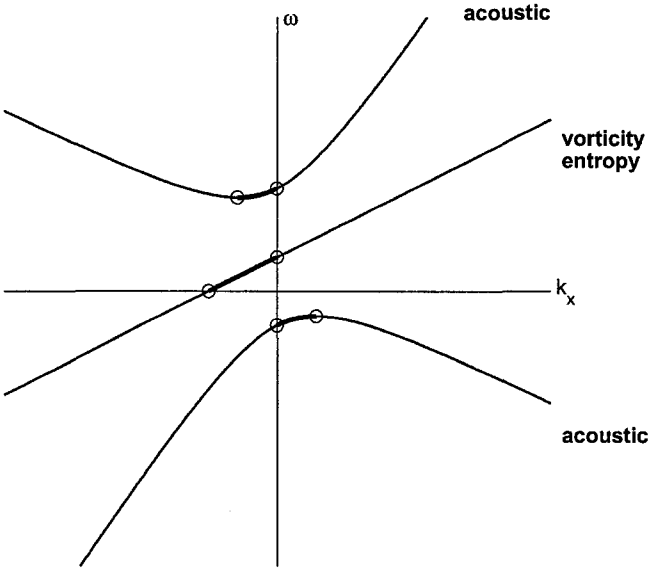

FIG. 4: Dispersion relations for mean flow in both the x- and y-directions. Bold lines indicate inconsistent phase and group velocities.

has caused a vertical shift in the curves. Again, there is inconsistency in the phase and group velocities for the acoustic waves, but now, in addition, an inconsistency is present for vorticity and entropy waves, indicated by the portion of the straight line that now passes through the second quadrant. In this case, no transformation has been found to remove both sets of inconsistencies.

Attempts have been made to handle the case of two-dimensional mean flow, but none has been found completely satisfactory. For example, in [42], Appelo, Hagstrom,

and Kreiss present the PML equations for waves entering the PML domain at an oblique angle. However, the authors fail to provide a treatment for the corner layers. Diaz and Joly also address the issue of oblique mean flow but make efforts only in the analysis of acoustic waves [43]. Nataf, in [44], uses Smith-factorizations to form the PML equations for any direction of mean flow, but this approach has yet to be shown extendable to the nonlinear equations. As will be seen with the equations and examples below, the approach given in the present work is complete in its handling of acoustic, vorticity, and entropy waves for linear and nonlinear equations through a proper treatment of both side and corner layers.

Specifically, the PML equations in Cartesian coordinates will be derived as follows: horizontal and vertical side layers will be formed independently of one another. Then for each type of side layer, a moving-frame change of variables can be used to effectively eliminate the mean flow in the transverse direction, which essentially reduces the mean flow down to one dimension. Because this change of reference does not affect the location of the Euler-PML interface, the PML equations for one-dimensional mean flow are then valid as the side layer equations in the given frame of reference. The final equations emerge upon return to the original frame of reference. Because the moving-frame changes of variables used for the horizontal and vertical layers cannot be applied simultaneously, the corner layer equations will be constructed as a linear combination of the horizontal and vertical side layers. Because such a construction does not result in equations that are perfectly matched to the governing equations, the stability of the corner layer equations must be artificially enforced. In our case, this is done by appending additional terms to the unmatched corner layer equations. The PML region then consists of perfectly matched side layers and dynamically stable corner layers.

The PML for cylindrical coordinates will also be given in the present study. Although scarcely provided in the PML literature, they are important in many practical computations. The difficulty in formulating the stable PML for cylindrical coordinates in the presence of an oblique mean flow also stems from inconsistencies in phase and group velocities. However, just as was possible in the Cartesian formulation, there is a way to work around the stability problems. This time a different approach is taken: the PML are first derived for horizontal mean flow only. In this situation, stability is easily achieved with the use of a proper space-time transformation, as was outlined in Section II.2.1. Next, to extend the capability of the PML to

include an oblique mean flow, a rotation of coordinates is employed to align the horizontal axis with the direction of mean flow. Because of the radial symmetry of the coordinate system, a rotation does not affect the location of the Euler-PML interface. Therefore, in the new rotated coordinate system, the PML are derived identically as in the case of horizontal mean flow, since under such a rotation, the mean flow occurs in only one dimension of the new coordinate system. Finally, upon returning to the original coordinate system, the cylindrical PML for an oblique mean flow emerge. In this case, there is no need to form separate equations for any particular region of the PML domain, as was done for the corner layers above. Therefore, with no artificially constructed equations, the entire layer will be perfectly matched across the interface.

CHAPTER III

PML IN CARTESIAN COORDINATES FOR OBLIQUE MEAN FLOW

III.1 LINEARIZED EULER EQUATIONS

III.1.1 PROPOSED PML EQUATIONS

Our first effort will be in deriving PML equations for the linearized Euler equations in Cartesian coordinates, given by

$$\frac{\partial \mathbf{u}}{\partial t} + \mathsf{A}\frac{\partial \mathbf{u}}{\partial x} + \mathsf{B}\frac{\partial \mathbf{u}}{\partial y} = 0, \tag{18}$$

where

$$\mathbf{u} = \begin{pmatrix} \rho \\ u \\ v \\ p \end{pmatrix}, \ \mathsf{A} = \begin{pmatrix} U_0 & 1 & 0 & 0 \\ 0 & U_0 & 0 & 1 \\ 0 & 0 & U_0 & 0 \\ 0 & 1 & 0 & U_0 \end{pmatrix}, \ \mathsf{B} = \begin{pmatrix} V_0 & 0 & 1 & 0 \\ 0 & V_0 & 0 & 0 \\ 0 & 0 & V_0 & 1 \\ 0 & 0 & 1 & V_0 \end{pmatrix} \tag{19}$$

and ρ is density, u and v are velocity components, p is the pressure, and U_0 and V_0 are Mach numbers in the x- and y-directions, respectively. Because flow is two-dimensional, x- and y-layers will be formed independently, and stable corner layers will subsequently be constructed. In this way, for the x- and y-layers, a moving-frame change of variables can be used to simulate no flow in the transverse direction, making it again possible to remove the inconsistencies with a single space-time transformation. Once phase and group velocities are consistent, we can proceed with the PML method, applying the PML changes of variable

$$x \to x + \frac{i}{\omega}\int_{x_0}^{x} \sigma_x \, dx, \ y \to y + \frac{i}{\omega}\int_{y_0}^{y} \sigma_y \, dy \tag{20}$$

to form the x- and y-layer PML equations, respectively, where σ_x and σ_y are positive functions of x and y, respectively. Consequently, in the x-layer, $\sigma_y = 0$, and in the y-layer, $\sigma_x = 0$. This leaves only a needed treatment for the corner layer, where both σ_x and σ_y are nonzero. As we will see in this section and Section III.2, a combination of the equations for the x- and y-layers will be sufficient. Figure 5 shows a schematic of the proposed x-, y-, and corner layers.

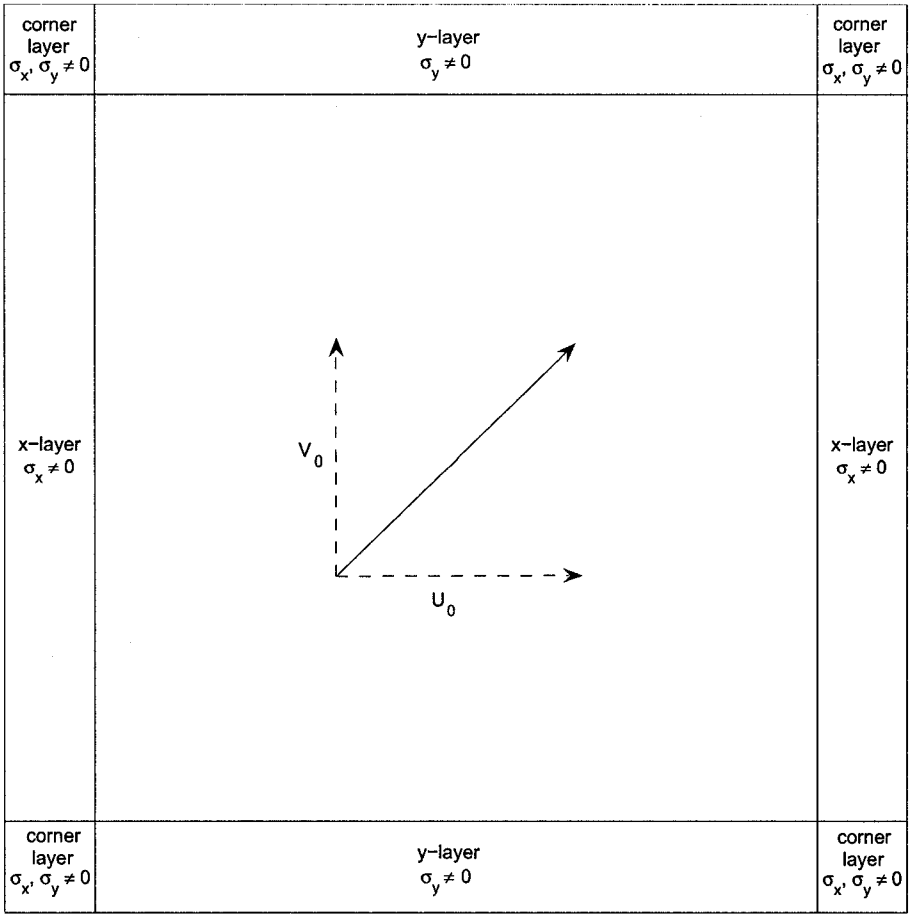

FIG. 5: Proposed x-, y-, and corner layers.

We begin by deriving the equations for the vertical x-layers. First, a moving-frame change of variables will be employed to simulate no vertical flow, namely,

$$\hat{x} = x \tag{21}$$

$$\hat{y} = y - V_0 t \tag{22}$$

$$\hat{t} = t \tag{23}$$

which gives

$$\frac{\partial}{\partial x} = \frac{\partial}{\partial \hat{x}} \tag{24}$$

$$\frac{\partial}{\partial y} = \frac{\partial}{\partial \hat{y}} \tag{25}$$

$$\frac{\partial}{\partial t} = \frac{\partial}{\partial \hat{t}} - V_0 \frac{\partial}{\partial \hat{y}} \tag{26}$$

The equation (18) now becomes

$$\frac{\partial \mathbf{u}}{\partial \hat{t}} - V_0 \frac{\partial \mathbf{u}}{\partial \hat{y}} + \mathsf{A} \frac{\partial \mathbf{u}}{\partial \hat{x}} + \mathsf{B} \frac{\partial \mathbf{u}}{\partial \hat{y}} = 0 \tag{27}$$

or

$$\frac{\partial \mathbf{u}}{\partial \hat{t}} + \mathsf{A} \frac{\partial \mathbf{u}}{\partial \hat{x}} + \mathsf{B}_0 \frac{\partial \mathbf{u}}{\partial \hat{y}} = 0 \tag{28}$$

where

$$\mathsf{B}_0 = \mathsf{B} - V_0 \mathsf{I} \tag{29}$$

and I is the four-dimensional identity matrix. The equation is now equivalent to those given in (4)–(5). Therefore, the stable PML equations for (28) will be identical to those for (4)–(5), which are given in [30] as

$$\frac{\partial \mathbf{u}}{\partial \hat{t}} + \mathsf{A} \frac{\partial \mathbf{u}}{\partial \hat{x}} + \mathsf{B}_0 \frac{\partial \mathbf{u}}{\partial \hat{y}} + \sigma_x \mathsf{B}_0 \frac{\partial \mathbf{q}_1}{\partial \hat{y}} + \sigma_x \mathbf{u} + \sigma_x \beta_x \mathsf{A} \mathbf{u} = 0 \tag{30}$$

$$\frac{\partial \mathbf{q}_1}{\partial \hat{t}} = \mathbf{u} \tag{31}$$

where again β_x is given by

$$\beta_x = \frac{U_0}{1 - U_0^2} \tag{32}$$

and terms involving σ_y are omitted since $\sigma_y = 0$ in the x-layer. The variable $\mathbf{q}_1$ is an auxiliary variable representing the antiderivative of $\mathbf{u}$. Since the location of the vertical Euler-PML interface remains unchanged after the moving-frame transformation is applied, equations (30)–(31) give valid x-layer equations. After transforming back to the original coordinates, x, y, and t, the resulting stable PML x-layer equations emerge:

$$\frac{\partial \mathbf{u}}{\partial t} + \mathsf{A}\frac{\partial \mathbf{u}}{\partial x} + \mathsf{B}\frac{\partial \mathbf{u}}{\partial y} + \sigma_x \mathsf{B}_0 \frac{\partial \mathbf{q}_1}{\partial y} + \sigma_x \mathbf{u} + \sigma_x \beta_x \mathsf{A}\mathbf{u} = 0 \tag{33}$$

$$\frac{\partial \mathbf{q}_1}{\partial t} + V_0 \frac{\partial \mathbf{q}_1}{\partial y} = \mathbf{u} \tag{34}$$

A similar approach is used for the y-layer equations. Specifically, the moving-frame change of variables

$$\hat{x} = x - U_0 t \tag{35}$$

$$\hat{y} = y \tag{36}$$

$$\hat{t} = t \tag{37}$$

leads to

$$\frac{\partial \mathbf{u}}{\partial t} + \mathsf{A}\frac{\partial \mathbf{u}}{\partial x} + \mathsf{B}\frac{\partial \mathbf{u}}{\partial y} + \sigma_y \mathsf{A}_0 \frac{\partial \mathbf{q}_2}{\partial x} + \sigma_y \mathbf{u} + \sigma_y \beta_y \mathsf{B}\mathbf{u} = 0 \tag{38}$$

$$\frac{\partial \mathbf{q}_2}{\partial t} + U_0 \frac{\partial \mathbf{q}_2}{\partial x} = \mathbf{u} \tag{39}$$

with

$$\mathsf{A}_0 = \mathsf{A} - U_0 \mathsf{I} \tag{40}$$

and

$$\beta_y = \frac{V_0}{1 - V_0^2} \tag{41}$$

where I is the identity matrix, and $\mathbf{q}_2$ is another auxiliary variable. This leaves only the need for corner layer equations, where both σ_x and σ_y are nonzero. By combining terms from the x- and y-layer equations, we propose a set of equations for the corner layer:

$$\frac{\partial \mathbf{u}}{\partial t} + \mathsf{A}\frac{\partial \mathbf{u}}{\partial x} + \mathsf{B}\frac{\partial \mathbf{u}}{\partial y} + \sigma_y \mathsf{A}_0 \frac{\partial \mathbf{q}_2}{\partial x} + \sigma_x \mathsf{B}_0 \frac{\partial \mathbf{q}_1}{\partial y} + (\sigma_x + \sigma_y)\mathbf{u} + \sigma_x \beta_x \mathsf{A}\mathbf{u} + \sigma_y \beta_y \mathsf{B}\mathbf{u} = 0 \tag{42}$$

$$\frac{\partial \mathbf{q}_1}{\partial t} + V_0 \frac{\partial \mathbf{q}_1}{\partial y} + \sigma_y \mathbf{q}_1 = \mathbf{u} \tag{43}$$

$$\frac{\partial \mathbf{q}_2}{\partial t} + U_0 \frac{\partial \mathbf{q}_2}{\partial x} + \sigma_x \mathbf{q}_2 = \mathbf{u} \tag{44}$$

An important characteristic of these equations is that the x- or y-layer equations can be recovered automatically by setting either $\sigma_y = 0$ or $\sigma_x = 0$, respectively. It is also important to note that since the corner layer equations cannot be derived by applying the two moving frames (21)–(23) and (35)–(37) simultaneously, the interface between side and corner layers are not perfectly matched. Consequently, the terms unique to the corner equations, $\sigma_y \mathbf{q}_1$ and $\sigma_x \mathbf{q}_2$ in equations (43) and (44), respectively, have been added for stability. A further analysis of stability is discussed in the following section.

Given equations (42)–(44), specific forms for σ_x and σ_y remain to be chosen. For the purpose of our examples, the absorption coefficient for x will take on the form

$$\sigma_x = \sigma_{\max} \left| \frac{x - x_0}{D} \right|^{\alpha} \tag{45}$$

where x_0 is the location of the Euler-PML interface, D is the PML width, and $\sigma_{\max}$ and α are extra parameters, the values of which will be chosen according to the example being considered. A similar expression will be used for σ_y.

III.1.2 THE STABILITY OF CORNER LAYERS

Because corner layers were formed by combining side layers and are therefore not deemed perfectly matched, it is important to analyze the stability of the equations. To do so, we will substitute a solution of the form

$$\begin{pmatrix} \mathbf{u} \\ \mathbf{q}_1 \\ \mathbf{q}_2 \end{pmatrix} = \begin{pmatrix} \hat{\mathbf{u}} \\ \hat{\mathbf{q}}_1 \\ \hat{\mathbf{q}}_2 \end{pmatrix} e^{i(k_x x + k_y y - \omega t)} \tag{46}$$

or more compactly

$$\mathbf{U} = \hat{\mathbf{U}} e^{i(k_x x + k_y y - \omega t)} \tag{47}$$

into the corner equations (42)–(44), where $\hat{\mathbf{U}}$ is assumed constant. This yields the system

$$\frac{\partial \mathbf{U}}{\partial t} + \begin{pmatrix} \mathsf{A} & 0 & \sigma_y \mathsf{A}_0 \\ 0 & 0 & 0 \\ 0 & 0 & U_0 \mathsf{I} \end{pmatrix} \frac{\partial \mathbf{U}}{\partial x} + \begin{pmatrix} \mathsf{B} & \sigma_x \mathbf{B}_0 & 0 \\ 0 & V_0 \mathsf{I} & 0 \\ 0 & 0 & 0 \end{pmatrix} \frac{\partial \mathbf{U}}{\partial y} +$$

$$\begin{pmatrix} (\sigma_x + \sigma_y)\mathsf{I} + \sigma_x \beta_x \mathsf{A} + \sigma_y \beta_y \mathsf{B} & 0 & 0 \\ 0 & \sigma_y \mathsf{I} & 0 \\ 0 & 0 & \sigma_x \mathsf{I} \end{pmatrix} \mathbf{U} = 0 \tag{48}$$

where I is the four-dimensional identity matrix. Clearly, since

$$\frac{\partial \mathbf{U}}{\partial t} = -i\omega \mathbf{U} \tag{49}$$

$$\frac{\partial \mathbf{U}}{\partial x} = ik_x \mathbf{U} \tag{50}$$

$$\frac{\partial \mathbf{U}}{\partial y} = ik_y \mathbf{U} \tag{51}$$

the system reduces to

$$\begin{pmatrix} (k_x - i\sigma_x \beta_x)\mathsf{A} + (k_y - i\sigma_y \beta_y)\mathsf{B} - i(\sigma_x + \sigma_y)\mathsf{I} & k_y \sigma_y \mathsf{B}_0 & k_x \sigma_y \mathsf{A}_0 \\ 0 & (k_y V_0 - i\sigma_y)\mathsf{I} & 0 \\ 0 & 0 & (k_x U_0 - i\sigma_x)\mathsf{I} \end{pmatrix} \hat{\mathbf{U}}$$

$$= \omega \hat{\mathbf{U}} \tag{52}$$

or more simply,

$$\mathsf{Q}\hat{\mathbf{U}} = \omega \hat{\mathbf{U}} \tag{53}$$

where Q is the matrix in equation (52). Then assuming σ_x and σ_y are constant, it is easy to recognize (53) as an eigenvalue problem for ω, for given values of k_x and k_y. If the imaginary part, ω_i, of any eigenvalue is positive, the wave amplitude will grow exponentially in time, resulting in an unstable system. However, if every ω_i is nonpositive, the system will be dynamically stable. Figure 6 plots the contours of the maximum ω_i over subsonic Mach numbers $0 \leq U_0, V_0 \leq 0.95$ and wavenumbers $|k_x|, |k_y| \leq 20$ for absorption coefficients fixed at $\sigma_x = \sigma_y = 2$. No positive ω_i is present, which supports the proposed stability of the equations.

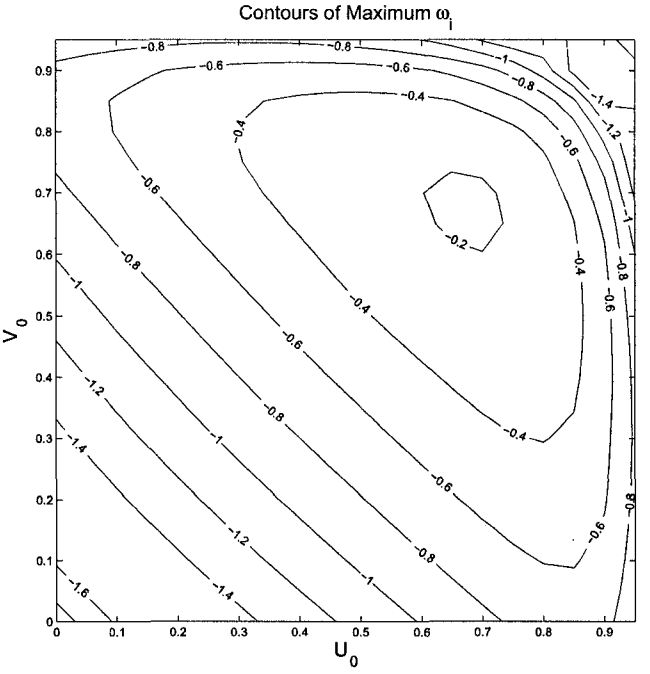

FIG. 6: Contours of maximum imaginary parts, ω_i, of eigenvalues for $\sigma_x = \sigma_y = 2$ over varying Mach numbers.

Alternatively, we can assume the values of U_0 and V_0 are constant and examine the resulting eigenvalue problem for ω over varying values of σ_x and σ_y. The result of such an analysis is plotted in Figure 7. Again, over the range of values $|\sigma_x|, |\sigma_y| \leq 5$ and $|k_x|, |k_y| \leq 20$ with $U_0 = V_0 = 0.5$, all ω_i are nonpositive, indicating that the corner equations are stable.

It is worth mentioning that the entire range of wavenumbers $|k_x|, |k_y| \leq \infty$ would normally be considered when analyzing the nondiscretized form of the equations. However, in practice, for finite difference schemes, wavenumbers larger than $\frac{\pi}{\Delta x}$ will not be present, in accordance with the Nyquist limit. Therefore, for our analysis, since $\sigma_x \Delta x \approx 2$ is a usual assumption [29], it is also reasonable to assume that examining wavenumbers with magnitudes less than 20 should safely accommodate all practical choices of Δx. It is also important to recognize that only subsonic Mach numbers need be considered, since boundary reflections cannot exist for mean flow at supersonic speeds. This is because the speed of a supersonic mean flow

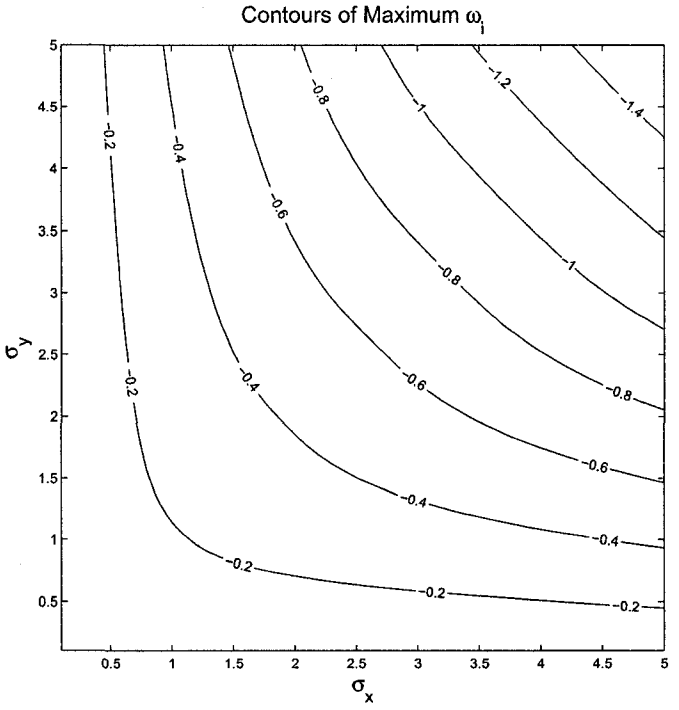

FIG. 7: Contours of maximum imaginary parts, ω_i, of eigenvalues for $U_0 = V_0 = 0.5$ over varying absorption coefficients.

would overcome the speed of waves that normally propagate in the opposite direction. Therefore, since no wave can travel against the mean flow, all waves, including potential boundary reflections, are carried out of the domain in the direction of the mean flow.

III.1.3 NUMERICAL EXAMPLES

Acoustic, Vorticity, and Entropy Waves

We will test the effectiveness of our equations (42)–(44) with a set of vorticity and entropy waves traveling with an oblique mean flow (U_0, V_0) and an acoustic wave traveling with the speed of sound relative to the mean flow. The physical domain in consideration is $[-50, 50] \times [-50, 50]$ with a PML of width D padding the boundaries. The domain is discretized by $\Delta x = \Delta y = 1$, and absorption coefficients are of

the form (45) with $\sigma_{\max} = 2$ and $\alpha = 3$. The seven-point fourth-order Dispersion-Relation-Preserving (DRP) finite difference scheme, given in [11], is used for the spatial discretization, and periodic boundary closure schemes are chosen for derivatives in x and y. This assumed periodicity at the boundary is valid in conjunction with the PML method because wave amplitudes have diminished to zero by the time waves reach the numerical boundary. For the time advancing method, the four-stage, second-order Low-Dissipation and Low-Dispersion Runge Kutta (LDDRK) scheme from [47] is chosen. The restriction $\Delta t = \frac{0.1}{1+\sqrt{2}}\Delta x$ is also enforced for stability. The wave components are initialized as follows:

$$\rho = e^{-(\ln 2)\frac{x^2+y^2}{16}} + \sum_{n=1}^{3} e^{-(\ln 2)\frac{(x-x_n)^2+(y-y_n)^2}{16}}, \quad p = e^{-(\ln 2)\frac{x^2+y^2}{16}} \tag{54}$$

$$u = \sum_{n=1}^{3}(y-y_n)e^{-(\ln 2)\frac{(x-x_n)^2+(y-y_n)^2}{16}}, \quad v = -\sum_{n=1}^{3}(x-x_n)e^{-(\ln 2)\frac{(x-x_n)^2+(y-y_n)^2}{16}} \tag{55}$$

where $(x_1, y_1) = (25, 0)$, $(x_2, y_2) = \frac{\sqrt{2}}{2}(25, 25)$, and $(x_3, y_3) = (0, 25)$ are the starting locations of the vorticity and entropy pulses, and $(0, 0)$ is the initial location of the acoustic pulse. Mach numbers are taken as $U_0 = V_0 = 0.5$, and the PML width is $D = 10\Delta x$, which, in this case, is ten percent of the width of the interior domain. It is important to recognize, however, that the PML width is independent of the size of the actual domain, which means an increase in the width of the interior domain would not require an increase in the PML width. Therefore, with an increase in the size of the total domain, the percentage of the domain allocated to the PML region would actually decrease.

Figure 8 shows the contour plots of density at times $t = 0, 70, 100$, and 200. As is shown, after part of the acoustic pulse exits the upper corner of the domain, two of the entropy pulses exit the domain through the side layers, while the third exits out the corner layer. Reflection errors generated from this third pulse are expected to be greater than those of the other two pulses, as equations are not perfectly matched at the interface between side and corner layers. However, the magnitude of the error still remains acceptably small when compared with a reference solution. The reference solution in this case is found by computing solutions on the larger domain $[-100, 100] \times [-100, 100]$.

Solutions of density at the single point $(45, 45)$ are plotted for PML and reference solutions as a function of time in the top part of Figure 9. Very little discrepancy

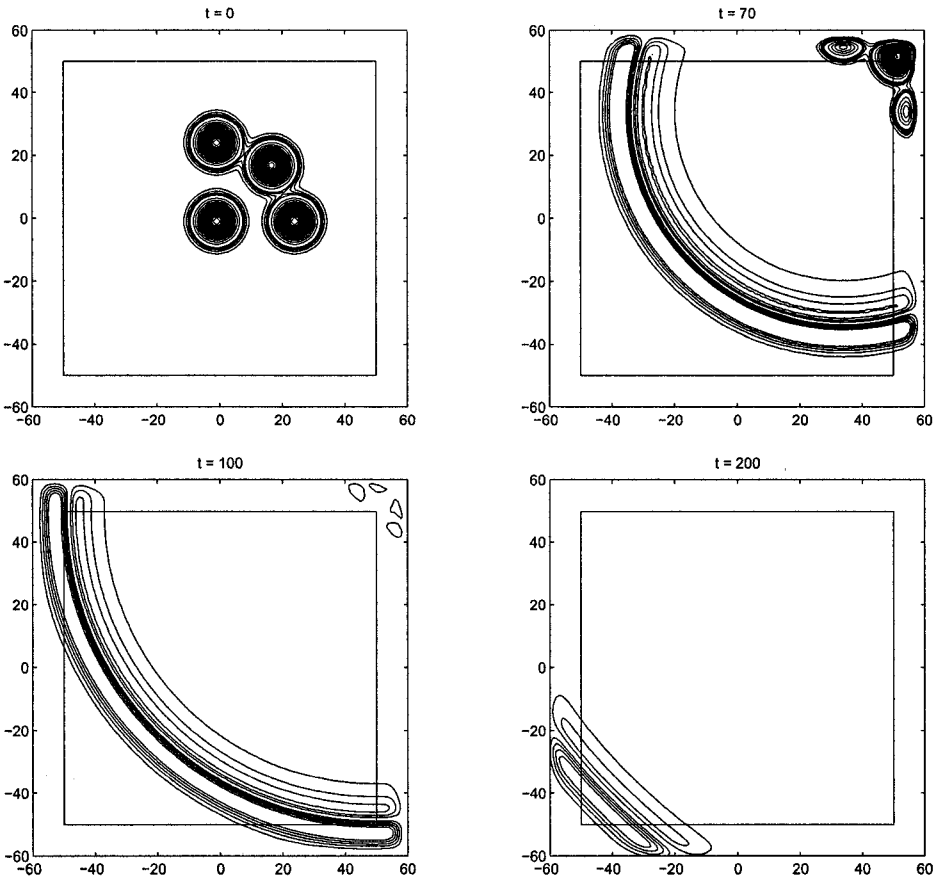

FIG. 8: Contours of density at times $t = 0$, 70, 100 and 200, showing three initial entropy waves and an initial acoustic wave located at the center, each of which exits the domain with little reflection. The mean flow Mach numbers are $U_0 = V_0 = 0.5$; PML width is $D = 10\Delta x$; and $\alpha = 3$.

is seen between the PML and reference solutions, indicating effective absorption of outgoing waves. The bottom of Figure 9 shows that the difference between the two solutions peaks at about 10^{-3}. Figure 10 plots the reflection coefficients for density between the two sets of solutions along the points $x = \pm 45$, $y = \pm 45$, for varying values of absorption coefficient parameter α and PML width D. Reflection coefficients are calculated as the maximum difference between the PML and reference solutions normalized by the maximum amplitude of the outgoing wave. In this case, the orders of magnitude for the reflection coefficients are between 10^{-3} and 10^{-2}. As the PML width increases from $D = 10\Delta x$ to $D = 20\Delta x$, a decrease in reflection

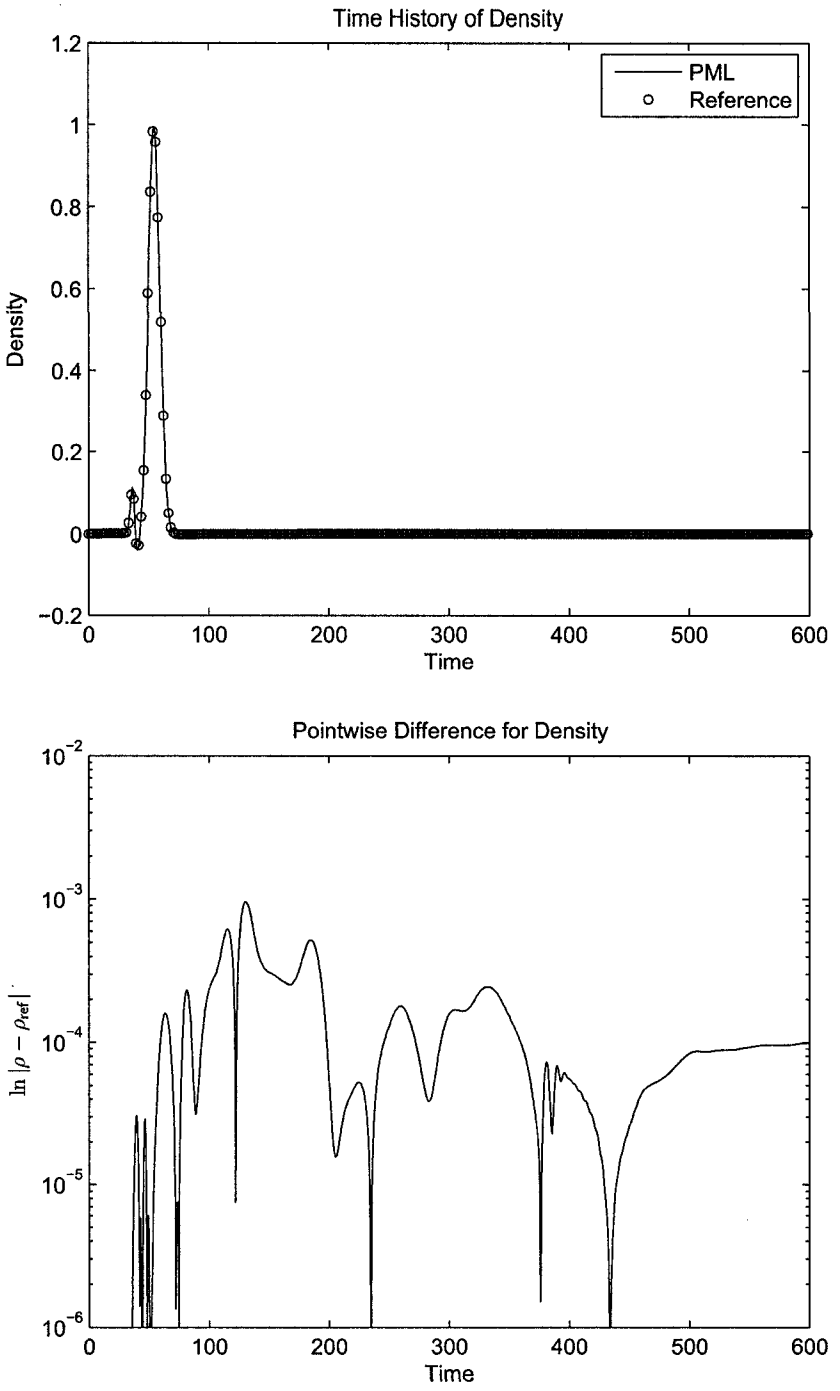

FIG. 9: Top: PML and reference solutions of density at the point $(45, 45)$ as a function of time. Bottom: Difference between the two solutions versus time at the same point.

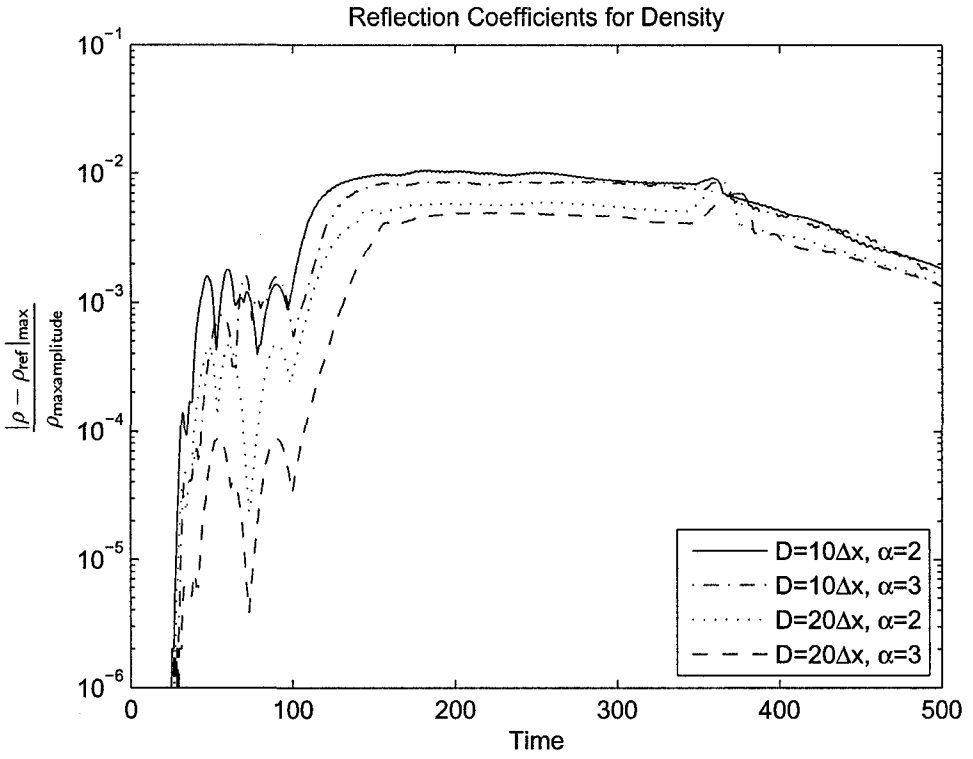

FIG. 10: Reflection coefficients versus time for density ρ along $x = \pm 45$ and $y = \pm 45$ for PML widths $D = 10\Delta x$ and $D = 20\Delta x$ and absorption coefficient parameters $\alpha = 2$ and $\alpha = 3$.

error is also noted. The effect of changing the α parameter is noticeable but not significant.

The code for this and other numerical examples has been developed in C++ specifically for this work. For this example and the first example from Section III.2.3, the code was compiled and run using Microsoft Visual C++. For the remaining examples, the code was compiled with GNU C++ and run on Linux. Plots were created using MATLAB.

III.2 NONLINEAR EULER EQUATIONS

III.2.1 DERIVATION OF PML EQUATIONS

A similar derivation will ensue for the nonlinear Euler equations. Side layers will be formed first, and stable corner layers constructed subsequently. The nonlinear Euler equations are given by

$$\frac{\partial \mathbf{u}}{\partial t} + \frac{\partial \mathbf{F}_1(\mathbf{u})}{\partial x} + \frac{\partial \mathbf{F}_2(\mathbf{u})}{\partial y} = 0 \tag{56}$$

where

$$\mathbf{u} = \begin{pmatrix} \rho \\ \rho u \\ \rho v \\ \rho e \end{pmatrix}, \ \mathbf{F}_1(\mathbf{u}) = \begin{pmatrix} \rho u \\ \rho u^2 + p \\ \rho uv \\ \rho hu \end{pmatrix}, \ \mathbf{F}_2(\mathbf{u}) = \begin{pmatrix} \rho v \\ \rho uv \\ \rho v^2 + p \\ \rho hv \end{pmatrix} \tag{57}$$

and

$$h = e + \frac{p}{\rho}, \ p = (\gamma - 1)\rho\left(e - \frac{u^2 + v^2}{2}\right) \tag{58}$$

where ρ is the density, u and v are velocity components, e is the energy, p is the pressure, and γ is the specific heat ratio. Here, the conservation form of the equations is chosen, as is often done for the nonlinear case. A constant background flow of (U_0, V_0) is assumed.

We begin the derivation of the x-layer equations somewhat differently than in the linearized case, by first splitting the solution into two parts as follows

$$\mathbf{u} = \bar{\mathbf{u}} + \mathbf{u}' \tag{59}$$

Here, $\mathbf{u}'$ is the fluctuating part of the variable, and $\bar{\mathbf{u}}$ is the pseudo mean flow, as is shown in Figure 11. The part $\bar{\mathbf{u}}$ must be time-independent and must therefore satisfy the steady Euler equations

$$\frac{\partial \mathbf{F}_1(\bar{\mathbf{u}})}{\partial x} + \frac{\partial \mathbf{F}_2(\bar{\mathbf{u}})}{\partial y} = 0 \tag{60}$$

Note, however, that $\bar{\mathbf{u}}$ does not have to be the actual mean flow, which is sometimes unknown. The part $\mathbf{u}'$ is time-dependent and will be the focus of our PML equations, since it is the part we seek to damp exponentially in time. By focusing only on the

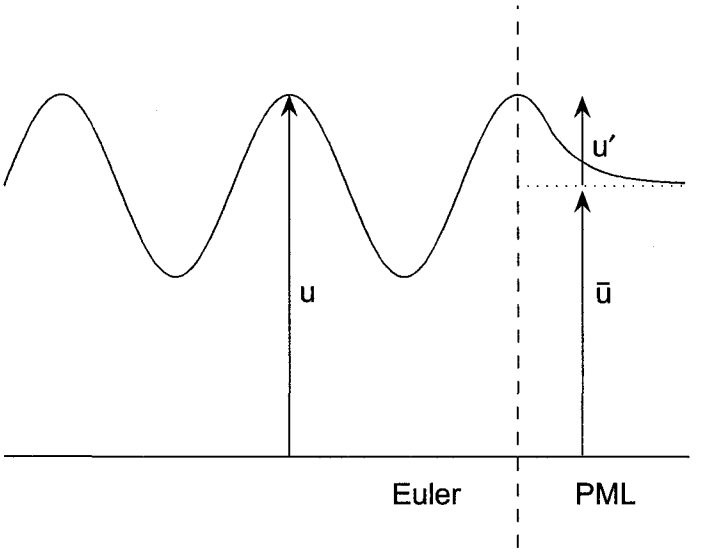

FIG. 11: Schematic of $\mathbf{u}$ components. The time-independent pseudo mean flow is denoted by $\bar{\mathbf{u}}$, and $\mathbf{u}'$ represents the time-dependent perturbation.

fluctuating part, we decrease computational effort by eliminating computation on the total variable $\mathbf{u}$, which can be significantly larger than $\mathbf{u}'$. After such a partitioning, the equations become

$$\frac{\partial \mathbf{u}'}{\partial t} + \frac{\partial(\mathbf{F}_1 - \bar{\mathbf{F}}_1)}{\partial x} + \frac{\partial(\mathbf{F}_2 - \bar{\mathbf{F}}_2)}{\partial y} = 0 \tag{61}$$

where the shorthand notations $\mathbf{F}_1 = \mathbf{F}_1(\mathbf{u})$, $\bar{\mathbf{F}}_1 = \mathbf{F}_1(\bar{\mathbf{u}})$, $\mathbf{F}_2 = \mathbf{F}_2(\mathbf{u})$, $\bar{\mathbf{F}}_2 = \mathbf{F}_2(\bar{\mathbf{u}})$ have been used. We can now continue our effort in deriving the x-layer equations by again introducing the moving-frame change of variables

$$\hat{x} = x \tag{62}$$

$$\hat{y} = y - V_0 t \tag{63}$$

$$\hat{t} = t \tag{64}$$

which gives

$$\frac{\partial \mathbf{u}'}{\partial \hat{t}} + \frac{\partial(\mathbf{F}_1 - \bar{\mathbf{F}}_1)}{\partial \hat{x}} + \frac{\partial(\mathbf{F}_2 - \bar{\mathbf{F}}_2 - V_0\mathbf{u}')}{\partial \hat{y}} = 0 \tag{65}$$

At this point the equation is equivalent to that with no vertical flow, and again we can employ previously established results, using the PML equations given in [33]:

$$\frac{\partial \mathbf{u}'}{\partial \hat{t}} + \frac{\partial(\mathbf{F}_1 - \bar{\mathbf{F}}_1)}{\partial \hat{x}} + \frac{\partial(\mathbf{F}_2 - \bar{\mathbf{F}}_2 - V_0\mathbf{u}')}{\partial \hat{y}} + \sigma_x \mathbf{q}_1 + \sigma_x \beta_x (\mathbf{F}_1 - \bar{\mathbf{F}}_1) = 0 \tag{66}$$

$$\frac{\partial \mathbf{q}_1}{\partial \hat{t}} + \frac{\partial(\mathbf{F}_1 - \bar{\mathbf{F}}_1)}{\partial \hat{x}} + \sigma_x \mathbf{q}_1 + \sigma_x \beta_x (\mathbf{F}_1 - \bar{\mathbf{F}}_1) = 0 \tag{67}$$

where

$$\beta_x = \frac{U_0}{1 - U_0^2} \tag{68}$$

and $\mathbf{q}_1$ is an auxiliary variable. Here, because we are dealing with only the x-layer in two dimensions, terms involving σ_y and terms involving the third dimension have been dropped from the equations given in [33]. After rewriting these equations in the original coordinates for space and time, the x-layer equations emerge:

$$\frac{\partial \mathbf{u}'}{\partial t} + \frac{\partial(\mathbf{F}_1 - \bar{\mathbf{F}}_1)}{\partial x} + \frac{\partial(\mathbf{F}_2 - \bar{\mathbf{F}}_2)}{\partial y} + \sigma_x \mathbf{q}_1 + \sigma_x \beta_x (\mathbf{F}_1 - \bar{\mathbf{F}}_1) = 0 \tag{69}$$

$$\frac{\partial \mathbf{q}_1}{\partial t} + \frac{\partial(\mathbf{F}_1 - \bar{\mathbf{F}}_1)}{\partial x} + V_0 \frac{\partial \mathbf{q}_1}{\partial y} + \sigma_x \mathbf{q}_1 + \sigma_x \beta_x (\mathbf{F}_1 - \bar{\mathbf{F}}_1) = 0 \tag{70}$$

In a similar manner, after using the moving frame

$$\hat{x} = x - U_0 t \tag{71}$$

$$\hat{y} = y \tag{72}$$

$$\hat{t} = t \tag{73}$$

the y-layer equations are found to be

$$\frac{\partial \mathbf{u}'}{\partial t} + \frac{\partial(\mathbf{F}_1 - \bar{\mathbf{F}}_1)}{\partial x} + \frac{\partial(\mathbf{F}_2 - \bar{\mathbf{F}}_2)}{\partial y} + \sigma_y \mathbf{q}_2 + \sigma_y \beta_y (\mathbf{F}_2 - \bar{\mathbf{F}}_2) = 0 \tag{74}$$

$$\frac{\partial \mathbf{q}_2}{\partial t} + U_0 \frac{\partial \mathbf{q}_2}{\partial x} + \frac{\partial(\mathbf{F}_2 - \bar{\mathbf{F}}_2)}{\partial y} + \sigma_y \mathbf{q}_2 + \sigma_y \beta_y (\mathbf{F}_2 - \bar{\mathbf{F}}_2) = 0 \tag{75}$$

where

$$\beta_y = \frac{V_0}{1 - V_0^2} \tag{76}$$

and $\mathbf{q}_2$ is another auxiliary variable.

The construction of corner layer equations again reduces to combining terms from the x- and y-layer equations, then introducing additional terms for stability. Using such a method, the corner layer equations are formed as

$$\frac{\partial \mathbf{u}'}{\partial t} + \frac{\partial(\mathbf{F}_1 - \bar{\mathbf{F}}_1)}{\partial x} + \frac{\partial(\mathbf{F}_2 - \bar{\mathbf{F}}_2)}{\partial y} + \sigma_x \mathbf{q}_1 + \sigma_y \mathbf{q}_2 + \sigma_x \beta_x (\mathbf{F}_1 - \bar{\mathbf{F}}_1) + \sigma_y \beta_y (\mathbf{F}_2 - \bar{\mathbf{F}}_2)$$
$$+ \sigma_x \sigma_y (\mathbf{u} - \bar{\mathbf{u}}) = 0 \tag{77}$$

$$\frac{\partial \mathbf{q}_1}{\partial t} + \frac{\partial(\mathbf{F}_1 - \bar{\mathbf{F}}_1)}{\partial x} + V_0 \frac{\partial \mathbf{q}_1}{\partial y} + (\sigma_x + \sigma_y)\mathbf{q}_1 + \sigma_x \beta_x (\mathbf{F}_1 - \bar{\mathbf{F}}_1) = 0 \tag{78}$$

$$\frac{\partial \mathbf{q}_2}{\partial t} + U_0 \frac{\partial \mathbf{q}_2}{\partial x} + \frac{\partial(\mathbf{F}_2 - \bar{\mathbf{F}}_2)}{\partial y} + (\sigma_x + \sigma_y)\mathbf{q}_2 + \sigma_y \beta_y (\mathbf{F}_2 - \bar{\mathbf{F}}_2) = 0 \tag{79}$$

In this case, the terms $\sigma_x \sigma_y (\mathbf{u} - \bar{\mathbf{u}})$, $\sigma_y \mathbf{q}_1$, and $\sigma_x \mathbf{q}_2$ have been added to equations (77), (78), and (79), respectively, to maintain the stability of the system. Again, upon setting σ_y or σ_x to zero, either the x- or y-layer equations can be quickly recovered. The next section tests the stability of the proposed corner equations.

III.2.2 STABILITY ANALYSIS FOR CORNER LAYERS

As was done for the linear case, the stability of the corner layer equations for the nonlinear case will be tested by substituting

$$\begin{pmatrix} \mathbf{u}' \\ \mathbf{q}_1 \\ \mathbf{q}_2 \end{pmatrix} = e^{i(k_x x + k_y y - \omega t)} \begin{pmatrix} \hat{\mathbf{u}} \\ \hat{\mathbf{q}}_1 \\ \hat{\mathbf{q}}_2 \end{pmatrix} \tag{80}$$

into the proposed equations (77)–(79), then analyzing the resulting eigenvalue problem for ω. In this case, however, because there is no straightforward way to analyze the stability of nonlinear equations, we will look at a linearized form of the equations by assuming

$$\mathbf{F}_1 - \bar{\mathbf{F}}_1 = \mathsf{A}\mathbf{u}', \ \mathbf{F}_2 - \bar{\mathbf{F}}_2 = \mathsf{B}\mathbf{u}' \tag{81}$$

where

$$\mathsf{A} = \begin{pmatrix} U_0 & 1 & 0 & 0 \\ 0 & U_0 & 0 & 1 \\ 0 & 0 & U_0 & 0 \\ 0 & 1 & 0 & U_0 \end{pmatrix}, \quad \mathsf{B} = \begin{pmatrix} V_0 & 0 & 1 & 0 \\ 0 & V_0 & 0 & 0 \\ 0 & 0 & V_0 & 1 \\ 0 & 0 & 1 & V_0 \end{pmatrix} \tag{82}$$

A linearized form of equations (77)-(79) is then given by

$$\frac{\partial \mathbf{u}'}{\partial t} + \mathsf{A}\frac{\partial \mathbf{u}'}{\partial x} + \mathsf{B}\frac{\partial \mathbf{u}'}{\partial y} + \sigma_x \mathbf{q}_1 + \sigma_y \mathbf{q}_2 + \sigma_x \beta_x \mathsf{A}\mathbf{u}' + \sigma_y \beta_y \mathsf{B}\mathbf{u}' + \sigma_x \sigma_y \mathbf{u}' = 0 \tag{83}$$

$$\frac{\partial \mathbf{q}_1}{\partial t} + \mathsf{A}\frac{\partial \mathbf{u}'}{\partial x} + V_0\frac{\partial \mathbf{q}_1}{\partial y} + (\sigma_x + \sigma_y)\mathbf{q}_1 + \sigma_x \beta_x \mathsf{A}\mathbf{u}' = 0 \tag{84}$$

$$\frac{\partial \mathbf{q}_2}{\partial t} + U_0\frac{\partial \mathbf{q}_2}{\partial x} + \mathsf{B}\frac{\partial \mathbf{u}'}{\partial y} + (\sigma_x + \sigma_y)\mathbf{q}_2 + \sigma_y \beta_y \mathsf{B}\mathbf{u}' = 0 \tag{85}$$

At this point, we can substitute the assumed wave form into the equations to analyze the stability. Again using the more compact notation

$$\mathbf{U} = \hat{\mathbf{U}} e^{i(k_x x + k_y y - \omega t)} \tag{86}$$

and remembering that

$$\frac{\partial \mathbf{U}}{\partial t} = -i\omega \mathbf{U} \tag{87}$$

$$\frac{\partial \mathbf{U}}{\partial x} = ik_x \mathbf{U} \tag{88}$$

$$\frac{\partial \mathbf{U}}{\partial y} = ik_y \mathbf{U} \tag{89}$$

we arrive at the system

$$\begin{pmatrix} (\mathrm{k}_x - i\sigma_x\beta_x)\mathsf{A} + (k_y - i\sigma_y\beta_y)\mathsf{B} - \mathrm{i}\sigma_x\sigma_y\mathsf{I} & -i\sigma_x\mathsf{I} & -i\sigma_y\mathsf{I} \\ (\mathrm{k}_x - i\sigma_x\beta_x)\mathsf{A} & (\mathrm{k}_y V_0 - i\sigma_x - i\sigma_y)\mathsf{I} & 0 \\ (\mathrm{k}_y - i\sigma_y\beta_y)\mathsf{B} & 0 & (\mathrm{k}_x U_0 - i\sigma_x - i\sigma_y)\mathsf{I} \end{pmatrix} \hat{\mathbf{U}}$$

$$= \omega \hat{\mathbf{U}} \tag{90}$$

or

$$\mathsf{Q}\hat{\mathbf{U}} = \omega \hat{\mathbf{U}} \tag{91}$$

where Q is the matrix in (90), and I is the four-dimensional identity matrix. Equation (91) is then our resulting eigenvalue problem for ω. If the imaginary part, ω_i, of the eigenvalue is nonpositive for every eigenvalue, then the equations will be dynamically stable.

The first effort in the analysis is to consider σ_x and σ_y as constants and examine the eigenvalues for velocities over the range $0 \leq U_0, V_0 \leq 0.95$. Figure 12 plots the contours of the maximum ω_i for $\sigma_x = \sigma_y = 2$ over wavenumbers $|k_x|, |k_y| \leq 20$. No positive ω_i is found, suggesting the corner equations are stable. The second effort

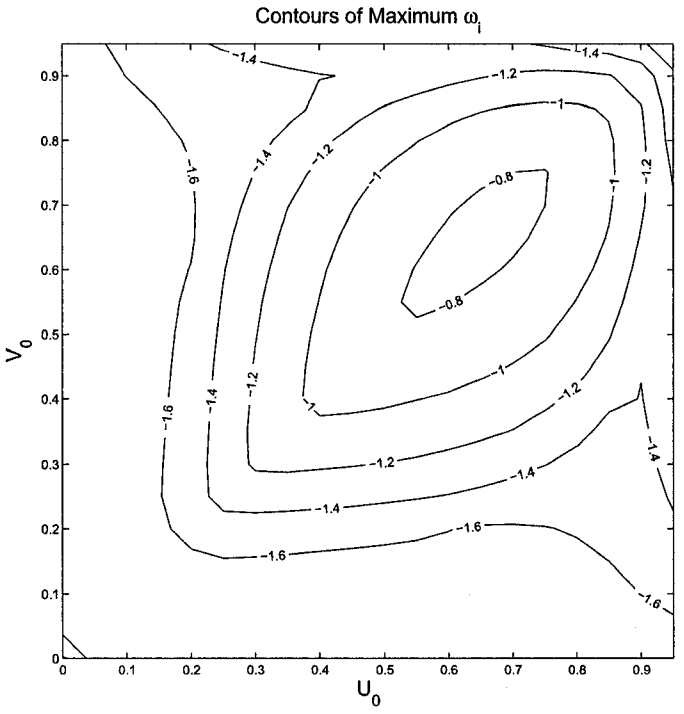

FIG. 12: Contours of maximum imaginary parts, ω_i, of eigenvalues for $\sigma_x = \sigma_y = 2$ over varying velocities.

is to consider U_0 and V_0 as constants and examine the eigenvalues for absorption coefficients in the range $|\sigma_x|, |\sigma_y| \leq 5$. Figure 13 plots the contours of the resulting maximum ω_i for $U_0 = V_0 = 0.5$ over wavenumbers $|k_x|, |k_y| \leq 20$. Again no positive ω_i is found, which further supports the assertion that the corner layer equations are stable.

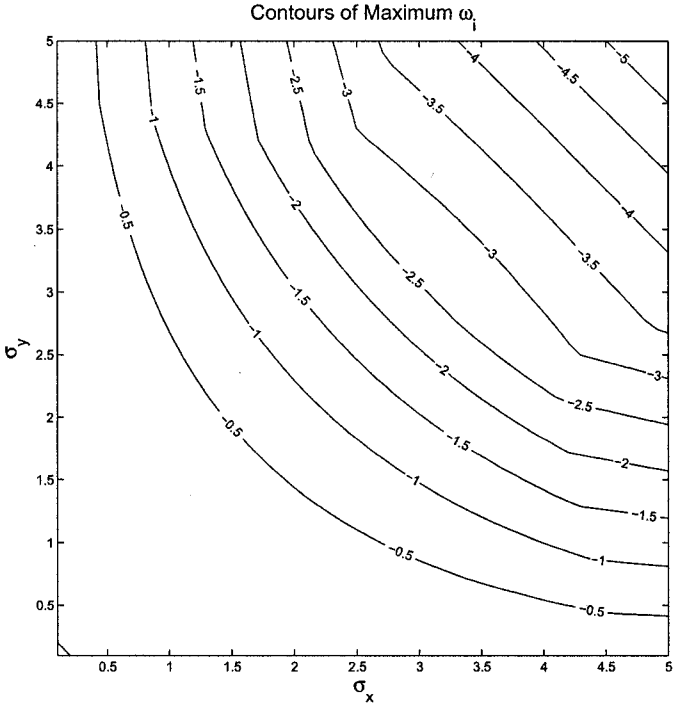

FIG. 13: Contours of maximum imaginary parts, ω_i, of eigenvalues for $U_0 = V_0 = 0.5$ over varying absorption coefficients.

III.2.3 NUMERICAL EXAMPLES

Isentropic Vortex

We will test the nonlinear PML equations for an exact solution of the nonlinear Euler equations, a convecting vortex of the form

$$\begin{pmatrix} \rho(\mathbf{x},t) \\ u(\mathbf{x},t) \\ v(\mathbf{x},t) \\ p(\mathbf{x},t) \end{pmatrix} = \begin{pmatrix} 0 \\ U_0 \\ V_0 \\ 0 \end{pmatrix} + \begin{pmatrix} \rho_r(r) \\ -u_r(r)\sin\theta \\ u_r(r)\cos\theta \\ p_r(r) \end{pmatrix} \tag{92}$$

where $r = \sqrt{(x - U_0 t)^2 + (y - V_0 t)^2}$, and for a given $u_r(r)$ and $\rho_r(r)$, the pressure $p_r(r)$ is given by

$$\frac{d}{dr} p_r(r) = \rho_r(r) \frac{u_r^2(r)}{r} \tag{93}$$

This solution to the nonlinear Euler equations advects with constant velocity (U_0, V_0). For this example, we will assume a velocity distribution of the form

$$u_r(r) = \frac{U'_{\max}}{b} r e^{\frac{1}{2}(1-\frac{r^2}{b^2})} \tag{94}$$

where $U'_{\max}$ is the maximum velocity of $u_r(r)$ at $r = b$. For isentropic flow, we enforce the relationship

$$p_r = \frac{1}{\gamma}\rho_r^\gamma \tag{95}$$

which leads to the following density and pressure distributions:

$$\rho_r(r) = \left(1 - \frac{1}{2}(\gamma-1)U'^2_{\max} e^{1-\frac{r^2}{b^2}}\right)^{1/(\gamma-1)} \tag{96}$$

$$p_r(r) = \frac{1}{\gamma}\left(1 - \frac{1}{2}(\gamma-1)U'^2_{\max} e^{1-\frac{r^2}{b^2}}\right)^{\gamma/(\gamma-1)} \tag{97}$$

Constant background velocity is taken to be $(U_0, V_0) = (0.5, 0.5)$, and in the above distributions, $U'_{\max} = 0.25$, $b = 0.2$, and $\gamma = 1.4$. The PML width is $D = 10\Delta x$, and the entire domain $[-1.2, 1.2] \times [-1.2, 1.2]$ is discretized by $\Delta x = \Delta y = 0.02$. Again the seven-point, fourth-order DRP scheme is used for spatial discretizations with periodic boundary closure schemes for derivatives in x and y. The four-stage LDDRK scheme is again used for time advancing, and the time step is restricted to $\Delta t = \frac{0.1}{1+\sqrt{2}}\Delta x$ for stability. The PML absorption coefficients, σ_x and σ_y, take the form of (45) with $\sigma_{max} = 20$ and $\alpha = 4$. In the PML region, grid stretching with stretch factors $\alpha(x) = 1 + 2\left|\frac{x-x_0}{D}\right|^2$ and $\alpha(y) = 1 + 2\left|\frac{y-y_0}{D}\right|^2$ is also added in the x- and y-directions, respectively, to increase the efficiency of the absorption [40]. Just as with the absorption coefficients, x_0 and y_0 are the locations of the PML-Euler interface for the x- and y-layers, respectively.

Figure 14 shows the contours of v-velocity at times $t = 0$, 1.5, 2.0 and 2.5. There are no apparent reflections. To test the accuracy, numerical solutions were compared with reference solutions computed on the larger domain $[-6.2, 6.2] \times [-6.2, 6.2]$. The top plot of Figure 15 shows the time history of the v-velocity component of the numerical and reference solutions at the point (0.9, 0.9). Very good agreement is seen between the two solutions. The bottom plot of Figure 15 is the difference between the numerical and reference solutions at the same point as a function of time. The

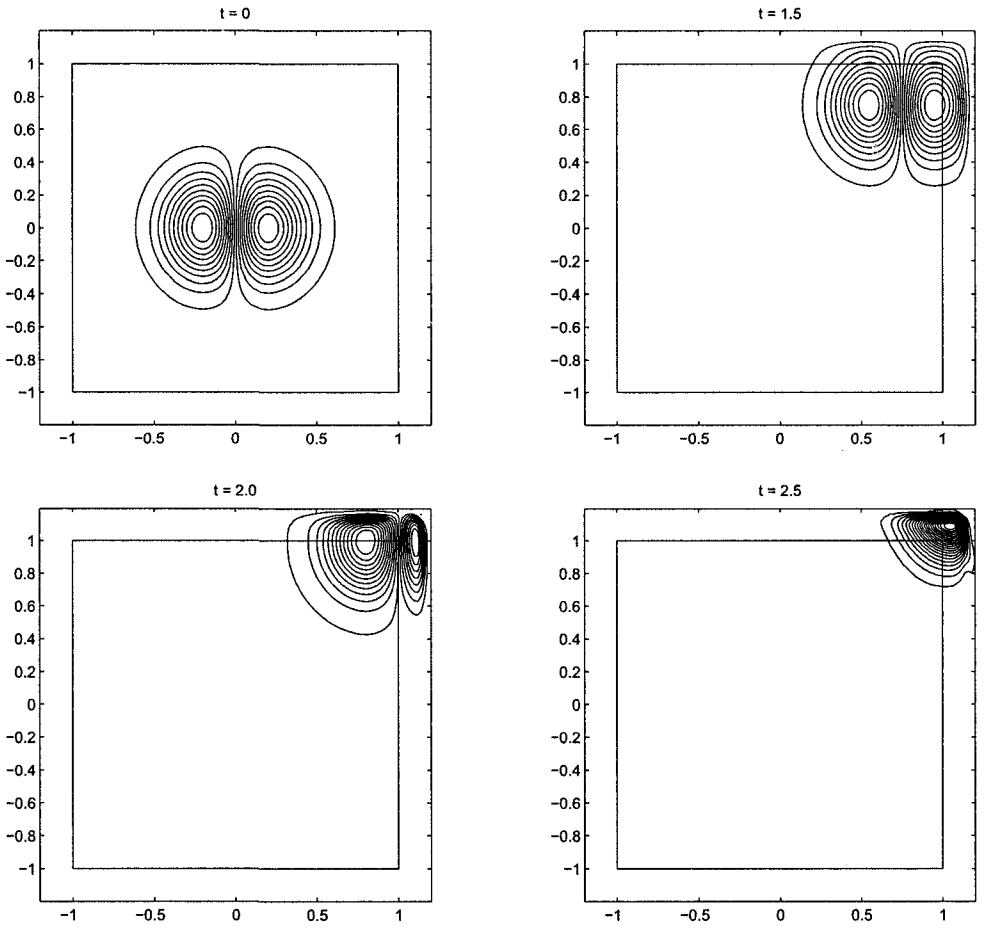

FIG. 14: Isentropic vortex: Contours of v-velocity at times $t = 0, 1.5, 2.0$, and 2.5.

magnitude of the difference is approximately 10^{-3}. The reflection coefficient for v-velocity is also calculated as the maximum difference between the PML and reference solutions along $x = \pm 0.9$ and $y = \pm 0.9$ normalized by the maximum amplitude of the given wave and plotted as a function of time, as shown in Figure 16.

Satisfactory results are also achieved for various cases of higher strength vortices. Taking $(U_0, V_0) = (0.2, 0.2)$, vortex strengths $U'_{\max} = 1.2U_0, 1.4U_0, 1.6U_0$ are tested. The maximum difference between PML and reference solutions for v-velocity is plotted in Figure 17 for each case. For comparison, the differences for the cases of weaker vortices, $U'_{\max} = 0.25U_0, 0.5U_0$, and $1.0U_0$ are also plotted. In general, the magnitude of the difference increases with the strength of the vortex. Note that when $U'_{\max} > U_0$,

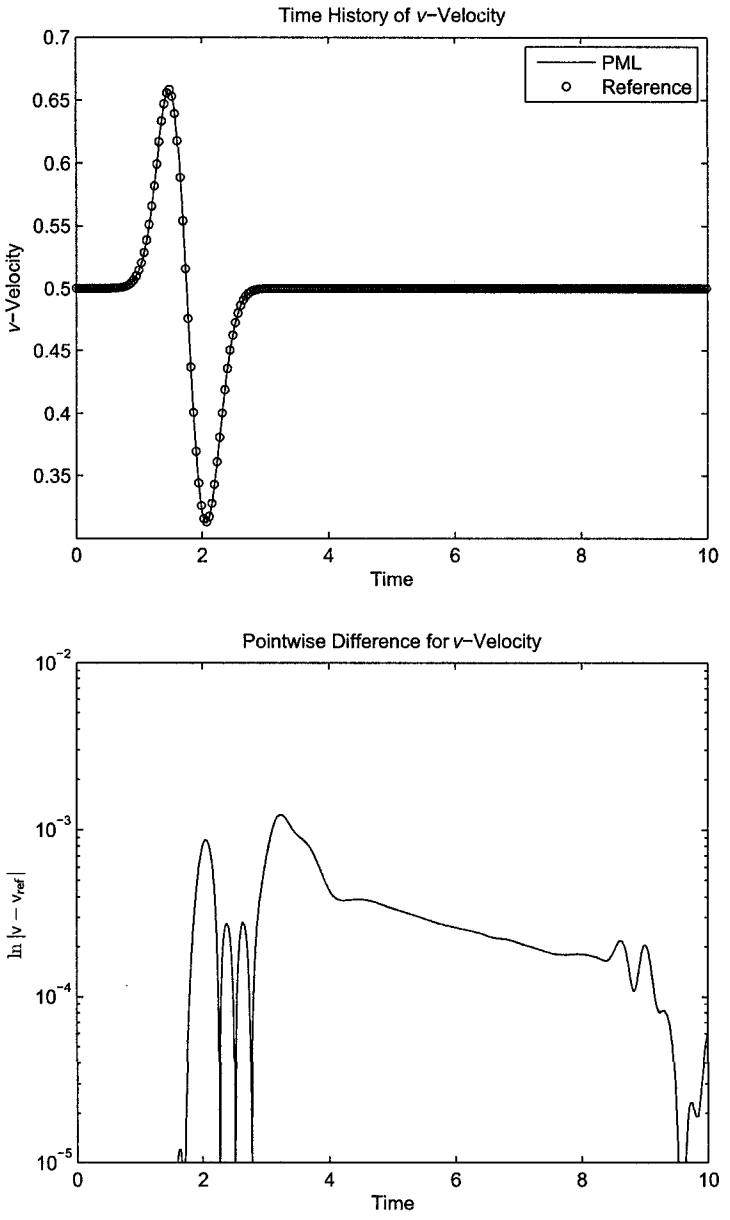

FIG. 15: Top: Solutions of v-velocity at the point (0.9, 0.9) as a function of time. Bottom: Difference between PML and reference solutions at (0.9, 0.9) as a function of time.

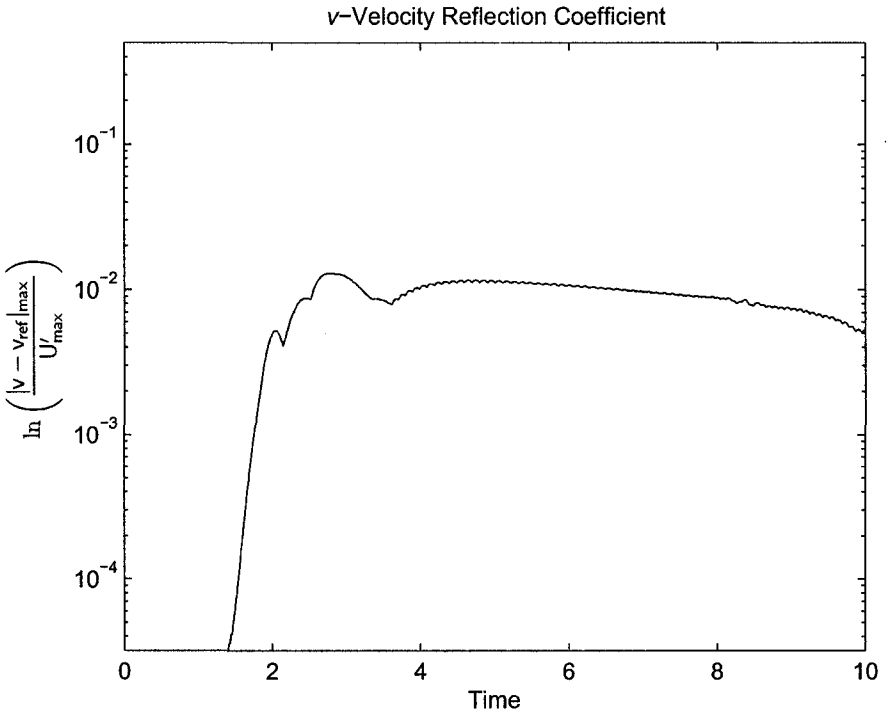

FIG. 16: Reflection coefficient for v-velocity versus time along $x = \pm 0.9$, $y = \pm 0.9$ for $U_0 = V_0 = 0.5$ and $U'_{\max} = 0.25$.

part of the vortex has a velocity opposite to the uniform background flow. When $U'_{\max}$ is small relative to U_0, difference levels are close to those of linearized cases.

Flow Over a Circular Cylinder

In this example, a circular cylinder of radius 0.5 is centered at the origin, and constant background flow is initially assumed. An overset grid approach, as explained in [48], is used to model viscous flow over a circular cylinder. A polar grid will be used around the cylinder to solve the Navier-Stokes equations. A Cartesian grid will capture the outgoing vortices shed off the cylinder, with the nonlinear Euler equations satisfied in the interior region, and the proposed PML equations satisfied in the PML region. A schematic of the overset grids is shown in Figure 18. Further references on overset grids and their applications are given in [49–51]. The polar domain is $r \in [0.5, 1.5]$, $\theta \in [0, 2\pi)$ with $\Delta r = 0.02$ and $\Delta\theta = \frac{\pi}{75}$. In this domain, the Reynolds number Re

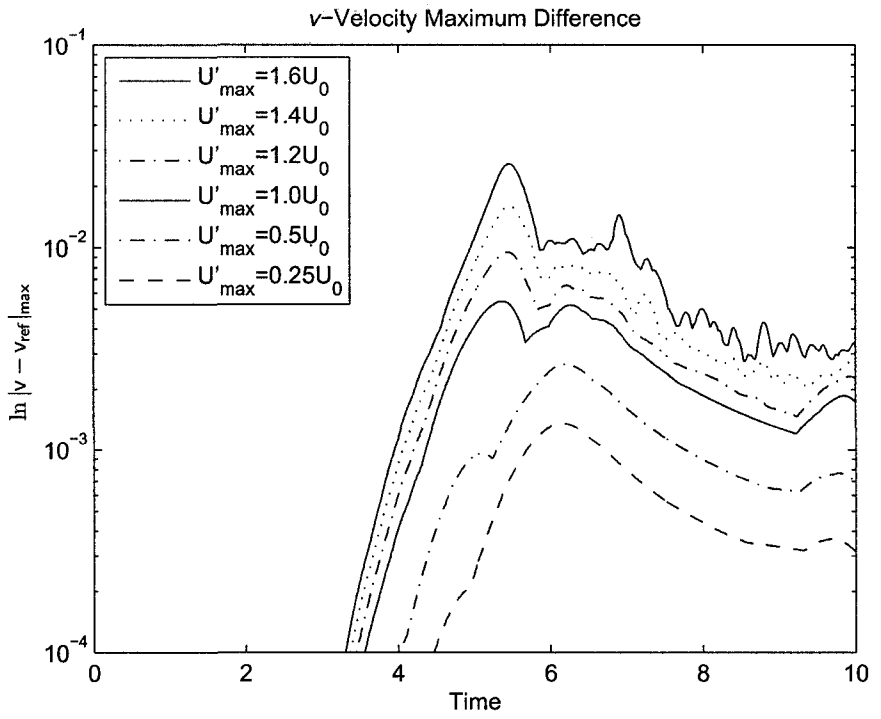

FIG. 17: Maximum difference between PML and reference solutions of v-velocity versus time along $x = \pm 0.9$, $y = \pm 0.9$ for $U_0 = V_0 = 0.2$ and varying $U'_{\max}$.

relative to the mean flow $M = \sqrt{U_0^2 + V_0^2}$ is taken to be $\frac{Re}{M} = 150$, and heat transfer terms are ignored. The interior Cartesian domain is $[-2, 6] \times [-2, 6]$ discretized by $\Delta x = \Delta y = 0.04$ and surrounded by a PML of width $D = 40\Delta x$. A sixteen-point interpolation scheme is used to update data between the two grids [48]. In both grids, the seven-point DRP and five-stage LDDRK schemes are used for spatial and temporal discretizations, respectively. Periodic boundary closure schemes are used for x, y, and θ derivatives, and a separate third-order boundary closure scheme is used for r derivatives. Grid stretching is again used in the PML region with stretch factors identical to those given in the previous example. In this example, the time step is chosen to be $\Delta t = \frac{0.5}{1+\sqrt{2}}\Delta r$, and initial background flow is taken as

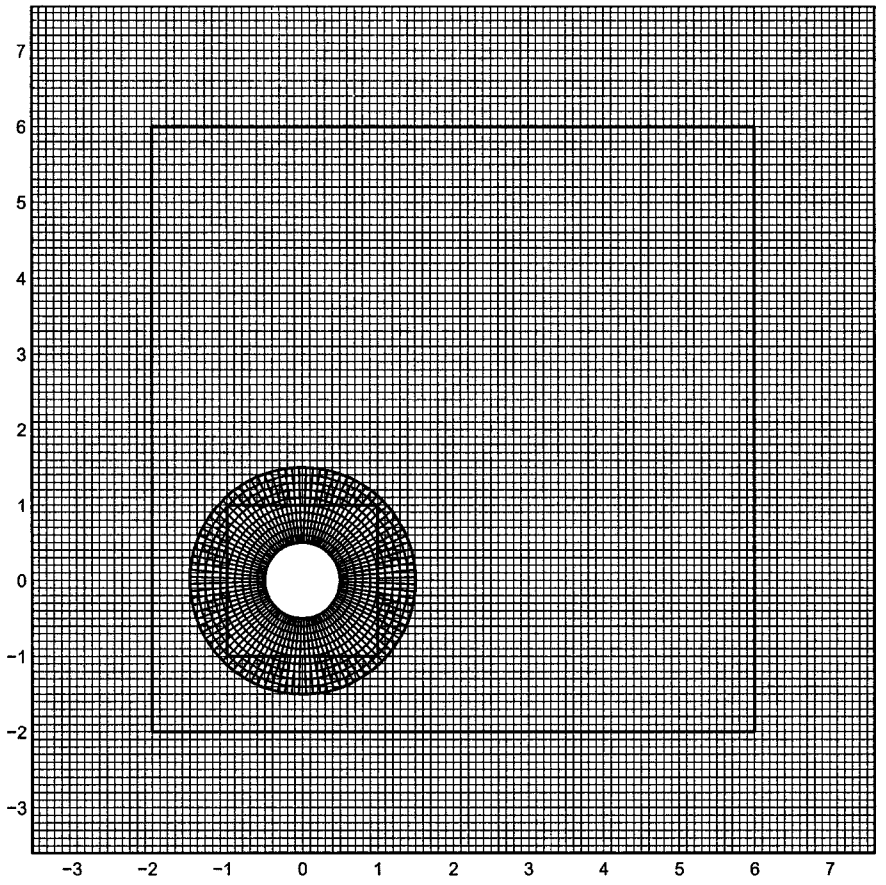

FIG. 18: Schematic of overset grids used. The polar grid is surrounded by a Cartesian grid. The Cartesian grid is then extended to include the PML region.

$$\begin{pmatrix} \rho \\ u \\ v \\ p \end{pmatrix} = \begin{pmatrix} 1 \\ 0.35 \\ 0.35 \\ \frac{1}{\gamma} \end{pmatrix} \tag{98}$$

where again $\gamma = 1.4$. For the PML absorption coefficients, σ_x and σ_y, $\sigma_{max} = 20$ and $\alpha = 4$ are chosen in the form (45).

Figure 19 shows the formation of the transient pressure pulse in a sequence of contour plots of density at times $t = 2, 3, 4$ and 5. It is clear that the outgoing wave is

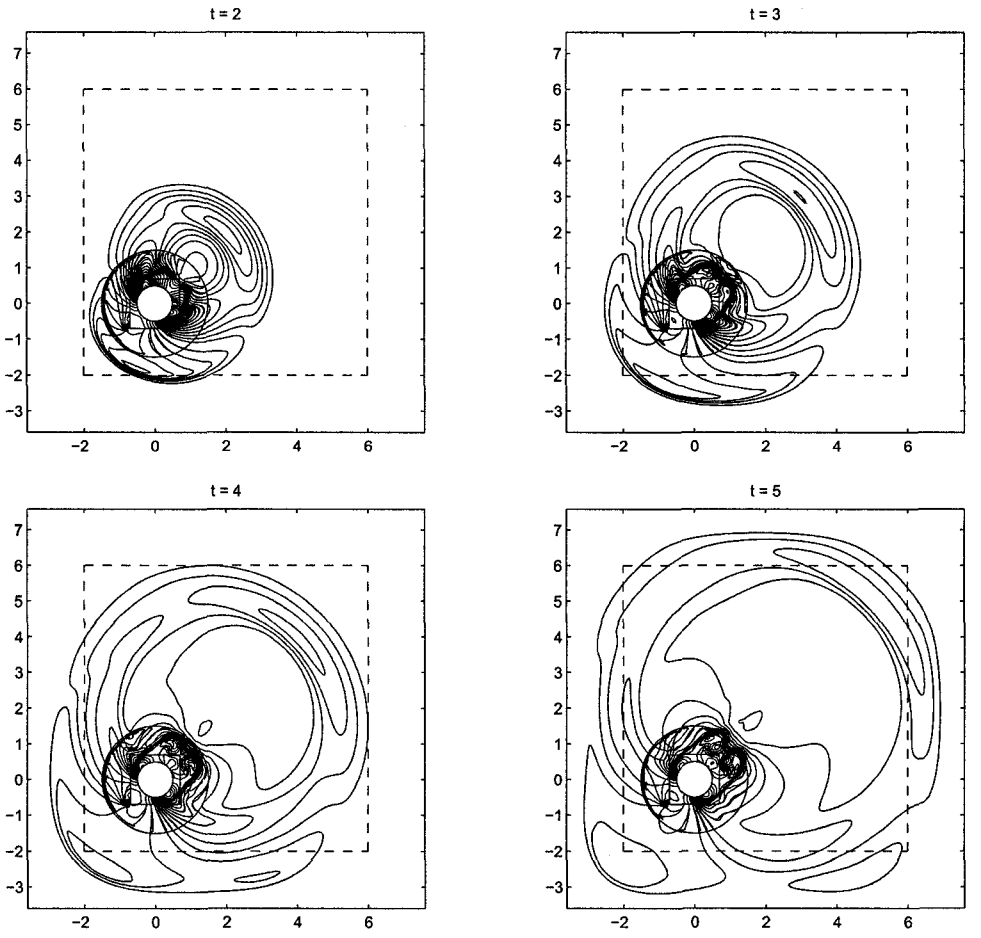

FIG. 19: Flow over a circular cylinder: Contours of density during the formation of the transient pressure pulse. Times $t = 2, 3, 4$, and 5 are shown.

being absorbed by the PML. Figures 20–23 show the final absorption of the transient pulse and the formation of vortices as flow moves over the cylinder. Contours for both the numerical and reference solutions are shown at times $t = 6$, 30, 35, and 150. Reference solutions are calculated on the larger domain $[-2, 14] \times [-2, 14]$. At $t = 6$, the transient pulse has just exited the domain. By $t = 30$, the first shed vortex is reaching the PML-Euler interface, and by $t = 35$, the vortex has been absorbed by the PML. At $t = 150$, vortices continue to exit the domain and appear to be absorbed well by the PML.

To evaluate the effectiveness of the absorption of exiting waves, comparisons are

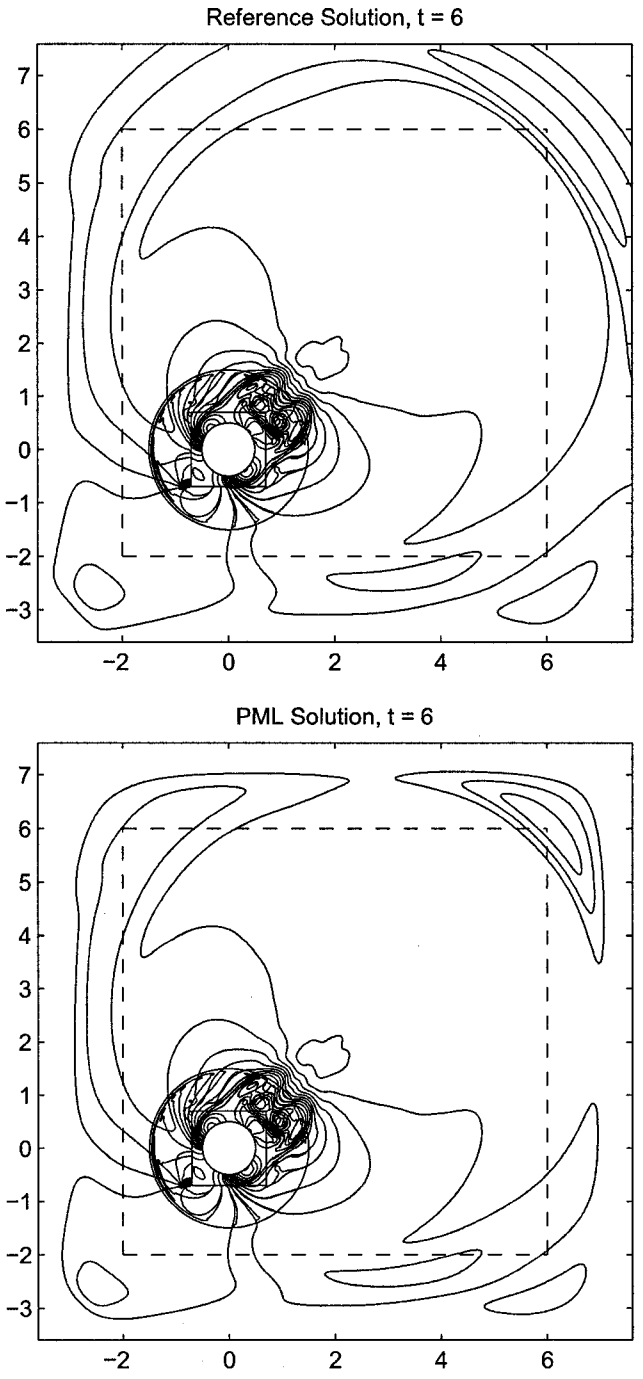

FIG. 20: Transient pressure pulse: Contours of density at time $t = 6$.

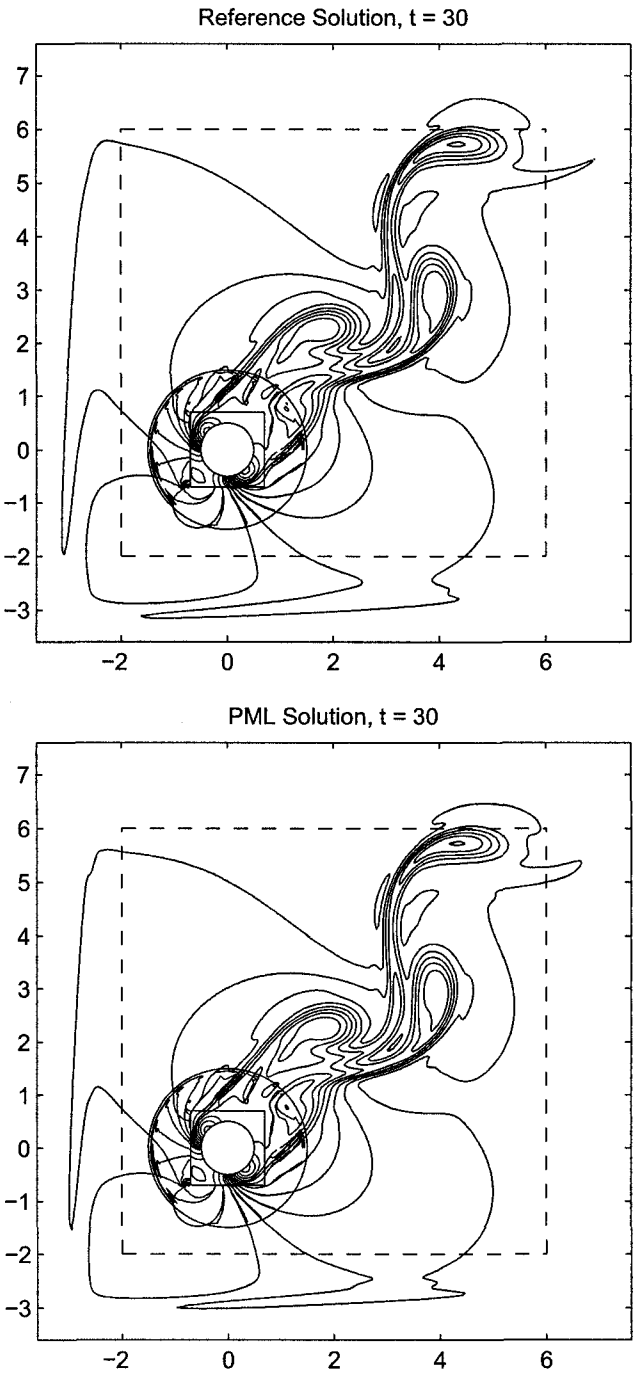

FIG. 21: Vortex shedding: Contours of density at time $t = 30$.

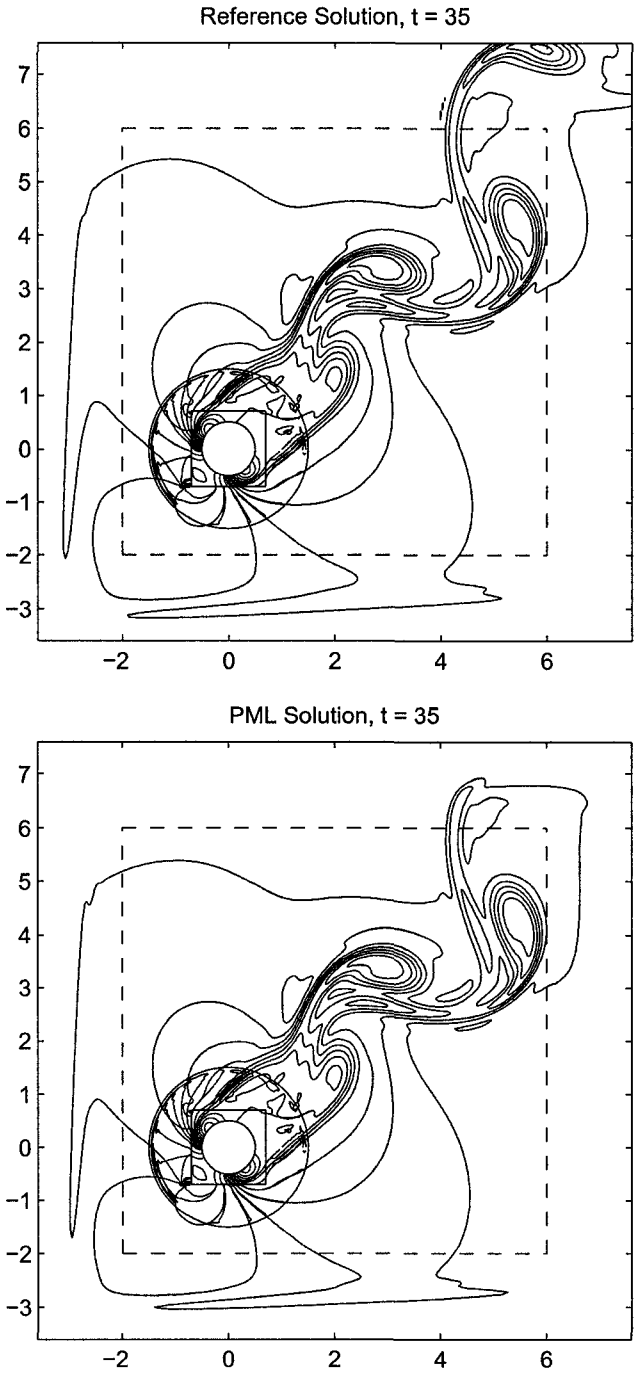

FIG. 22: Vortex shedding: Contours of density at time $t = 35$.

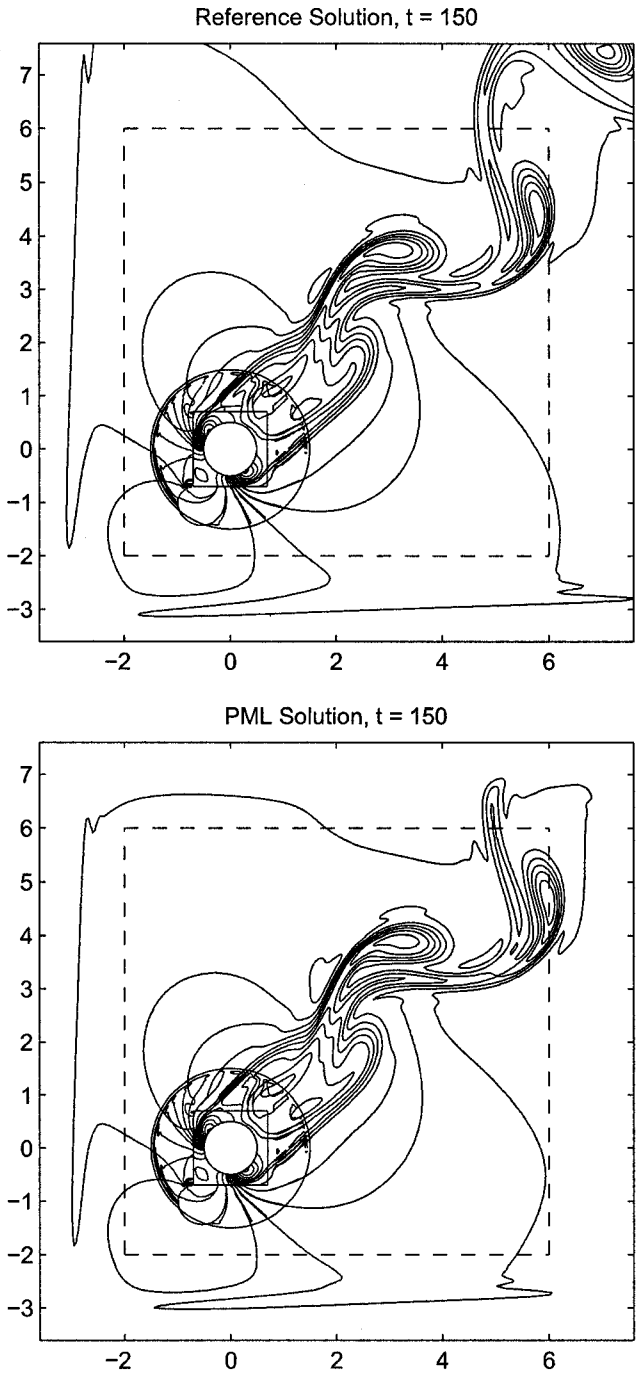

FIG. 23: Vortex shedding: Contours of density at time $t = 150$.

made between the PML and reference solutions at the single corner point $(5.8, 5.8)$. The top of Figure 24 shows the time history of v-velocity at that point. Very good agreement is seen between the PML and reference solutions for the transient pressure pulse, which is an indication of the effectiveness of the boundary condition. The bottom plot shows the difference between the two solutions at the same point as a function of time. For comparison, the differences for PML widths $D = 20\Delta x$ and $D = 60\Delta x$ are also included in the plot. Comparisons are also made over the range of values $x = 5.8,\ y \in [2, 5.8]$ and $x \in [2, 5.8],\ y = 5.8$. Because the reference domain was only expanded on the right and top boundaries, comparison points were focused toward the upper right corner. Figure 25 plots the maximum difference between numerical and reference solutions as a function of time for PML widths of $D = 20\Delta x$, $40\Delta x$, and $60\Delta x$. It is clear that the initial transient pressure pulse is absorbed well with little reflection for each PML width and that an increase in the width of the PML corresponds to a decrease in reflection error.

In both Figures 24 and 25, as the vortices created by shedding begin to reach the edge of the domain, a significant increase in the maximum differences is observed. This can be attributed to the effects of domain truncation on the behavior of the physical system. If the domain is truncated too aggressively, the truncation can, in essence, cut off physical occurrences, such as turbulent-like behavior, that would have happened farther down stream from the source, and which, left unaltered, would have affected the solutions closer to the source. The solutions from the smaller truncated domain and the solutions from the larger domain are therefore representing slightly different physical situations in regards to the nonlinear behavior. This is most likely the cause of the discrepancies between the PML and reference solutions in the secondary portion of the error plots. Ideally, the PML solution would be computed on the larger domain, and a further expanded domain would be used for reference. However, due to time constraints and limitations on available computing resources, this work has not been carried out. Further, computations of such magnitude would most effectively be implemented with the use of parallel computing, which is outside the scope of this paper. Regardless, even for this latter portion, Figure 25 shows that an increase in PML width results in a general decrease in the maximum difference, behavior indicative of the perfect matching of the boundary condition.

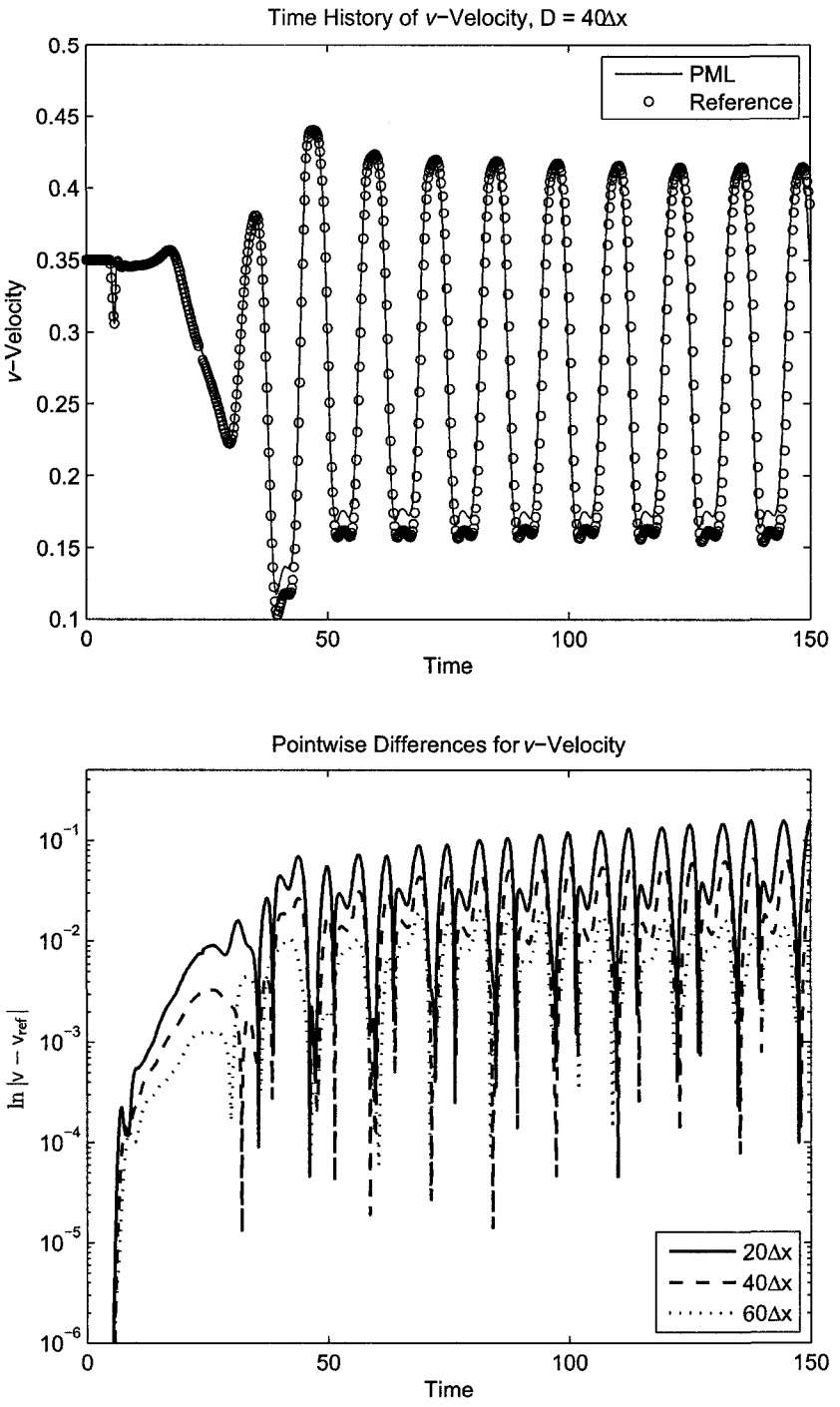

FIG. 24: Top: Time history of v-velocity at the point $(5.8, 5.8)$ for PML of width $D = 40\Delta x$ against a reference solution. Bottom: Differences between PML and reference solutions for v-velocity versus time at the point $(5.8, 5.8)$ for PML widths $D = 20\Delta x$, $40\Delta x$, and $60\Delta x$.

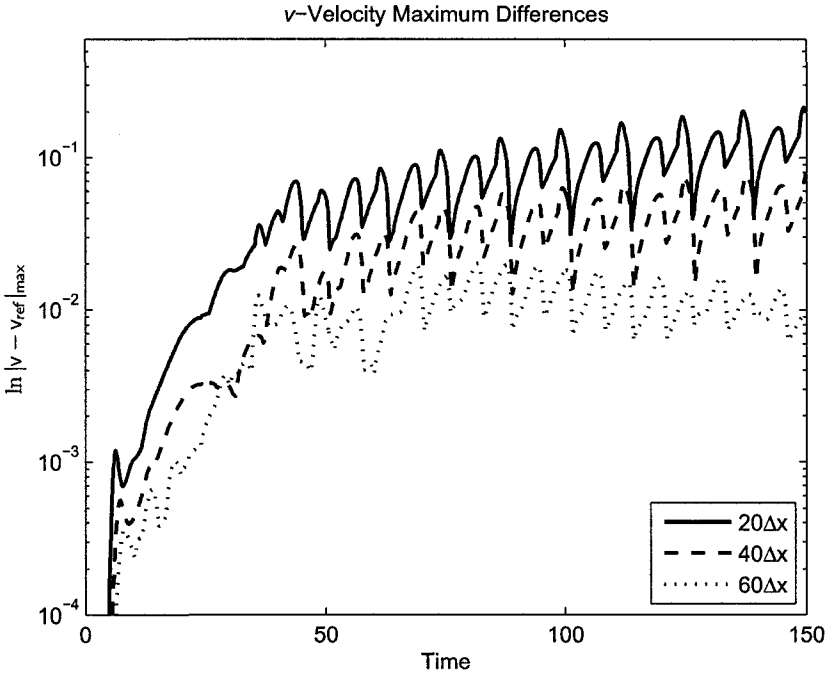

FIG. 25: Maximum differences between PML and reference solutions for v-velocity versus time along $x = 5.8$, $y \in [2, 5.8]$ and $x \in [2, 5.8]$, $y = 5.8$ for PML widths $D = 20\Delta x$, $40\Delta x$, and $60\Delta x$.

CHAPTER IV

PML IN CYLINDRICAL COORDINATES

Because certain physical problems are better suited for representation in a cylindrical coordinate system, it is important to develop a PML boundary condition in cylindrical coordinates. Further, because interior schemes already exist in cylindrical coordinates, it is useful to provide a high-accuracy boundary condition to accompany these schemes. Despite its importance, however, very little work has been done on the cylindrical PML, particularly in the field of acoustics. In light of this, the present chapter will focus on providing the much needed boundary condition in the cylindrical coordinate system, first for the nonlinear Euler equations in conservation form with horizontal mean flow, and second for the linearized Euler equations in primitive variables with horizontal mean flow. Both conservation and primitive variables are presented so that interior schemes that have already been implemented with either type of variable can easily incorporate the PML boundary condition. Finally, the cylindrical PML equations are generalized to accommodate mean flow in an arbitrary direction. The derivation differs from that of the Cartesian PML in that independent side and corner layers are no longer needed to handle an oblique mean flow. Once stability is achieved for the horizontal case, the stability for the oblique case will automatically follow. This results because the PML for the oblique case and that of the horizontal case differ only by a simple rotation of coordinates. Therefore, only a single set of equations is needed in the entire PML region. As will be seen, the stability of the PML equations for horizontal mean flow follows from a proper space-time transformation, applied prior to the PML change of variables. Then, as mentioned, the equations for oblique mean flow are easily found with the single additional task of rotating the coordinate system.

IV.1 NONLINEAR EULER EQUATIONS IN CONSERVATION FORM

IV.1.1 PML FORMULATION

Our first effort in deriving PML equations for cylindrical coordinates will be for the case of flow in a single dimension, namely the x-direction. The boundary condition will be derived for the nonlinear Euler equations in conservation form, given by

$$\frac{\partial \mathbf{u}}{\partial t} + \cos\theta \frac{\partial \mathbf{F}_1(\mathbf{u})}{\partial r} - \frac{\sin\theta}{r}\frac{\partial \mathbf{F}_1(\mathbf{u})}{\partial \theta} + \sin\theta \frac{\partial \mathbf{F}_2(\mathbf{u})}{\partial r} + \frac{\cos\theta}{r}\frac{\partial \mathbf{F}_2(\mathbf{u})}{\partial \theta} = 0 \tag{99}$$

where

$$\mathbf{u} = \begin{pmatrix} \rho \\ \rho u \\ \rho v \\ \rho e \end{pmatrix} \mathbf{F}_1(\mathbf{u}) = \begin{pmatrix} \rho u \\ \rho u^2 + p \\ \rho uv \\ \rho hu \end{pmatrix}, \ \mathbf{F}_2(\mathbf{u}) = \begin{pmatrix} \rho v \\ \rho uv \\ \rho v^2 + p \\ \rho hv \end{pmatrix} \tag{100}$$

with

$$h = e + \frac{p}{\rho}, \ p = (\gamma - 1)\rho\left(e - \frac{u^2 + v^2}{2}\right) \tag{101}$$

and ρ is density, u and v are velocity components, e is the energy, p is the pressure, and γ is the specific heat ratio. However, although our ultimate goal is to form PML equations in cylindrical coordinates, our derivation will begin with the nonlinear Euler equations in Cartesian coordinates, as given in (56). This time we assume a constant background flow of $(U_0, 0)$. We begin the derivation by partitioning the solution into two parts as follows:

$$\mathbf{u} = \bar{\mathbf{u}} + \mathbf{u}' \tag{102}$$

where $\mathbf{u}'$ is the time-dependent component of $\mathbf{u}$, and $\bar{\mathbf{u}}$ is the time-independent component that satisfies the steady Euler equations (60). Again, this is done to minimize computational effort, as the size of the total variable $\mathbf{u}$ is often much larger than the size of the fluctuation $\mathbf{u}'$. Equation (56) then becomes

$$\frac{\partial \mathbf{u}'}{\partial t} + \frac{\partial(\mathbf{F}_1 - \bar{\mathbf{F}}_1)}{\partial x} + \frac{\partial(\mathbf{F}_2 - \bar{\mathbf{F}}_2)}{\partial y} = 0 \tag{103}$$

where the shorthand notations $\mathbf{F}_1 = \mathbf{F}_1(\mathbf{u})$, $\bar{\mathbf{F}}_1 = \mathbf{F}_1(\bar{\mathbf{u}})$, $\mathbf{F}_2 = \mathbf{F}_2(\mathbf{u})$, $\bar{\mathbf{F}}_2 = \mathbf{F}_2(\bar{\mathbf{u}})$ have been used. We now rewrite the equation in cylindrical coordinates to get

$$\frac{\partial \mathbf{u}'}{\partial t} + \cos\theta \frac{\partial(\mathbf{F}_1 - \bar{\mathbf{F}}_1)}{\partial r} - \frac{\sin\theta}{r}\frac{\partial(\mathbf{F}_1 - \bar{\mathbf{F}}_1)}{\partial \theta} + \sin\theta \frac{\partial(\mathbf{F}_2 - \bar{\mathbf{F}}_2)}{\partial r} + \frac{\cos\theta}{r}\frac{\partial(\mathbf{F}_2 - \bar{\mathbf{F}}_2)}{\partial \theta} = 0 \tag{104}$$

where the well-known transformations

$$\frac{\partial}{\partial x} = \cos\theta \frac{\partial}{\partial r} - \frac{\sin\theta}{r}\frac{\partial}{\partial \theta} \tag{105}$$

$$\frac{\partial}{\partial y} = \sin\theta \frac{\partial}{\partial r} + \frac{\cos\theta}{r}\frac{\partial}{\partial \theta} \tag{106}$$

have been used. Recall from Section II.2.1, that in the presence of mean flow, inconsistencies arise in the phase and group velocities of acoustic waves. These inconsistencies must be corrected before the PML change of variable is applied, otherwise the system will not be stable. Because the mean flow is assumed only in the horizontal direction, the dispersion relations for the linearized form of equation (104) are the same as those given in (6) and (7), and a single transformation will therefore be sufficient to remove any inconsistencies in the phase and group velocities. Specifically, the transformation (11) will be used, with x expanded as a function of r and θ, or

$$\hat{t} = t + \beta_x r\cos\theta \tag{107}$$

$$\hat{r} = r \tag{108}$$

$$\hat{\theta} = \theta \tag{109}$$

which gives

$$\frac{\partial}{\partial t} = \frac{\partial}{\partial \hat{t}} \tag{110}$$

$$\frac{\partial}{\partial r} = \frac{\partial}{\partial \hat{r}} + \beta_x \cos\hat{\theta}\frac{\partial}{\partial \hat{t}} \tag{111}$$

$$\frac{\partial}{\partial \theta} = \frac{\partial}{\partial \hat{\theta}} - \beta_x \hat{r}\sin\hat{\theta}\frac{\partial}{\partial \hat{t}} \tag{112}$$

where

$$\beta_x = \frac{U_0}{1-U_0^2} \tag{113}$$

After applying such a transformation, our equation becomes

$$\frac{\partial \mathbf{u}'}{\partial \hat{t}} + \cos\hat{\theta}\left[\frac{\partial(\mathbf{F}_1 - \bar{\mathbf{F}}_1)}{\partial \hat{r}} + \beta_x\cos\hat{\theta}\frac{\partial(\mathbf{F}_1 - \bar{\mathbf{F}}_1)}{\partial \hat{t}}\right]$$

$$-\frac{\sin\hat{\theta}}{\hat{r}}\left[\frac{\partial(\mathbf{F}_1 - \bar{\mathbf{F}}_1)}{\partial \hat{\theta}} - \beta_x\hat{r}\sin\hat{\theta}\frac{\partial(\mathbf{F}_1 - \bar{\mathbf{F}}_1)}{\partial \hat{t}}\right]$$

$$+\sin\hat{\theta}\left[\frac{\partial(\mathbf{F}_2 - \bar{\mathbf{F}}_2)}{\partial \hat{r}} + \beta_x\cos\hat{\theta}\frac{\partial(\mathbf{F}_2 - \bar{\mathbf{F}}_2)}{\partial \hat{t}}\right]$$

$$+\frac{\cos\hat{\theta}}{\hat{r}}\left[\frac{\partial(\mathbf{F}_2-\bar{\mathbf{F}}_2)}{\partial\hat{\theta}}-\beta_x\hat{r}\sin\hat{\theta}\frac{\partial(\mathbf{F}_2-\bar{\mathbf{F}}_2)}{\partial\hat{t}}\right]=0 \tag{114}$$

At this point, we are ready to apply the PML change of variable in the frequency domain. Our equation (114) in the frequency domain is

$$(-i\omega)\tilde{\mathbf{u}}'+\cos\hat{\theta}\left[\frac{\partial(\widetilde{\mathbf{F}_1-\bar{\mathbf{F}}_1})}{\partial\hat{r}}+\beta_x\cos\hat{\theta}(-i\omega)(\widetilde{\mathbf{F}_1-\bar{\mathbf{F}}_1})\right]$$

$$-\frac{\sin\hat{\theta}}{\hat{r}}\left[\frac{\partial(\widetilde{\mathbf{F}_1-\bar{\mathbf{F}}_1})}{\partial\hat{\theta}}-\beta_x\hat{r}\sin\hat{\theta}(-i\omega)(\widetilde{\mathbf{F}_1-\bar{\mathbf{F}}_1})\right]$$

$$+\sin\hat{\theta}\left[\frac{\partial(\widetilde{\mathbf{F}_2-\bar{\mathbf{F}}_2})}{\partial\hat{r}}+\beta_x\cos\hat{\theta}(-i\omega)(\widetilde{\mathbf{F}_2-\bar{\mathbf{F}}_2})\right]$$

$$+\frac{\cos\hat{\theta}}{\hat{r}}\left[\frac{\partial(\widetilde{\mathbf{F}_2-\bar{\mathbf{F}}_2})}{\partial\hat{\theta}}-\beta_x\hat{r}\sin\hat{\theta}(-i\omega)(\widetilde{\mathbf{F}_2-\bar{\mathbf{F}}_2})\right]=0 \tag{115}$$

This time, the PML change of variable will be a transformation on the spatial variable $\hat{r}$ and is given by

$$\hat{r}\rightarrow\hat{r}+\frac{i}{\omega}\int_{\hat{r}_0}^{\hat{r}}\sigma_{\hat{r}}\,d\hat{r} \tag{116}$$

which gives

$$\frac{\partial}{\partial\hat{r}}\rightarrow\frac{1}{1+i\frac{\sigma_{\hat{r}}}{\omega}}\frac{\partial}{\partial\hat{r}} \tag{117}$$

The equation then becomes

$$(-i\omega)\tilde{\mathbf{u}}'+\cos\hat{\theta}\left[\frac{1}{1+i\frac{\sigma_{\hat{r}}}{\omega}}\frac{\partial(\widetilde{\mathbf{F}_1-\bar{\mathbf{F}}_1})}{\partial\hat{r}}+\beta_x\cos\hat{\theta}(-i\omega)(\widetilde{\mathbf{F}_1-\bar{\mathbf{F}}_1})\right]$$

$$-\frac{\sin\hat{\theta}}{\hat{r}+\frac{i}{\omega}\int_{\hat{r}_0}^{\hat{r}}\sigma_{\hat{r}}\,d\hat{r}}\left[\frac{\partial(\widetilde{\mathbf{F}_1-\bar{\mathbf{F}}_1})}{\partial\hat{\theta}}-\beta_x\left(\hat{r}+\frac{i}{\omega}\int_{\hat{r}_0}^{\hat{r}}\sigma_{\hat{r}}\,d\hat{r}\right)\sin\hat{\theta}(-i\omega)(\widetilde{\mathbf{F}_1-\bar{\mathbf{F}}_1})\right]$$

$$+\sin\hat{\theta}\left[\frac{1}{1+i\frac{\sigma_{\hat{r}}}{\omega}}\frac{\partial(\widetilde{\mathbf{F}_2-\bar{\mathbf{F}}_2})}{\partial\hat{r}}+\beta_x\cos\hat{\theta}(-i\omega)(\widetilde{\mathbf{F}_2-\bar{\mathbf{F}}_2})\right]$$

$$+\frac{\cos\hat{\theta}}{\hat{r}+\frac{i}{\omega}\int_{\hat{r}_0}^{\hat{r}}\sigma_{\hat{r}}\,d\hat{r}}\left[\frac{\partial(\widetilde{\mathbf{F}_2-\bar{\mathbf{F}}_2})}{\partial\hat{\theta}}-\beta_x\left(\hat{r}+\frac{i}{\omega}\int_{\hat{r}_0}^{\hat{r}}\sigma_{\hat{r}}\,d\hat{r}\right)\sin\hat{\theta}(-i\omega)(\widetilde{\mathbf{F}_2-\bar{\mathbf{F}}_2})\right]=0 \tag{118}$$

To simplify the conversion back to the time domain, we introduce a decomposition of $\mathbf{u}'$ into two auxiliary variables, $\mathbf{q}_1$ and $\mathbf{q}_2$. That is,

$$\mathbf{u}'=\mathbf{q}_1+\mathbf{q}_2 \tag{119}$$

In this way, the equation for $\mathbf{u}'$ (118) can be split into individual equations for $\mathbf{q}_1$ and $\mathbf{q}_2$ as follows:

$$(-i\omega)\tilde{\mathbf{q}}_1+\cos\hat{\theta}\left[\frac{1}{1+i\frac{\sigma_{\hat{r}}}{\omega}}\frac{\partial(\widetilde{\mathbf{F}_1-\bar{\mathbf{F}}_1})}{\partial\hat{r}}+\beta_x\cos\hat{\theta}(-i\omega)(\widetilde{\mathbf{F}_1-\bar{\mathbf{F}}_1})\right]$$

$$+\sin\hat{\theta}\left[\frac{1}{1+i\frac{\sigma_{\hat{r}}}{\omega}}\frac{\partial(\widetilde{\mathbf{F}_2-\bar{\mathbf{F}}_2})}{\partial\hat{r}}+\beta_x\cos\hat{\theta}(-i\omega)(\widetilde{\mathbf{F}_2-\bar{\mathbf{F}}_2})\right]=0 \tag{120}$$

$$(-i\omega)\tilde{\mathbf{q}}_2{}'-\frac{\sin\hat{\theta}}{\hat{r}+\frac{i}{\omega}\int_{\hat{r}_0}^{\hat{r}}\sigma_{\hat{r}}\,d\hat{r}}\left[\frac{\partial(\widetilde{\mathbf{F}_1-\bar{\mathbf{F}}_1})}{\partial\hat{\theta}}-\beta_x\left(\hat{r}+\frac{i}{\omega}\int_{\hat{r}_0}^{\hat{r}}\sigma_{\hat{r}}\,d\hat{r}\right)\sin\hat{\theta}(-i\omega)(\widetilde{\mathbf{F}_1-\bar{\mathbf{F}}_1})\right]$$

$$+\frac{\cos\hat{\theta}}{\hat{r}+\frac{i}{\omega}\int_{\hat{r}_0}^{\hat{r}}\sigma_{\hat{r}}\,d\hat{r}}\left[\frac{\partial(\widetilde{\mathbf{F}_2-\bar{\mathbf{F}}_2})}{\partial\hat{\theta}}-\beta_x\left(\hat{r}+\frac{i}{\omega}\int_{\hat{r}_0}^{\hat{r}}\sigma_{\hat{r}}\,d\hat{r}\right)\sin\hat{\theta}(-i\omega)(\widetilde{\mathbf{F}_2-\bar{\mathbf{F}}_2})\right]=0 \tag{121}$$

The complex fractions can now be easily cleared by multiplying equations (120) and (121) respectively by $(1+i\frac{\sigma_{\hat{r}}}{\omega})$ and $(\hat{r}+\frac{i}{\omega}\int_{\hat{r}_0}^{\hat{r}}\sigma_{\hat{r}}\,d\hat{r})$, which gives

$$(-i\omega+\sigma_{\hat{r}})\tilde{\mathbf{q}}_1+\cos\hat{\theta}\frac{\partial(\widetilde{\mathbf{F}_1-\bar{\mathbf{F}}_1})}{\partial\hat{r}}+\beta_x\cos^2\hat{\theta}(-i\omega+\sigma_{\hat{r}})(\widetilde{\mathbf{F}_1-\bar{\mathbf{F}}_1})$$

$$+\sin\hat{\theta}\frac{\partial(\widetilde{\mathbf{F}_2-\bar{\mathbf{F}}_2})}{\partial\hat{r}}+\beta_x\sin\hat{\theta}\cos\hat{\theta}(-i\omega+\sigma_{\hat{r}})(\widetilde{\mathbf{F}_2-\bar{\mathbf{F}}_2})=0 \tag{122}$$

$$\left(-i\omega\hat{r}+\int_{\hat{r}_0}^{\hat{r}}\sigma_{\hat{r}}\,d\hat{r}\right)\tilde{\mathbf{q}}_2-\sin\hat{\theta}\frac{\partial(\widetilde{\mathbf{F}_1-\bar{\mathbf{F}}_1})}{\partial\hat{\theta}}+\beta_x\sin^2\hat{\theta}\left(-i\omega\hat{r}+\int_{\hat{r}_0}^{\hat{r}}\sigma_{\hat{r}}\,d\hat{r}\right)(\widetilde{\mathbf{F}_1-\bar{\mathbf{F}}_1})$$

$$+\cos\hat{\theta}\frac{\partial(\widetilde{\mathbf{F}_2-\bar{\mathbf{F}}_2})}{\partial\hat{\theta}}-\beta_x\cos\hat{\theta}\sin\hat{\theta}\left(-i\omega\hat{r}+\int_{\hat{r}_0}^{\hat{r}}\sigma_{\hat{r}}\,d\hat{r}\right)(\widetilde{\mathbf{F}_2-\bar{\mathbf{F}}_2})=0 \tag{123}$$

At this point, the equations can be converted back to the time domain, giving

$$\frac{\partial\mathbf{q}_1}{\partial\hat{t}}+\sigma_{\hat{r}}\mathbf{q}_1+\cos\hat{\theta}\frac{\partial(\mathbf{F}_1-\bar{\mathbf{F}}_1)}{\partial\hat{r}}+\beta_x\cos^2\hat{\theta}\left[\frac{\partial(\mathbf{F}_1-\bar{\mathbf{F}}_1)}{\partial\hat{t}}+\sigma_{\hat{r}}(\mathbf{F}_1-\bar{\mathbf{F}}_1)\right]$$

$$+\sin\hat{\theta}\frac{\partial(\mathbf{F}_2-\bar{\mathbf{F}}_2)}{\partial\hat{r}}+\beta_x\sin\hat{\theta}\cos\hat{\theta}\left[\frac{\partial(\mathbf{F}_2-\bar{\mathbf{F}}_2)}{\partial\hat{t}}+\sigma_{\hat{r}}(\mathbf{F}_2-\bar{\mathbf{F}}_2)\right]=0 \tag{124}$$

$$\frac{\partial\mathbf{q}_2}{\partial\hat{t}}+\frac{1}{\hat{r}}\left(\int_{\hat{r}_0}^{\hat{r}}\sigma_{\hat{r}}\,d\hat{r}\right)\mathbf{q}_2-\frac{\sin\hat{\theta}}{\hat{r}}\frac{\partial(\mathbf{F}_1-\bar{\mathbf{F}}_1)}{\partial\hat{\theta}}$$

$$+\beta_x sin^2\hat{\theta}\left[\frac{\partial(\mathbf{F}_1-\bar{\mathbf{F}}_1)}{\partial\hat{t}}+\frac{1}{\hat{r}}\left(\int_{\hat{r}_0}^{\hat{r}}\sigma_{\hat{r}}\,d\hat{r}\right)(\mathbf{F}_1-\bar{\mathbf{F}}_1)\right]+\frac{\cos\hat{\theta}}{\hat{r}}\frac{\partial(\mathbf{F}_2-\bar{\mathbf{F}}_2)}{\partial\hat{\theta}}$$

$$-\beta_x\cos\hat{\theta}\sin\theta\left[\frac{\partial(\mathbf{F}_2-\bar{\mathbf{F}}_2)}{\partial\hat{t}}+\frac{1}{\hat{r}}\left(\int_{\hat{r}_0}^{\hat{r}}\sigma_{\hat{r}}\,d\hat{r}\right)(\mathbf{F}_2-\bar{\mathbf{F}}_2)\right]=0 \tag{125}$$

All that remains is to rewrite our equations in the original space and time coordinates, $r=\hat{r}$, $\theta=\hat{\theta}$ and $t=\hat{t}-\beta_x\hat{r}\cos\hat{\theta}$. Upon doing so, we arrive at the final equations for $\mathbf{q}_1$ and $\mathbf{q}_2$:

$$\frac{\partial\mathbf{q}_1}{\partial t}+\sigma_r\mathbf{q}_1+\cos\theta\frac{\partial(\mathbf{F}_1-\bar{\mathbf{F}}_1)}{\partial r}+\beta_x\sigma_r\cos^2\theta(\mathbf{F}_1-\bar{\mathbf{F}}_1)+\sin\theta\frac{\partial(\mathbf{F}_2-\bar{\mathbf{F}}_2)}{\partial r}$$

$$+\beta_x\sigma_r\sin\theta\cos\theta(\mathbf{F}_2-\bar{\mathbf{F}}_2)=0 \tag{126}$$

$$\frac{\partial\mathbf{q}_2}{\partial t}+\frac{1}{r}\left(\int_{r_0}^{r}\sigma_r\,dr\right)\mathbf{q}_2-\frac{\sin\theta}{r}\frac{\partial(\mathbf{F}_1-\bar{\mathbf{F}}_1)}{\partial\theta}+\beta_x\frac{\sin^2\theta}{r}\left(\int_{r_0}^{r}\sigma_r\,dr\right)(\mathbf{F}_1-\bar{\mathbf{F}}_1)$$

$$+\frac{\cos\theta}{r}\frac{\partial(\mathbf{F}_2-\bar{\mathbf{F}}_2)}{\partial\theta}-\beta_x\frac{\cos\theta\sin\theta}{r}\left(\int_{r_0}^{r}\sigma_r\,dr\right)(\mathbf{F}_2-\bar{\mathbf{F}}_2)=0 \tag{127}$$

Finally, the equation for $\mathbf{u}'$ can be recovered by adding equations (126) and (127):

$$\frac{\partial\mathbf{u}'}{\partial t}+\sigma_r\mathbf{q}_1+\frac{1}{r}\left(\int_{r_0}^{r}\sigma_r\,dr\right)\mathbf{q}_2+\cos\theta\frac{\partial(\mathbf{F}_1-\bar{\mathbf{F}}_1)}{\partial r}-\frac{\sin\theta}{r}\frac{\partial(\mathbf{F}_1-\bar{\mathbf{F}}_1)}{\partial\theta}+\beta_x\sigma_r\cos^2\theta(\mathbf{F}_1-\bar{\mathbf{F}}_1)$$

$$+\beta_x \frac{\sin^2\theta}{r}\left(\int_{r_0}^{r}\sigma_r\,dr\right)(\mathbf{F}_1-\bar{\mathbf{F}}_1)+\sin\theta\frac{\partial(\mathbf{F}_2-\bar{\mathbf{F}}_2)}{\partial r}+\frac{\cos\theta}{r}\frac{\partial(\mathbf{F}_2-\bar{\mathbf{F}}_2)}{\partial\theta}$$

$$+\beta_x\sigma_r\sin\theta\cos\theta(\mathbf{F}_2-\bar{\mathbf{F}}_2)-\beta_x\frac{\cos\theta\sin\theta}{r}\left(\int_{r_0}^{r}\sigma_r\,dr\right)(\mathbf{F}_2-\bar{\mathbf{F}}_2)=0 \tag{128}$$

The equations valid in the PML region are therefore given by

$$\frac{\partial\mathbf{u}}{\partial t}+\sigma_r\mathbf{q}_1+\frac{1}{r}\left(\int_{r_0}^{r}\sigma_r\,dr\right)\mathbf{q}_2+\cos\theta\frac{\partial(\mathbf{F}_1-\bar{\mathbf{F}}_1)}{\partial r}-\frac{\sin\theta}{r}\frac{\partial(\mathbf{F}_1-\bar{\mathbf{F}}_1)}{\partial\theta}+\beta_x\sigma_r\cos^2\theta(\mathbf{F}_1-\bar{\mathbf{F}}_1)$$

$$+\beta_x \frac{\sin^2\theta}{r}\left(\int_{r_0}^{r}\sigma_r\,dr\right)(\mathbf{F}_1-\bar{\mathbf{F}}_1)+\sin\theta\frac{\partial(\mathbf{F}_2-\bar{\mathbf{F}}_2)}{\partial r}+\frac{\cos\theta}{r}\frac{\partial(\mathbf{F}_2-\bar{\mathbf{F}}_2)}{\partial\theta}$$

$$+\beta_x\sigma_r\sin\theta\cos\theta(\mathbf{F}_2-\bar{\mathbf{F}}_2)-\beta_x\frac{\cos\theta\sin\theta}{r}\left(\int_{r_0}^{r}\sigma_r\,dr\right)(\mathbf{F}_2-\bar{\mathbf{F}}_2)=0 \tag{129}$$

$$\frac{\partial\mathbf{q}_1}{\partial t}+\sigma_r\mathbf{q}_1+\cos\theta\frac{\partial(\mathbf{F}_1-\bar{\mathbf{F}}_1)}{\partial r}+\beta_x\sigma_r\cos^2\theta(\mathbf{F}_1-\bar{\mathbf{F}}_1)+\sin\theta\frac{\partial(\mathbf{F}_2-\bar{\mathbf{F}}_2)}{\partial r}$$

$$+\beta_x\sigma_r\sin\theta\cos\theta(\mathbf{F}_2-\bar{\mathbf{F}}_2)=0 \tag{130}$$

$$\frac{\partial\mathbf{q}_2}{\partial t}+\frac{1}{r}\left(\int_{r_0}^{r}\sigma_r\,dr\right)\mathbf{q}_2-\frac{\sin\theta}{r}\frac{\partial(\mathbf{F}_1-\bar{\mathbf{F}}_1)}{\partial\theta}+\beta_x\frac{\sin^2\theta}{r}\left(\int_{r_0}^{r}\sigma_r\,dr\right)(\mathbf{F}_1-\bar{\mathbf{F}}_1)$$

$$+\frac{\cos\theta}{r}\frac{\partial(\mathbf{F}_2-\bar{\mathbf{F}}_2)}{\partial\theta}-\beta_x\frac{\cos\theta\sin\theta}{r}\left(\int_{r_0}^{r}\sigma_r\,dr\right)(\mathbf{F}_2-\bar{\mathbf{F}}_2)=0 \tag{131}$$

Notice, however, because of the relationship (119) between $\mathbf{u}'$, $\mathbf{q}_1$, and $\mathbf{q}_2$, the equations (129)–(131) are not independent. Therefore, it is only necessary to store two of the three variables, since the third variable can easily be calculated once the values of the other two are known. For example, the second auxiliary variable $\mathbf{q}_2$ and its corresponding equation (131) could be eliminated by substituting

$$\mathbf{q}_2=\mathbf{u}'-\mathbf{q}_1=\mathbf{u}-\bar{\mathbf{u}}-\mathbf{q}_1 \tag{132}$$

into the equation for $\mathbf{u}$ (129). The resulting PML formulation would then be

$$\frac{\partial \mathbf{u}}{\partial t} + \sigma_r \mathbf{q} + \frac{1}{r}\left(\int_{r_0}^{r} \sigma_r \, dr\right)(\mathbf{u} - \bar{\mathbf{u}} - \mathbf{q}) + \cos\theta \frac{\partial(\mathbf{F}_1 - \bar{\mathbf{F}}_1)}{\partial r} - \frac{\sin\theta}{r}\frac{\partial(\mathbf{F}_1 - \bar{\mathbf{F}}_1)}{\partial \theta}$$

$$+\beta_x \sigma_r \cos^2\theta(\mathbf{F}_1 - \bar{\mathbf{F}}_1) + \beta_x \frac{\sin^2\theta}{r}\left(\int_{r_0}^{r} \sigma_r \, dr\right)(\mathbf{F}_1 - \bar{\mathbf{F}}_1) + \sin\theta \frac{\partial(\mathbf{F}_2 - \bar{\mathbf{F}}_2)}{\partial r}$$

$$+\frac{\cos\theta}{r}\frac{\partial(\mathbf{F}_2 - \bar{\mathbf{F}}_2)}{\partial \theta} + \beta_x \sigma_r \sin\theta\cos\theta(\mathbf{F}_2 - \bar{\mathbf{F}}_2) - \beta_x \frac{\cos\theta\sin\theta}{r}\left(\int_{r_0}^{r} \sigma_r \, dr\right)(\mathbf{F}_2 - \bar{\mathbf{F}}_2) = 0 \tag{133}$$

$$\frac{\partial \mathbf{q}}{\partial t} + \sigma_r \mathbf{q} + \cos\theta \frac{\partial(\mathbf{F}_1 - \bar{\mathbf{F}}_1)}{\partial r} + \beta_x \sigma_r \cos^2\theta(\mathbf{F}_1 - \bar{\mathbf{F}}_1) + \sin\theta \frac{\partial(\mathbf{F}_2 - \bar{\mathbf{F}}_2)}{\partial r}$$

$$+\beta_x \sigma_r \sin\theta\cos\theta(\mathbf{F}_2 - \bar{\mathbf{F}}_2) = 0 \tag{134}$$

where $\mathbf{q}$ has replaced $\mathbf{q}_1$, and clearly the storage of only two variables is required. This type of simplification is recommended for improved efficiency.

For the purpose of our examples, the integral functions $\int_{r_0}^{r} \sigma_r \, dr$ are found explicitly rather than approximated numerically at runtime.

IV.1.2 NUMERICAL EXAMPLES

Pressure Pulse with No Mean Flow

We first test our boundary condition for a nonlinear pressure pulse with no mean flow. The domain in consideration is $r \in [0, 5]$, $\theta \in [0, 2\pi)$ with a circular cylinder of radius 0.5 located at the center of the domain. To keep the grid spacing sufficiently small for larger values of r, an overset grid approach is again employed, as is shown in Figure 26. This time, there will be three concentric cylindrical grids. With each transition from an inner grid to an outer grid, the length interval in the θ direction is halved. So the length intervals are $\Delta r = 0.03$, and $\Delta\theta = \frac{\pi}{50}$, $\frac{\pi}{100}$, and $\frac{\pi}{200}$ for each of the respective grids. The seven-point DRP scheme is again used for spatial discretizations with a periodic boundary closure scheme for θ derivatives and a separate third-order boundary closure scheme for r derivatives. The five-stage LDDRK scheme is used for advancing time with $\Delta t = \frac{0.5}{1+\sqrt{2}}\Delta r$ chosen for stability. The absorption coefficient will be taken as

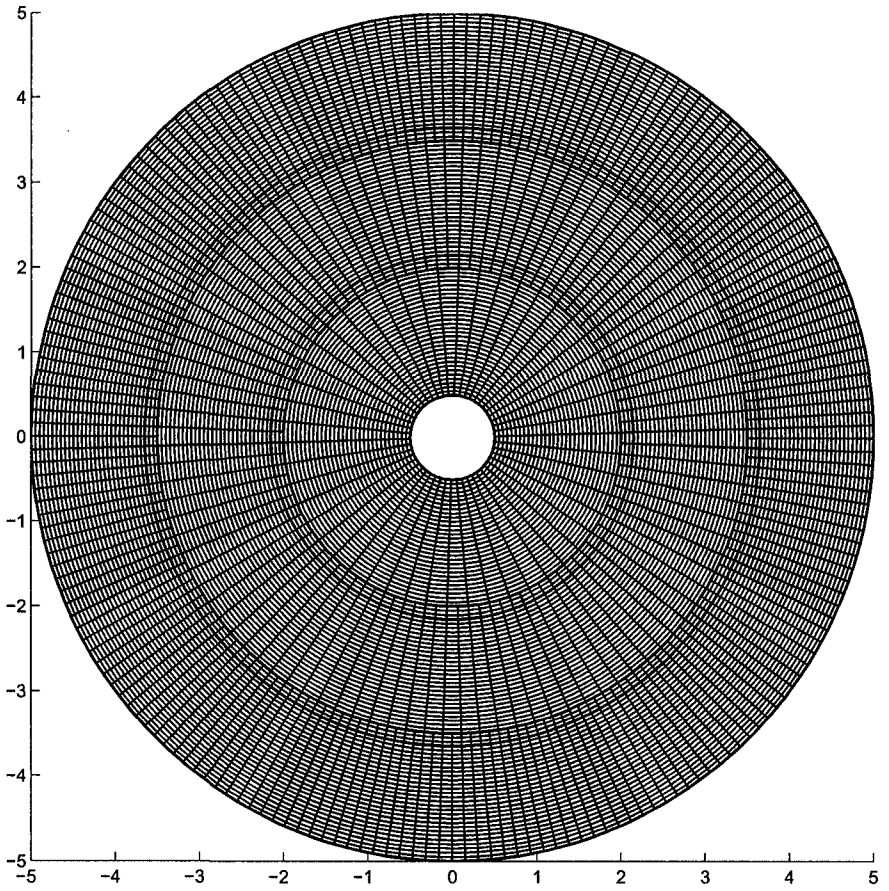

FIG. 26: Overset grids include three concentric cylindrical grids.

$$\sigma_r = \sigma_{\max} \left| \frac{r - r_0}{D} \right|^{\alpha} \tag{135}$$

where r_0 is the location of the interface between Euler and PML regions. Parameter values are chosen as $\sigma_{\max} = 20$ and $\alpha = 4$, and a PML width $D = 20\Delta r$ is chosen. The pressure pulse will start at the point (3,0) and is initialized as

$$\rho = 1 \tag{136}$$

$$u = 0 \tag{137}$$

$$v = 0 \tag{138}$$

$$p = \frac{1}{\gamma} + e^{-\ln(2)((x-3)^2+y^2)/0.2^2} \tag{139}$$

with $\gamma = 1.4$. Figure 27 shows the contours of pressure at times $t = 0, 2, 5$, and 7.5. The wave appears to exit the domain with little reflection. To better assess the

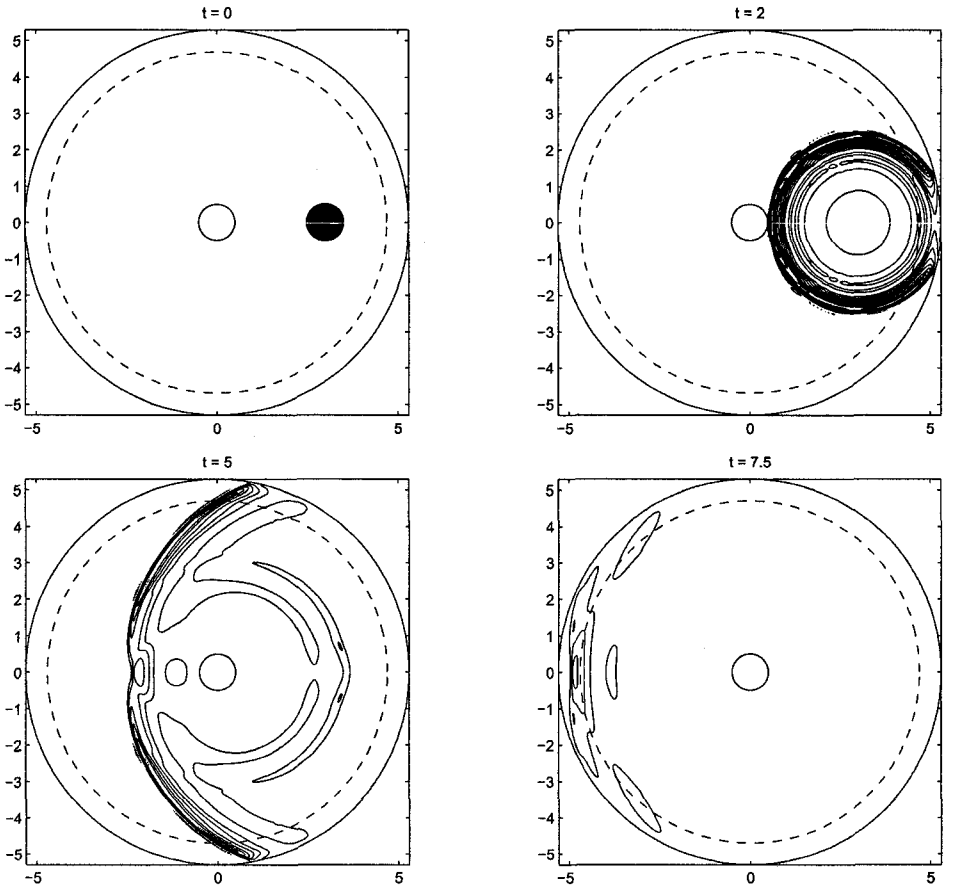

FIG. 27: Pressure pulse with no mean flow: Pressure contours at times $t = 0, 2, 5$, and 7.5.

reflection error, the PML solution is compared with a reference solution, which is found by calculating solutions on the larger domain $r \in [0, 16]$, $\theta \in [0, 2\pi)$. The time history of pressure at a single point is plotted for both solutions in the top part of Figure 28. On the bottom, the difference between the two solutions is plotted as a function of time. Good agreement is seen between the two solutions, with maximum difference magnitude around 10^{-4}.

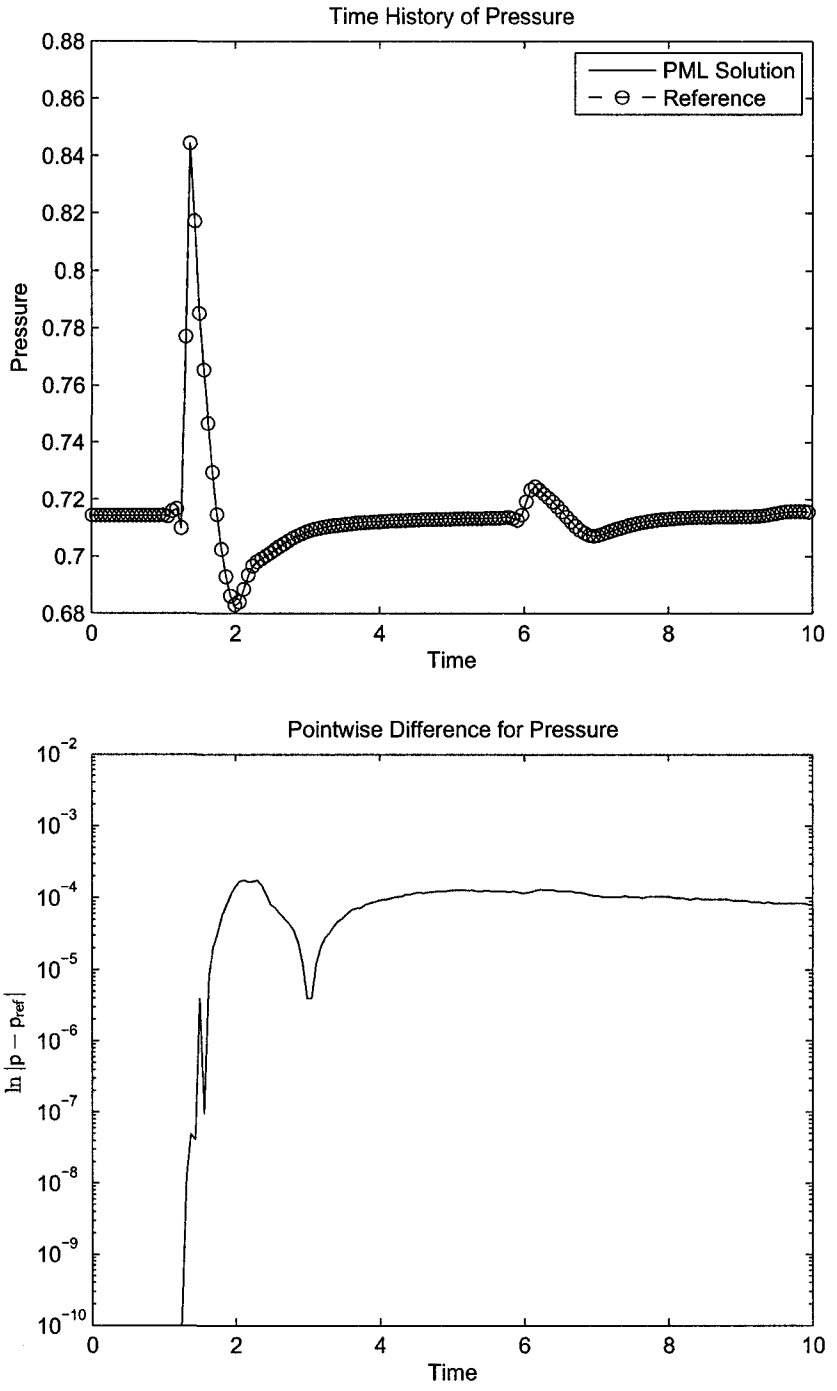

FIG. 28: Top: Time history of pressure at a single point for the PML and reference solutions. Bottom: Difference between the two solutions at the same point as a function of time.

Pressure Pulse with Mean Flow

Our equations will also be tested for a pressure pulse in the presence of mean flow. Flow is assumed in the horizontal direction only, which is seen in the initial condition as a nonzero x-component of velocity. The domain will again be $r \in [0, 5]$, $\theta \in [0, 2\pi)$. We again use overset grids, but this time a Cartesian grid, $x \in [-1, 1]$, $y \in [-1, 1]$, is added to the center of the domain to accommodate solutions at the origin, as is seen in Figure 29. Discretizations in time and space are identical to the previous

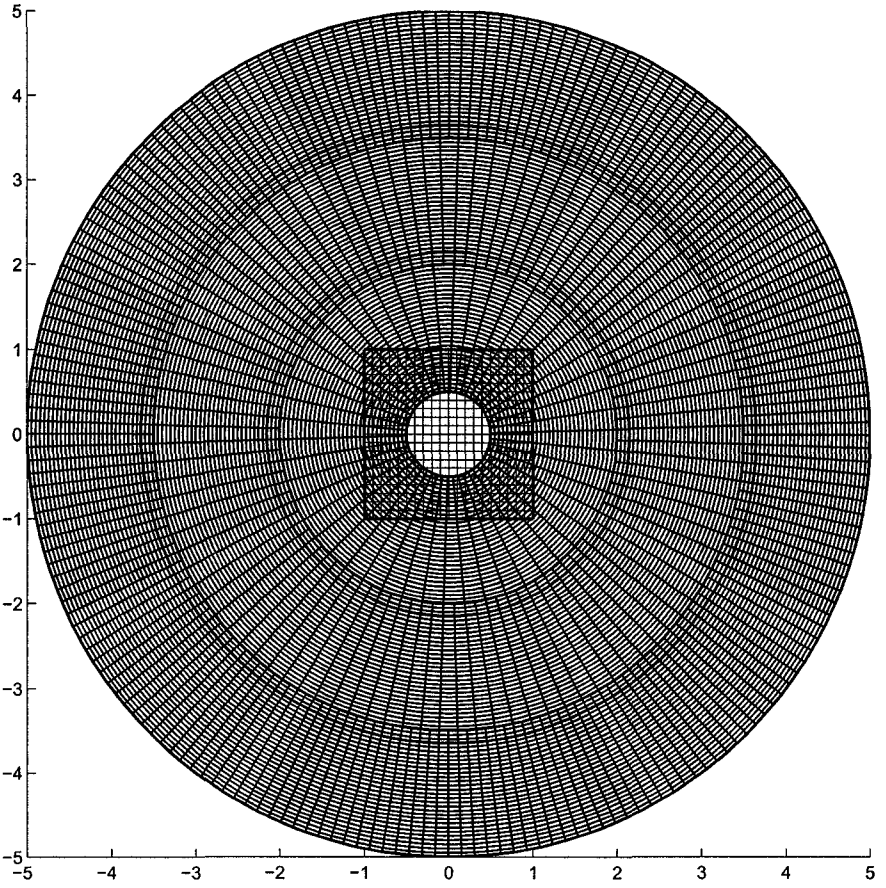

FIG. 29: Overset grids include three concentric cylindrical grids with a Cartesian grid in the center.

example, and we now take $\Delta x = \Delta y = 0.04$. In this example, the pressure pulse will be initialized at the center of the domain as

$$\rho = 1 + e^{-\ln(2)(x^2+y^2)/0.2^2} \tag{140}$$

$$u = 0.5 \tag{141}$$

$$v = 0 \tag{142}$$

$$p = \frac{1}{\gamma} + e^{-\ln(2)(x^2+y^2)/0.2^2} \tag{143}$$

with $\gamma = 1.4$. Figure 30 shows the contours of pressure at times $t = 0, 2, 5$, and 8 for a PML width of $D = 20\Delta r$. Again, the waves appear to exit with little reflection.

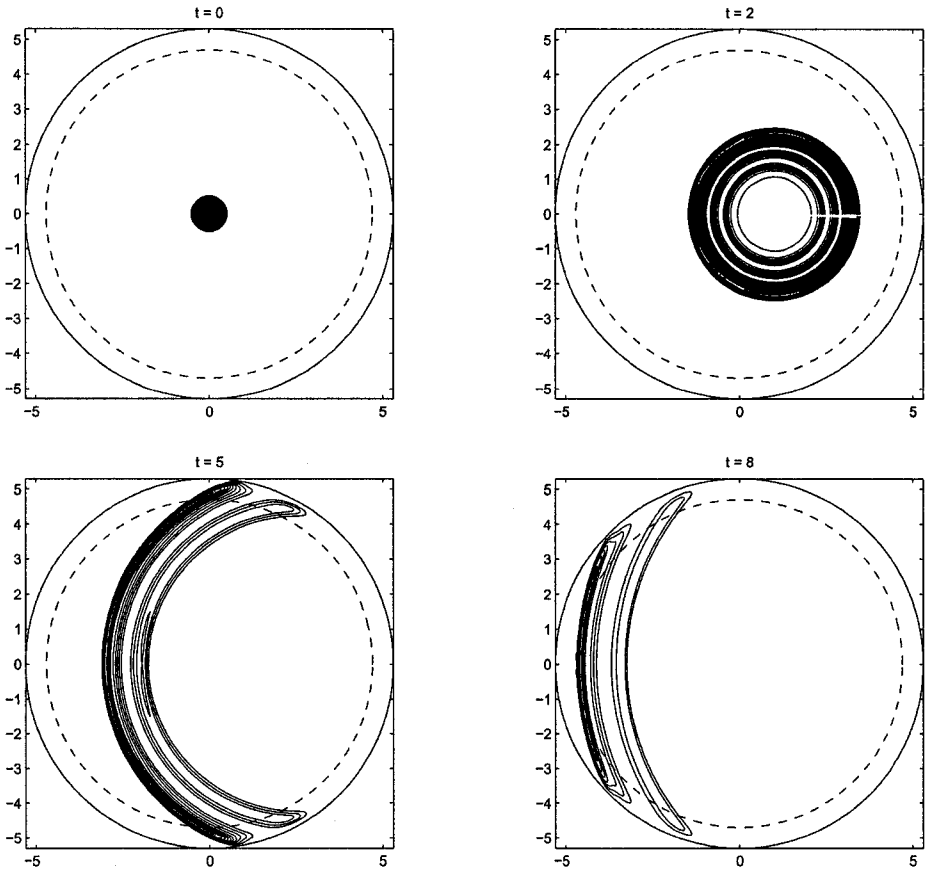

FIG. 30: Pressure pulse with mean flow: Pressure contours at times $t = 0, 2, 5$, and 8.

Comparison with a larger domain reference solution, shown in Figure 31, validates the effectiveness of the boundary condition, with good agreement seen between the two solutions in the time history of pressure at the point $(4.55, 0)$ and the difference between the two solutions on the order of magnitude 10^{-6}.

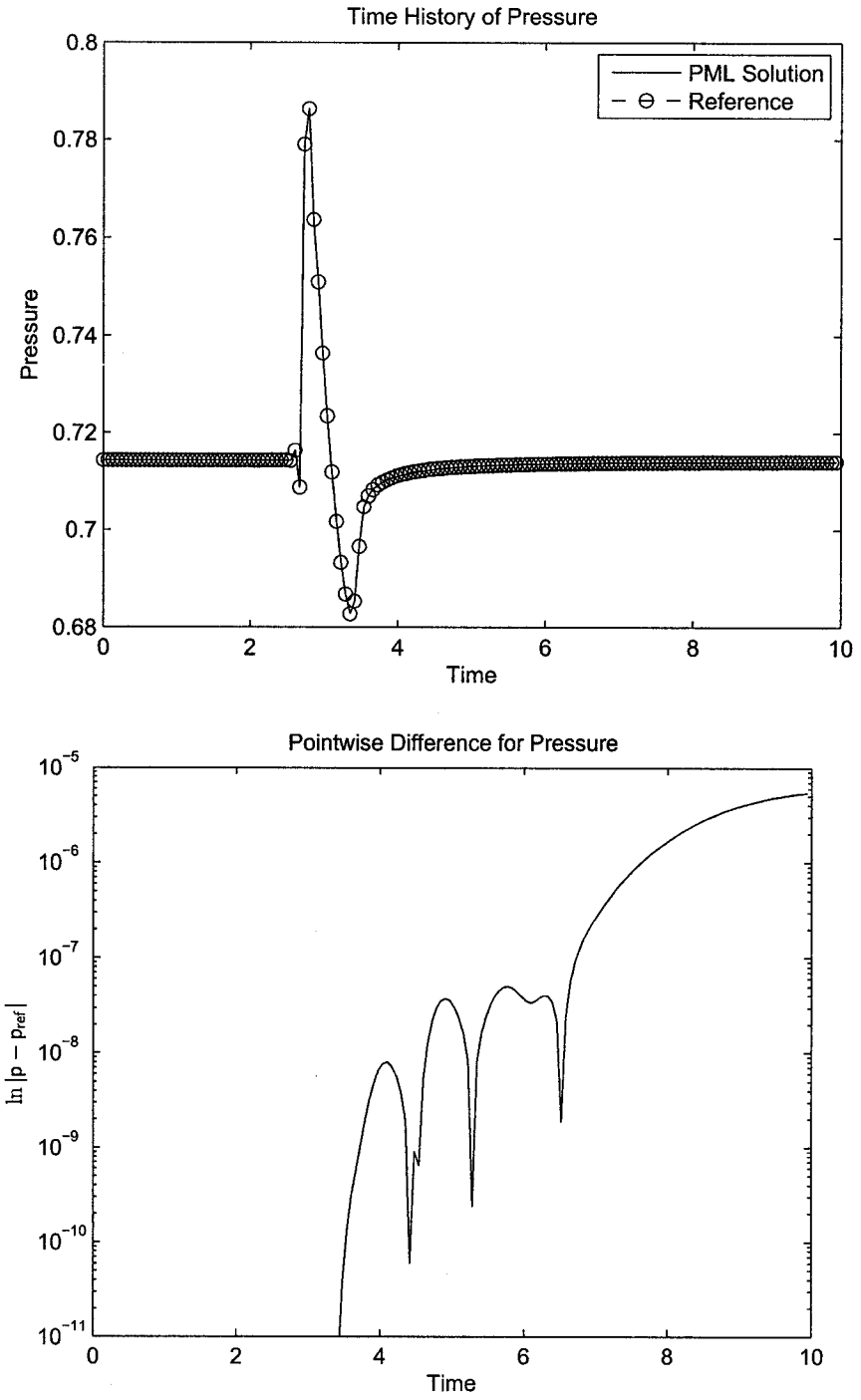

FIG. 31: Top: Time history of pressure at a single point for the PML and reference solutions. Bottom: Difference between the two solutions at the same point as a function of time.

IV.2 LINEARIZED EULER EQUATIONS IN PRIMITIVE VARIABLES

IV.2.1 DERIVATION OF PML EQUATIONS

To accommodate various interior schemes in CFD and CAA, we will also derive the cylindrical PML boundary condition for primitive variables. Primitive variables are most often used with the linearized form of the Euler equations, so the linearized form in cylindrical coordinates will be considered. The derivation of such equations was carried out by applying the transformations

$$\frac{\partial}{\partial x} = \cos\theta \frac{\partial}{\partial r} - \frac{\sin\theta}{r}\frac{\partial}{\partial \theta} \tag{144}$$

$$\frac{\partial}{\partial y} = \sin\theta \frac{\partial}{\partial r} + \frac{\cos\theta}{r}\frac{\partial}{\partial \theta} \tag{145}$$

$$u = v_r \cos\theta - v_\theta \sin\theta \tag{146}$$

$$v = v_r \sin\theta + v_\theta \cos\theta \tag{147}$$

to the linearized Euler equations in Cartesian coordinates (18) under the assumption that the mean flow (U_0, V_0) is constant. The resulting linearized equations are given by

$$\frac{\partial \rho}{\partial t} + \bar{v}_r \frac{\partial \rho}{\partial r} + \frac{\bar{v}_\theta}{r}\frac{\partial \rho}{\partial \theta} + \frac{\partial v_r}{\partial r} + \frac{1}{r}\frac{\partial v_\theta}{\partial \theta} + \frac{v_r}{r} = 0 \tag{148}$$

$$\frac{\partial v_r}{\partial t} + \bar{v}_r \frac{\partial v_r}{\partial r} + \frac{\bar{v}_\theta}{r}\frac{\partial v_r}{\partial \theta} + \frac{\partial p}{\partial r} - \frac{\bar{v}_\theta v_\theta}{r} = 0 \tag{149}$$

$$\frac{\partial v_\theta}{\partial t} + \bar{v}_r \frac{\partial v_\theta}{\partial r} + \frac{\bar{v}_\theta}{r}\frac{\partial v_\theta}{\partial \theta} + \frac{1}{r}\frac{\partial p}{\partial \theta} + \frac{\bar{v}_\theta v_r}{r} = 0 \tag{150}$$

$$\frac{\partial p}{\partial t} + \bar{v}_r \frac{\partial p}{\partial r} + \frac{\bar{v}_\theta}{r}\frac{\partial p}{\partial \theta} + \frac{\partial v_r}{\partial r} + \frac{1}{r}\frac{\partial v_\theta}{\partial \theta} + \frac{v_r}{r} = 0 \tag{151}$$

where ρ is the density, v_r and v_θ are the velocities in the r- and θ-directions, respectively, and p is the pressure. These can be written in matrix-vector form as

$$\frac{\partial \mathbf{u}}{\partial t} + \mathsf{A}(\theta)\frac{\partial \mathbf{u}}{\partial r} + \frac{1}{r}\mathsf{B}(\theta)\frac{\partial \mathbf{u}}{\partial \theta} + \frac{1}{r}\mathsf{C}(\theta)\mathbf{u} = 0 \tag{152}$$

where

$$\mathbf{u} = \begin{pmatrix} \rho \\ v_r \\ v_\theta \\ p \end{pmatrix}, \; \mathsf{A}(\theta) = \begin{pmatrix} \bar{v}_r & 1 & 0 & 0 \\ 0 & \bar{v}_r & 0 & 1 \\ 0 & 0 & \bar{v}_r & 0 \\ 0 & 1 & 0 & \bar{v}_r \end{pmatrix}, \; \mathsf{B}(\theta) = \begin{pmatrix} \bar{v}_\theta & 0 & 1 & 0 \\ 0 & \bar{v}_\theta & 0 & 0 \\ 0 & 0 & \bar{v}_\theta & 1 \\ 0 & 0 & 1 & \bar{v}_\theta \end{pmatrix},$$

$$\mathsf{C}(\theta) = \begin{pmatrix} 0 & 1 & 0 & 0 \\ 0 & 0 & -\bar{v}_\theta & 0 \\ 0 & \bar{v}_\theta & 0 & 0 \\ 0 & 1 & 0 & 0 \end{pmatrix} \tag{153}$$

We note that ρ, v_r, v_θ, and p in (152) are the perturbations to the mean flow, and that matrices A, B, and C depend on θ because the cylindrical mean velocities $\bar{v}_r$ and $\bar{v}_\theta$ are related to the Cartesian mean velocities U_0 and V_0 by

$$\bar{v}_r = U_0 \cos\theta + V_0 \sin\theta \tag{154}$$

$$\bar{v}_\theta = -U_0 \sin\theta + V_0 \cos\theta \tag{155}$$

In this section, however, PML equations are only considered for a one-dimensional mean flow $(U_0, 0)$. The case of a general mean flow (U_0, V_0) is addressed in the following section.

To ensure consistency in phase and group velocities, we begin with a single space-time transformation, namely

$$\hat{t} = t + \beta_x r \cos\theta \tag{156}$$

$$\hat{r} = r \tag{157}$$

$$\hat{\theta} = \theta \tag{158}$$

which gives

$$\frac{\partial}{\partial t} = \frac{\partial}{\partial \hat{t}} \tag{159}$$

$$\frac{\partial}{\partial r} = \frac{\partial}{\partial \hat{r}} + \beta_x \cos\hat{\theta} \frac{\partial}{\partial \hat{t}} \tag{160}$$

$$\frac{\partial}{\partial \theta} = \frac{\partial}{\partial \hat{\theta}} - \beta_x \hat{r} \sin\hat{\theta} \frac{\partial}{\partial \hat{t}} \tag{161}$$

where

$$\beta_x = \frac{U_0}{1 - U_0^2} \tag{162}$$

Such a transformation is sufficient for removing the inconsistencies in phase and group velocities of the acoustic waves since we are dealing with one-dimensional mean flow. The equation then becomes

$$\frac{\partial \mathbf{u}}{\partial \hat{t}} + \mathsf{A}\left[\frac{\partial \mathbf{u}}{\partial \hat{r}} + \beta_x \cos\hat{\theta}\frac{\partial \mathbf{u}}{\partial \hat{t}}\right] + \frac{1}{\hat{r}}\mathsf{B}\left[\frac{\partial \mathbf{u}}{\partial \hat{\theta}} - \beta_x \hat{r}\sin\hat{\theta}\frac{\partial \mathbf{u}}{\partial \hat{t}}\right] + \frac{1}{\hat{r}}\mathsf{C}\mathbf{u} = 0 \tag{163}$$

For simplicity, matrices $\mathsf{A}(\theta)$, $\mathsf{B}(\theta)$, and $\mathsf{C}(\theta)$ are abbreviated as A, B, and C, respectively. At this point, it is valid to apply the PML change of variable in the frequency domain without risk of instability. Writing the equation in the frequency domain, we have

$$(-i\omega)\tilde{\mathbf{u}} + \mathsf{A}\left[\frac{\partial \tilde{\mathbf{u}}}{\partial \hat{r}} + \beta_x \cos\hat{\theta}(-i\omega)\tilde{\mathbf{u}}\right] + \frac{1}{\hat{r}}\mathsf{B}\left[\frac{\partial \tilde{\mathbf{u}}}{\partial \hat{\theta}} - \beta_x \hat{r}\sin\hat{\theta}(-i\omega)\tilde{\mathbf{u}}\right] + \frac{1}{\hat{r}}\mathsf{C}\tilde{\mathbf{u}} = 0 \tag{164}$$

We can now apply the PML change of variable, given by

$$\hat{r} \rightarrow \hat{r} + \frac{i}{\omega}\int_{\hat{r}_0}^{\hat{r}} \sigma_{\hat{r}}\, d\hat{r} \tag{165}$$

and our equation becomes

$$(-i\omega)\tilde{\mathbf{u}} + \mathsf{A}\left[\frac{1}{1 + i\frac{\sigma_{\hat{r}}}{\omega}}\frac{\partial \tilde{\mathbf{u}}}{\partial \hat{r}} + \beta_x \cos\hat{\theta}(-i\omega)\tilde{\mathbf{u}}\right] +$$

$$\frac{1}{\hat{r} + \frac{i}{\omega}\int_{\hat{r}_0}^{\hat{r}} \sigma_{\hat{r}}\, d\hat{r}}\mathsf{B}\left[\frac{\partial \tilde{\mathbf{u}}}{\partial \hat{\theta}} - \beta_x\left(\hat{r} + \frac{i}{\omega}\int_{\hat{r}_0}^{\hat{r}} \sigma_{\hat{r}}\, d\hat{r}\right)\sin\hat{\theta}(-i\omega)\tilde{\mathbf{u}}\right] + \frac{1}{\hat{r} + \frac{i}{\omega}\int_{\hat{r}_0}^{\hat{r}} \sigma_{\hat{r}}\, d\hat{r}}\mathsf{C}\tilde{\mathbf{u}} = 0 \tag{166}$$

All that remains is to convert back to the time domain and finally back to the original coordinate system. To facilitate conversion back to the time domain, we split $\mathbf{u}$ into two auxiliary variables:

$$\mathbf{u} = \mathbf{q}_1 + \mathbf{q}_2 \tag{167}$$

Our single equation for $\mathbf{u}$ can then be split into two equations, one for each of the auxiliary variables $\mathbf{q}_1$ and $\mathbf{q}_2$, and as before, complex fractions can be easily cleared, resulting in

$$(-i\omega + \sigma_{\hat{r}})\tilde{\mathbf{q}}_1 + \mathsf{A}\left[\frac{\partial \tilde{\mathbf{u}}}{\partial \hat{r}} + \beta_x \cos\hat{\theta}(-i\omega)\tilde{\mathbf{u}} + \beta_x \sigma_{\hat{r}} \cos\hat{\theta}\tilde{\mathbf{u}}\right] = 0 \tag{168}$$

$$(-i\omega)\tilde{\mathbf{q}}_2 + \frac{1}{\hat{r}}\left(\int_{\hat{r}_0}^{\hat{r}} \sigma_{\hat{r}}\, d\hat{r}\right)\tilde{\mathbf{q}}_2 + \frac{1}{\hat{r}}\mathsf{B}\left[\frac{\partial \tilde{\mathbf{u}}}{\partial \hat{\theta}} - \beta_x \hat{r}\sin\hat{\theta}(-i\omega)\tilde{\mathbf{u}} - \beta_x\left(\int_{\hat{r}_0}^{\hat{r}} \sigma_{\hat{r}}\, d\hat{r}\right)\sin\hat{\theta}\tilde{\mathbf{u}}\right]$$

$$+\frac{1}{\hat{r}}\mathsf{C}\tilde{\mathbf{u}} = 0 \tag{169}$$

The simple transition back to the time domain then results in

$$\frac{\partial \mathbf{q}_1}{\partial \hat{t}} + \sigma_{\hat{r}}\mathbf{q}_1 + \mathsf{A}\left[\frac{\partial \mathbf{u}}{\partial \hat{r}} + \beta_x \cos\hat{\theta}\frac{\partial \mathbf{u}}{\partial \hat{t}} + \beta_x \sigma_{\hat{r}} \cos\hat{\theta}\mathbf{u}\right] = 0 \tag{170}$$

$$\frac{\partial \mathbf{q}_2}{\partial \hat{t}} + \frac{1}{\hat{r}}\left(\int_{\hat{r}_0}^{\hat{r}} \sigma_{\hat{r}}\, d\hat{r}\right)\mathbf{q}_2 + \frac{1}{\hat{r}}\mathsf{B}\left[\frac{\partial \mathbf{u}}{\partial \hat{\theta}} - \beta_x \hat{r}\sin\hat{\theta}\frac{\partial \mathbf{u}}{\partial \hat{t}} - \beta_x\left(\int_{\hat{r}_0}^{\hat{r}} \sigma_{\hat{r}}\, d\hat{r}\right)\sin\hat{\theta}\mathbf{u}\right] + \frac{1}{\hat{r}}\mathsf{C}\mathbf{u} = 0 \tag{171}$$

Finally, in the original coordinates, t, r, and θ, we arrive at the final equations for $\mathbf{q}_1$ and $\mathbf{q}_2$:

$$\frac{\partial \mathbf{q}_1}{\partial t} + \sigma_r \mathbf{q}_1 + \mathsf{A}\left[\frac{\partial \mathbf{u}}{\partial r} + \beta_x \sigma_r \cos\theta\mathbf{u}\right] = 0 \tag{172}$$

$$\frac{\partial \mathbf{q}_2}{\partial t} + \frac{1}{r}\left(\int_{r_0}^{r} \sigma_r\, dr\right)\mathbf{q}_2 + \frac{1}{r}\mathsf{B}\left[\frac{\partial \mathbf{u}}{\partial \theta} - \beta_x\left(\int_{r_0}^{r} \sigma_r\, dr\right)\sin\theta\mathbf{u}\right] + \frac{1}{r}\mathsf{C}\mathbf{u} = 0 \tag{173}$$

The equation for $\mathbf{u}$ is easily recovered by adding equations (172) and (173). The PML equations are therefore given by

$$\frac{\partial \mathbf{u}}{\partial t} + \sigma_r \mathbf{q}_1 + \frac{1}{r}\left(\int_{r_0}^{r} \sigma_r\, dr\right)\mathbf{q}_2 + \mathsf{A}\left[\frac{\partial \mathbf{u}}{\partial r} + \beta_x \sigma_r \cos\theta\mathbf{u}\right] +$$

$$\frac{1}{r}\mathsf{B}\left[\frac{\partial \mathbf{u}}{\partial \theta} - \beta_x\left(\int_{r_0}^{r} \sigma_r\, dr\right)\sin\theta\mathbf{u}\right] + \frac{1}{r}\mathsf{C}\mathbf{u} = 0 \tag{174}$$

$$\frac{\partial \mathbf{q}_1}{\partial t} + \sigma_r \mathbf{q}_1 + \mathsf{A}\left[\frac{\partial \mathbf{u}}{\partial r} + \beta_x \sigma_r \cos\theta\mathbf{u}\right] = 0 \tag{175}$$

$$\frac{\partial \mathbf{q}_2}{\partial t} + \frac{1}{r}\left(\int_{r_0}^{r} \sigma_r\, dr\right)\mathbf{q}_2 + \frac{1}{r}\mathsf{B}\left[\frac{\partial \mathbf{u}}{\partial \theta} - \beta_x\left(\int_{r_0}^{r} \sigma_r\, dr\right)\sin\theta\mathbf{u}\right] + \frac{1}{r}\mathsf{C}\mathbf{u} = 0 \tag{176}$$

Similar to the equations derived in the previous section, equations (174)–(176) are not independent. Eliminating one of the auxiliary variables results in the following equivalent but more efficient system of equations:

$$\frac{\partial \mathbf{u}}{\partial t} + \sigma_r \mathbf{q} + \frac{1}{r}\left(\int_{r_0}^{r} \sigma_r \, dr\right)(\mathbf{u} - \mathbf{q}) + \mathsf{A}\left[\frac{\partial \mathbf{u}}{\partial r} + \beta_x \sigma_r \cos\theta \mathbf{u}\right]$$

$$+\frac{1}{r}\mathsf{B}\left[\frac{\partial \mathbf{u}}{\partial \theta} - \beta_x \left(\int_{r_0}^{r} \sigma_r \, dr\right)\sin\theta \mathbf{u}\right] + \frac{1}{r}\mathsf{C}\mathbf{u} = 0 \tag{177}$$

$$\frac{\partial \mathbf{q}}{\partial t} + \sigma_r \mathbf{q} + \mathsf{A}\left[\frac{\partial \mathbf{u}}{\partial r} + \beta_x \sigma_r \cos\theta \mathbf{u}\right] = 0 \tag{178}$$

Here $\mathbf{q}_2$ has been eliminated, and $\mathbf{q}_1$ has been replaced with $\mathbf{q}$.

Again, for numerical examples, the integral terms $\int_{r_0}^{r} \sigma_r \, dr$ are found explicitly rather than approximated at runtime.

IV.2.2 NUMERICAL EXAMPLES

Acoustic, Vorticity, and Entropy Waves with a Horizontal Mean Flow

We will test the equations developed in the previous section using an example of acoustic, vorticity, and entropy pulses traveling with a horizontal mean flow. The pulses are now initialized for the linearized equations as

$$\rho = e^{-\ln(2)(x^2+y^2)/0.2^2} + \sum_{n=1}^{3} e^{-\ln(2)((x-x_n)^2+(y-y_n)^2)/0.2^2} \tag{179}$$

$$u = \sum_{n=1}^{3} (y+1) e^{-\ln(2)((x-x_n)^2+(y-y_n)^2)/0.2^2} \tag{180}$$

$$v = -\sum_{n=1}^{3} (x-1) e^{-\ln(2)((x-x_n)^2+(y-y_n)^2)/0.2^2} \tag{181}$$

$$p = e^{-\ln(2)(x^2+y^2)/0.2^2} \tag{182}$$

where $(x_1, y_1) = (2, 0)$, $(x_2, y_2) = (1, 1)$, and $(x_3, y_3) = (1, -1)$ are the initial locations of the vorticity and entropy pulses, and $(0, 0)$ is the initial location of the acoustic pulse. The domain is $r \in [0, 5]$, $\theta \in [0, 2\pi)$ with a PML width of $D = 20\Delta x$. Mean flow is taken as $(U_0, V_0) = (0.5, 0)$. Grids and discretizations are setup exactly as they were in the second example of Section IV.1.2. The absorption coefficient, σ_r, takes the form (135) with $\sigma_{\max} = 35$ and $\alpha = 2$. Figure 32 shows the contours of density at

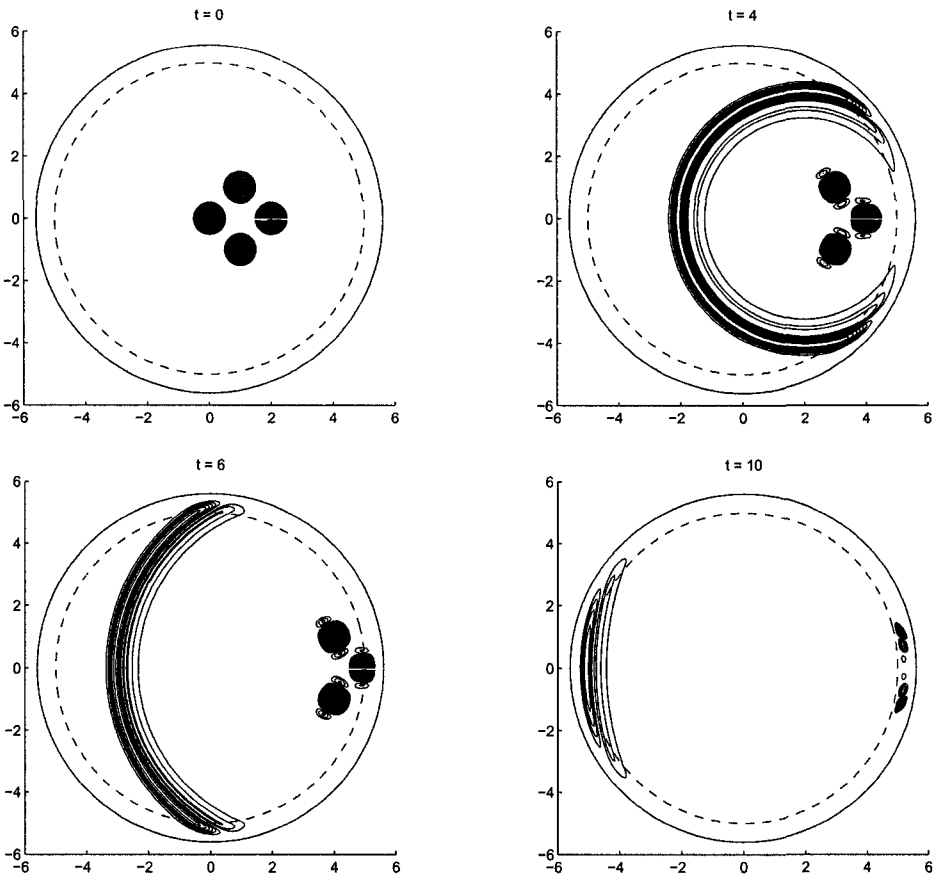

FIG. 32: Acoustic, vorticity, and entropy pulses with horizontal mean flow: Density contours at times $t = 0, 4, 6$, and 10.

times $t = 0$, 4, 6, and 10. The waves appear to exit the domain with little reflection. The PML solution is compared with a reference solution from the larger domain $r \in [0, 11]$, $\theta \in [0, 2\pi)$. The top part of Figure 33 plots the PML solution of density at the single point $(r, \theta) = (4.55, 0)$ against the corresponding reference solution as a function of time. Good agreement is seen in this case. The difference between these two solutions at the same point is plotted in the bottom of Figure 33, and the magnitude of the difference remains small for all given values of time. Figure 34 shows the reflection coefficient for density as calculated by the maximum difference between the PML and reference solutions along the points $r = 4.55, \theta \in [0, 2\pi)$, normalized by the maximum wave amplitude, which in this case is simply unity. The

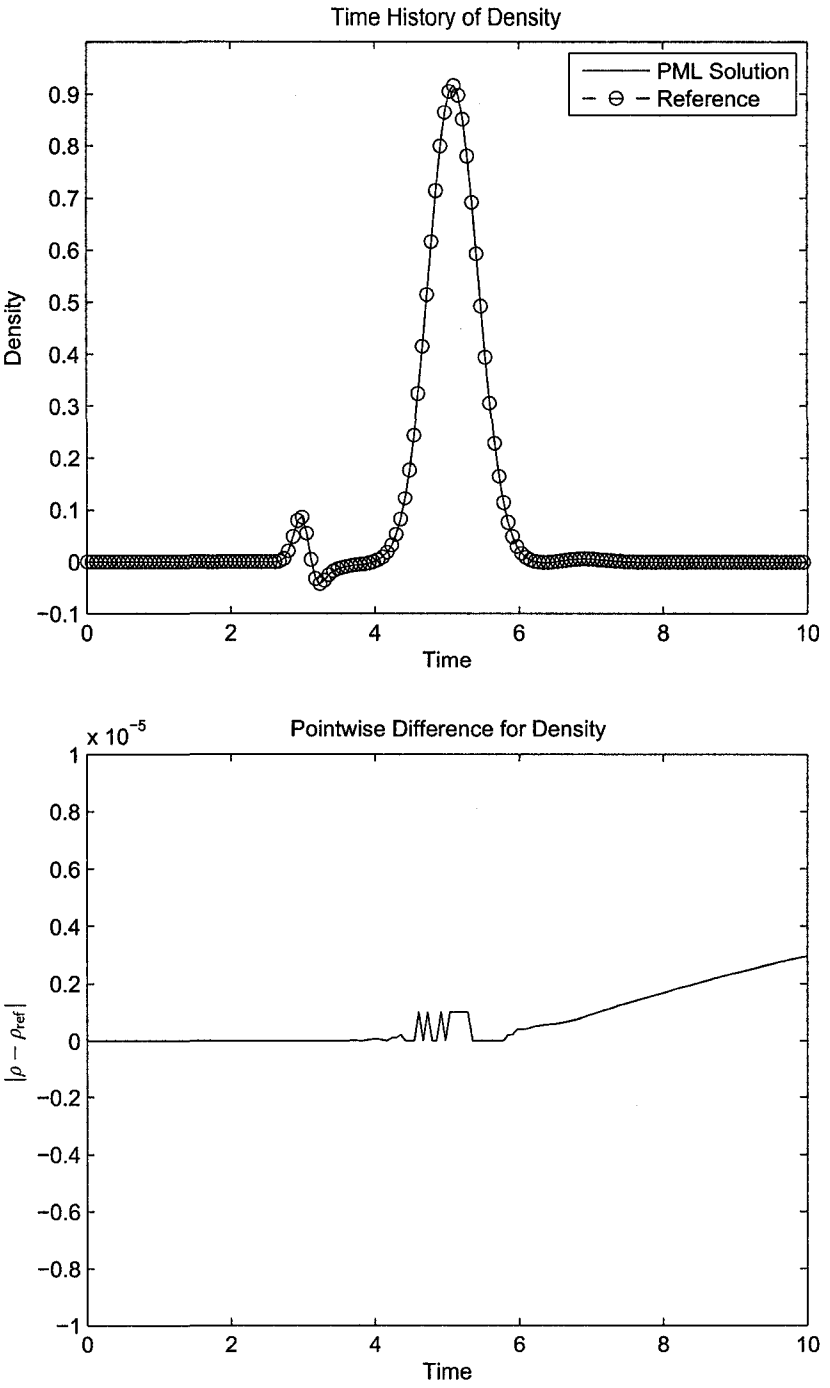

FIG. 33: Top: Time history of density at the point $(r, \theta) = (4.55, 0)$ for the PML and reference solutions. Bottom: Difference between the two solutions at the same point as a function of time.

peak magnitude for the reflection coefficient is close to 10^{-5}.

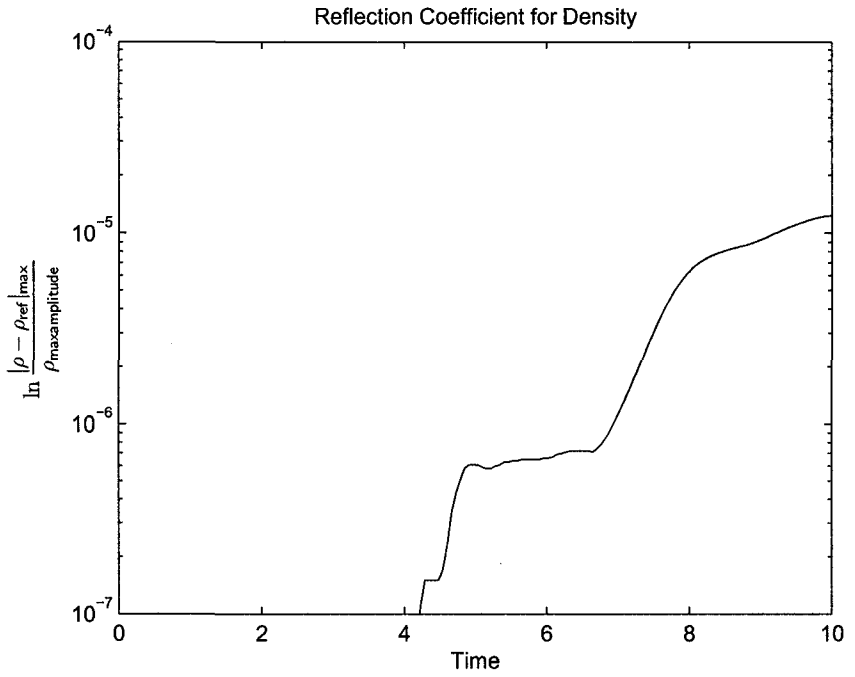

FIG. 34: Reflection coefficient for density as a function of time, computed along the points $r = 4.55$, $\theta \in [0, 2\pi)$.

IV.3 EXTENSION OF CYLINDRICAL PML TO OBLIQUE MEAN FLOW

IV.3.1 GENERAL APPROACH

Because of the radial symmetry in cylindrical coordinates, deriving the PML equations for an oblique mean flow is greatly simplified. As we will see, it involves only one extra step, an initial rotation of the coordinate system. Recall from Section II.2.1 that the space-time transformation used to remove inconsistencies in phase and group velocities is valid only for one-dimensional mean flow, which in our derivation for the cylindrical equations was taken in the x-direction. Therefore, if mean flow is also present in the y-direction, that same transformation will not be effective in removing the inconsistencies. An easy way to work around this is to use a rotated coordinate system in which the horizontal axis is aligned with the direction of mean flow. The

mean flow will then be present in only one dimension of the new coordinate system, and a single transformation can again be used to correct the inconsistencies in phase and group velocities. Suppose we have a system with mean flow given by (U_0, V_0) where U_0 and V_0 are both nonzero. The resultant mean flow has a magnitude of $M = \sqrt{U_0^2 + V_0^2}$ in the direction of angle $\phi = \tan^{-1}\left(\frac{V_0}{U_0}\right)$ from the positive x-axis, as is shown in Figure 35. In such a situation, we will transform to a new coordinate

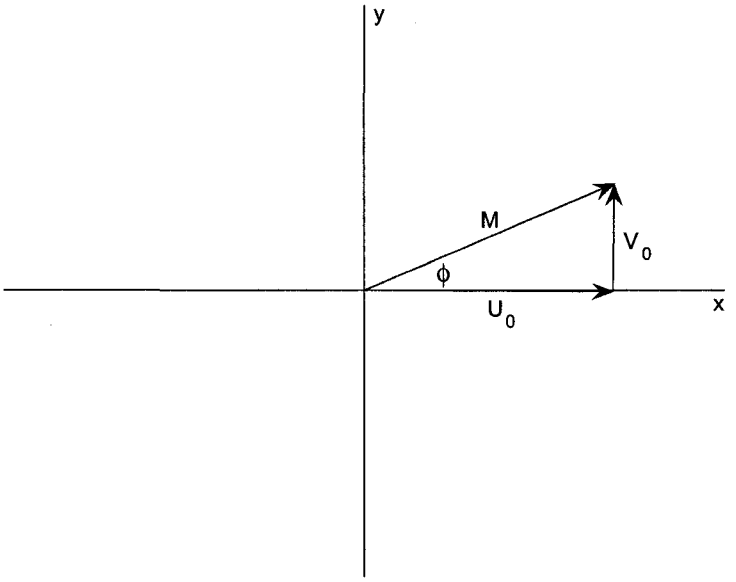

FIG. 35: Mean flow in two dimensions.

system, (x', y'), in which the horizontal axis is aligned with the mean flow, as is shown in Figure 36. The mean flow in (x', y') is then $(M, 0)$, which is clearly nonzero only in the x'-direction. With the mean flow reduced to one dimension, we can proceed as before in the derivation of the PML equations. Once the equations are formed in x' and y', the final step in the derivation will be to translate back to the original coordinates x and y.

It should be mentioned that such an approach is not valid in Cartesian coordinates, as the rotation of the coordinate system would affect the location of the interface between the Euler and PML regions, and the boundaries would no longer be aligned with the coordinate system.

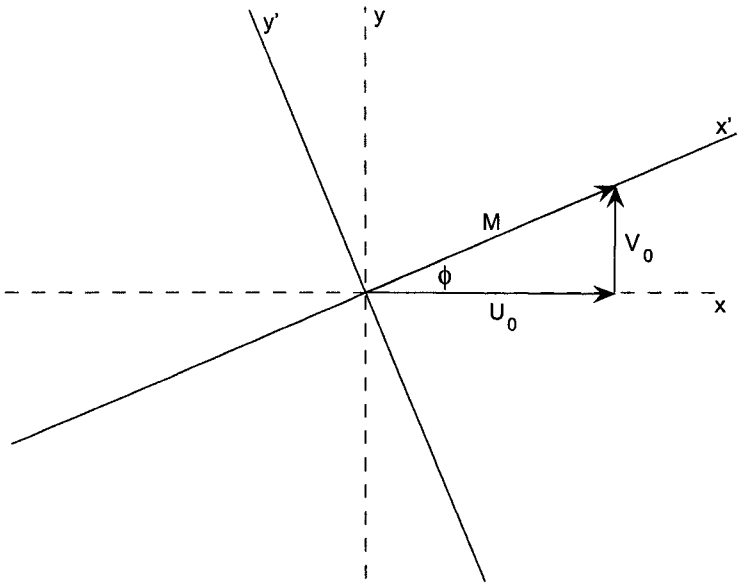

FIG. 36: Rotated coordinate system.

IV.3.2 PML FOR NONLINEAR EULER EQUATIONS IN CONSERVATION FORM

Suppose we want to rederive the cylindrical PML equations for the nonlinear Euler equations (99) with an oblique background flow (U_0, V_0). Using the rotated coordinate system given above, our new cylindrical variables will be

$$r' = r \tag{183}$$

$$\theta' = \theta - \phi \tag{184}$$

where

$$\phi = \tan^{-1}\left(\frac{V_0}{U_0}\right) \tag{185}$$

which means

$$\frac{\partial}{\partial r'} = \frac{\partial}{\partial r} \tag{186}$$

$$\frac{\partial}{\partial \theta'} = \frac{\partial}{\partial \theta} \tag{187}$$

As mentioned above, the mean flow in the rotated coordinate system will be $(M, 0)$, where

$$M = \sqrt{U_0^2 + V_0^2} \tag{188}$$

Then, after the variable has been split according to (102), the governing equations in (r', θ') are simply

$$\frac{\partial \mathbf{u}'}{\partial t} + \cos\theta' \frac{\partial(\mathbf{F}_1 - \bar{\mathbf{F}}_1)}{\partial r'} - \frac{\sin\theta'}{r'} \frac{\partial(\mathbf{F}_1 - \bar{\mathbf{F}}_1)}{\partial \theta'} + \sin\theta' \frac{\partial(\mathbf{F}_2 - \bar{\mathbf{F}}_2)}{\partial r'} + \frac{\cos\theta'}{r'} \frac{\partial(\mathbf{F}_2 - \bar{\mathbf{F}}_2)}{\partial \theta'} = 0 \tag{189}$$

Now to correct the inconsistencies in phase and group velocities, the following change of variables is used:

$$\hat{t} = t + \beta r' \cos\theta' \tag{190}$$

$$\hat{r} = r' \tag{191}$$

$$\hat{\theta} = \theta' \tag{192}$$

where now,

$$\beta = \frac{M}{1 - M^2} = \frac{\sqrt{U_0^2 + V_0^2}}{1 - U_0^2 - V_0^2} \tag{193}$$

This leads to the equation

$$\frac{\partial \mathbf{u}'}{\partial \hat{t}} + \cos\hat{\theta}' \left[\frac{\partial(\mathbf{F}_1 - \bar{\mathbf{F}}_1)}{\partial \hat{r}'} + \beta \cos\hat{\theta}' \frac{\partial(\mathbf{F}_1 - \bar{\mathbf{F}}_1)}{\partial \hat{t}} \right]$$

$$- \frac{\sin\hat{\theta}'}{\hat{r}'} \left[\frac{\partial(\mathbf{F}_1 - \bar{\mathbf{F}}_1)}{\partial \hat{\theta}'} - \beta \hat{r}' \sin\hat{\theta}' \frac{\partial(\mathbf{F}_1 - \bar{\mathbf{F}}_1)}{\partial \hat{t}} \right]$$

$$+ \sin\hat{\theta}' \left[\frac{\partial(\mathbf{F}_2 - \bar{\mathbf{F}}_2)}{\partial \hat{r}'} + \beta \cos\hat{\theta}' \frac{\partial(\mathbf{F}_2 - \bar{\mathbf{F}}_2)}{\partial \hat{t}} \right]$$

$$+ \frac{\cos\hat{\theta}'}{\hat{r}'} \left[\frac{\partial(\mathbf{F}_2 - \bar{\mathbf{F}}_2)}{\partial \hat{\theta}'} - \beta \hat{r}' \sin\hat{\theta}' \frac{\partial(\mathbf{F}_2 - \bar{\mathbf{F}}_2)}{\partial \hat{t}} \right] = 0 \tag{194}$$

The rest of the derivation is carried out identically as in the derivation given in Section IV.1.1 with r, θ, and β_x replaced by r', θ', and β, respectively. The PML equations (129)–(131) in (r', θ') are then given by

$$\frac{\partial \mathbf{u}}{\partial t} + \sigma_{r'}\mathbf{q}_1 + \frac{1}{r'}\left(\int_{r'_0}^{r'} \sigma_{r'}\, dr'\right)\mathbf{q}_2 + \cos\theta' \frac{\partial(\mathbf{F}_1 - \bar{\mathbf{F}}_1)}{\partial r'} - \frac{\sin\theta'}{r'}\frac{\partial(\mathbf{F}_1 - \bar{\mathbf{F}}_1)}{\partial \theta'}$$

$$+\beta\sigma_{r'}\cos^2\theta'(\mathbf{F}_1 - \bar{\mathbf{F}}_1) + \beta\frac{\sin^2\theta'}{r'}\left(\int_{r'_0}^{r'} \sigma_{r'}\, dr'\right)(\mathbf{F}_1 - \bar{\mathbf{F}}_1) + \sin\theta'\frac{\partial(\mathbf{F}_2 - \bar{\mathbf{F}}_2)}{\partial r'}$$

$$+\frac{\cos\theta'}{r'}\frac{\partial(\mathbf{F}_2 - \bar{\mathbf{F}}_2)}{\partial \theta'} + \beta\sigma_{r'}\sin\theta'\cos\theta'(\mathbf{F}_2 - \bar{\mathbf{F}}_2)$$

$$-\beta\frac{\cos\theta'\sin\theta'}{r'}\left(\int_{r'_0}^{r'} \sigma_{r'}\, dr'\right)(\mathbf{F}_2 - \bar{\mathbf{F}}_2) = 0 \tag{195}$$

$$\frac{\partial \mathbf{q}_1}{\partial t} + \sigma_{r'}\mathbf{q}_1 + \cos\theta'\frac{\partial(\mathbf{F}_1 - \bar{\mathbf{F}}_1)}{\partial r'} + \beta\sigma_{r'}\cos^2\theta'(\mathbf{F}_1 - \bar{\mathbf{F}}_1) + \sin\theta'\frac{\partial(\mathbf{F}_2 - \bar{\mathbf{F}}_2)}{\partial r'}$$

$$+\beta\sigma_{r'}\sin\theta'\cos\theta'(\mathbf{F}_2 - \bar{\mathbf{F}}_2) = 0 \tag{196}$$

$$\frac{\partial \mathbf{q}_2}{\partial t} + \frac{1}{r'}\left(\int_{r'_0}^{r'} \sigma_{r'}\, dr'\right)\mathbf{q}_2 - \frac{\sin\theta'}{r'}\frac{\partial(\mathbf{F}_1 - \bar{\mathbf{F}}_1)}{\partial \theta'} + \beta\frac{\sin^2\theta'}{r'}\left(\int_{r'_0}^{r'} \sigma_{r'}\, dr'\right)(\mathbf{F}_1 - \bar{\mathbf{F}}_1)$$

$$+\frac{\cos\theta'}{r'}\frac{\partial(\mathbf{F}_2 - \bar{\mathbf{F}}_2)}{\partial \theta'} - \beta\frac{\cos\theta'\sin\theta'}{r'}\left(\int_{r'_0}^{r'} \sigma_{r'}\, dr'\right)(\mathbf{F}_2 - \bar{\mathbf{F}}_2) = 0 \tag{197}$$

At this point, all that remains is to rewrite the equations back in the original coordinates r and θ. This is easily carried out, and the resulting equations are

$$\frac{\partial \mathbf{u}}{\partial t} + \sigma_r\mathbf{q}_1 + \frac{1}{r}\left(\int_{r_0}^{r} \sigma_r\, dr\right)\mathbf{q}_2 + \cos(\theta-\phi)\frac{\partial(\mathbf{F}_1 - \bar{\mathbf{F}}_1)}{\partial r} - \frac{\sin(\theta-\phi)}{r}\frac{\partial(\mathbf{F}_1 - \bar{\mathbf{F}}_1)}{\partial \theta}$$

$$+\beta\sigma_r\cos^2(\theta-\phi)(\mathbf{F}_1-\bar{\mathbf{F}}_1) + \beta\frac{\sin^2(\theta-\phi)}{r}\left(\int_{r_0}^{r} \sigma_r\, dr\right)(\mathbf{F}_1-\bar{\mathbf{F}}_1) + \sin(\theta-\phi)\frac{\partial(\mathbf{F}_2 - \bar{\mathbf{F}}_2)}{\partial r}$$

$$+\frac{\cos(\theta-\phi)}{r}\frac{\partial(\mathbf{F}_2 - \bar{\mathbf{F}}_2)}{\partial \theta} + \beta\sigma_r\sin(\theta-\phi)\cos(\theta-\phi)(\mathbf{F}_2 - \bar{\mathbf{F}}_2)$$

$$-\beta\frac{\cos(\theta-\phi)\sin(\theta-\phi)}{r}\left(\int_{r_0}^{r} \sigma_r\, dr\right)(\mathbf{F}_2 - \bar{\mathbf{F}}_2) = 0 \tag{198}$$

$$\frac{\partial \mathbf{q}_1}{\partial t} + \sigma_r \mathbf{q}_1 + \cos(\theta-\phi)\frac{\partial(\mathbf{F}_1 - \bar{\mathbf{F}}_1)}{\partial r} + \beta\sigma_r \cos^2(\theta-\phi)(\mathbf{F}_1 - \bar{\mathbf{F}}_1) + \sin(\theta-\phi)\frac{\partial(\mathbf{F}_2 - \bar{\mathbf{F}}_2)}{\partial r}$$

$$+\beta\sigma_r \sin(\theta-\phi)\cos(\theta-\phi)(\mathbf{F}_2 - \bar{\mathbf{F}}_2) = 0 \tag{199}$$

$$\frac{\partial \mathbf{q}_2}{\partial t} + \frac{1}{r}\left(\int_{r_0}^{r} \sigma_r\, dr\right)\mathbf{q}_2 - \frac{\sin(\theta-\phi)}{r}\frac{\partial(\mathbf{F}_1 - \bar{\mathbf{F}}_1)}{\partial \theta} + \beta\frac{\sin^2(\theta-\phi)}{r}\left(\int_{r_0}^{r} \sigma_r\, dr\right)(\mathbf{F}_1 - \bar{\mathbf{F}}_1)$$

$$+\frac{\cos(\theta-\phi)}{r}\frac{\partial(\mathbf{F}_2 - \bar{\mathbf{F}}_2)}{\partial \theta} - \beta\frac{\cos(\theta-\phi)\sin(\theta-\phi)}{r}\left(\int_{r_0}^{r} \sigma_r\, dr\right)(\mathbf{F}_2 - \bar{\mathbf{F}}_2) = 0 \tag{200}$$

where, again,

$$\beta = \frac{\sqrt{U_0^2 + V_0^2}}{1 - U_0^2 - V_0^2} \tag{201}$$

and

$$\phi = \tan^{-1}\left(\frac{V_0}{U_0}\right) \tag{202}$$

Notice that since r and r' are equivalent and σ_r is a function of r only, σ_r and $\sigma_{r'}$ are also equivalent. Notice also that the system can be reduced down to two variables by enforcing the relationship (119). It is also easy to see that if $V_0 = 0$, equations (198)–(200) reduce to the equations derived for one-dimensional mean flow (129)–(131).

IV.3.3 PML FOR LINEARIZED EULER EQUATIONS IN PRIMITIVE VARIABLES

The PML boundary condition for the linearized Euler equations in cylindrical coordinates (152) can also be reformulated to accommodate the case of an oblique mean flow (U_0, V_0), where, again, U_0 and V_0 are related to $\bar{v}_r$ and $\bar{v}_\theta$ by (154)–(155). In order to align the horizontal axis with the direction of mean flow, the following change of variables is again used:

$$r' = r \tag{203}$$

$$\theta' = \theta - \phi \tag{204}$$

where

$$\phi = \tan^{-1}\left(\frac{V_0}{U_0}\right) \tag{205}$$

The governing equation (152) then becomes

$$\frac{\partial \mathbf{u}}{\partial t} + \mathsf{A}(\theta')\frac{\partial \mathbf{u}}{\partial r'} + \frac{1}{r'}\mathsf{B}(\theta')\frac{\partial \mathbf{u}}{\partial \theta'} + \frac{1}{r'}\mathsf{C}(\theta')\mathbf{u} = 0 \tag{206}$$

where $\mathsf{A}(\theta')$, $\mathsf{B}(\theta')$, and $\mathsf{C}(\theta')$ are the same as those given in (153) with θ replaced by θ' and mean flow (U_0, V_0) now given by $(M, 0)$. Because the mean flow $(M, 0)$ in the (r', θ') coordinate system is one-dimensional, the usual transformation is chosen to align phase and group velocities, specifically,

$$\hat{t} = t + \beta r' \cos\theta' \tag{207}$$

$$\hat{r} = r' \tag{208}$$

$$\hat{\theta} = \theta' \tag{209}$$

where

$$\beta = \frac{M}{1 - M^2} = \frac{\sqrt{U_0^2 + V_0^2}}{1 - U_0^2 - V_0^2} \tag{210}$$

The remainder of the derivation exactly mimics the steps carried out in Section IV.2.1 with r, θ, and β_x replaced by r', θ', and β, respectively. The PML equations (174)–(176) in (r', θ') are therefore given by

$$\frac{\partial \mathbf{u}}{\partial t} + \sigma_{r'}\mathbf{q}_1 + \frac{1}{r'}\left(\int_{r'_0}^{r'} \sigma_{r'}\, dr'\right)\mathbf{q}_2 + \mathsf{A}(\theta')\left[\frac{\partial \mathbf{u}}{\partial r'} + \beta\sigma_{r'}\cos\theta'\mathbf{u}\right]$$
$$+\frac{1}{r'}\mathsf{B}(\theta')\left[\frac{\partial \mathbf{u}}{\partial \theta'} - \beta\left(\int_{r'_0}^{r'} \sigma_{r'}\, dr'\right)\sin\theta'\mathbf{u}\right] + \frac{1}{r'}\mathsf{C}(\theta')\mathbf{u} = 0 \tag{211}$$

$$\frac{\partial \mathbf{q}_1}{\partial t} + \sigma_{r'}\mathbf{q}_1 + \mathsf{A}(\theta')\left[\frac{\partial \mathbf{u}}{\partial r'} + \beta\sigma_{r'}\cos\theta'\mathbf{u}\right] = 0 \tag{212}$$

$$\frac{\partial \mathbf{q}_2}{\partial t} + \frac{1}{r'}\left(\int_{r'_0}^{r'} \sigma_{r'}\, dr'\right)\mathbf{q}_2 + \frac{1}{r'}\mathsf{B}(\theta')\left[\frac{\partial \mathbf{u}}{\partial \theta'} - \beta\left(\int_{r'_0}^{r'} \sigma_{r'}\, dr'\right)\sin\theta'\mathbf{u}\right] + \frac{1}{r'}\mathsf{C}(\theta')\mathbf{u} = 0 \tag{213}$$

Finally, the equations are converted back to the original coordinates, r and θ, and become

$$\frac{\partial \mathbf{u}}{\partial t} + \sigma_r \mathbf{q}_1 + \frac{1}{r}\left(\int_{r_0}^{r} \sigma_r \, dr\right) \mathbf{q}_2 + \mathsf{A}(\theta)\left[\frac{\partial \mathbf{u}}{\partial r} + \beta\sigma_r \cos(\theta - \phi)\mathbf{u}\right]$$

$$+\frac{1}{r}\mathsf{B}(\theta)\left[\frac{\partial \mathbf{u}}{\partial \theta} - \beta\left(\int_{r_0}^{r} \sigma_r \, dr\right)\sin(\theta - \phi)\mathbf{u}\right] + \frac{1}{r}\mathsf{C}(\theta)\mathbf{u} = 0 \tag{214}$$

$$\frac{\partial \mathbf{q}_1}{\partial t} + \sigma_r \mathbf{q}_1 + \mathsf{A}(\theta)\left[\frac{\partial \mathbf{u}}{\partial r} + \beta\sigma_r \cos(\theta - \phi)\mathbf{u}\right] = 0 \tag{215}$$

$$\frac{\partial \mathbf{q}_2}{\partial t} + \frac{1}{r}\left(\int_{r_0}^{r} \sigma_r \, dr\right) \mathbf{q}_2 + \frac{1}{r}\mathsf{B}(\theta)\left[\frac{\partial \mathbf{u}}{\partial \theta} - \beta\left(\int_{r_0}^{r} \sigma_r \, dr\right)\sin(\theta - \phi)\mathbf{u}\right] + \frac{1}{r}\mathsf{C}(\theta)\mathbf{u} = 0 \tag{216}$$

where

$$\beta = \frac{\sqrt{U_0^2 + V_0^2}}{1 - U_0^2 - V_0^2} \tag{217}$$

and

$$\phi = \tan^{-1}\left(\frac{V_0}{U_0}\right) \tag{218}$$

Here the mean flow has been rewritten in terms of the original coordinates as (U_0, V_0). Again, the equations are not independent because of the relationship (167) between $\mathbf{u}$, $\mathbf{q}_1$, and $\mathbf{q}_2$. Therefore, only two variables need to be stored at implementation. Upon setting $V_0 = 0$ in (214)–(216), the equations (174)–(176) are recovered as expected.

CHAPTER V

CONCLUDING REMARKS

With steps being taken to improve the accuracy of solutions in the interior domain, the importance of improving accuracy at the boundary also continues to increase. With the Perfectly Matched Layer, it has been possible to derive high-accuracy boundary conditions that in turn preserve accuracy in the interior of the domain. In this work, Perfectly Matched Layer absorbing boundary conditions have been presented for the linearized and nonlinear Euler equations for an oblique mean flow and have also been adapted for use in a cylindrical coordinate system. The PML equations have been shown to be stable and have produced satisfactory numerical results. Further, the capability of PML for use with an oblique mean flow and cylindrical coordinates, as presented in this work, allows for a number of new configurations to be tested numerically. It also serves as a basis for the derivation of PML for increasingly realistic configurations. As the number of applicable problems increases, the Perfectly Matched Layer as a nonreflecting boundary condition should continue to gain acceptance as the method of choice.

In comparison with other nonreflecting boundary conditions, the Perfectly Matched Layer can be considered superior on multiple levels. The biggest advantage is that of improved accuracy. Because the boundary conditions are exactly matched to the governing equations, reflection errors originating from numerical boundaries are greatly decreased, and in turn, overall errors are much smaller. While the accuracy of characteristic boundary conditions is comparable to that of PML in the case where waves exit the domain normal to the boundary or at small angles of incidence, that accuracy quickly diminishes as the angle of incidence is increased. Therefore, the case of oblique mean flow is much better handled with the Perfectly Matched Layer. Another advantage of PML is increased efficiency, particularly in comparison to asymptotic boundary conditions and absorbing zone approaches. Because asymptotic boundary conditions are based on solutions occurring far from the source, domains must be kept large enough to validate the use of such solutions, or the accuracy of the solutions will suffer. Absorbing zone domains are often larger than PML domains as well because solutions in the absorbing zone must be altered very gradually in order to prevent reflections from occurring within the absorbing zone itself.

Further, in comparison to other PML methods that have been introduced in previous works, the approaches presented in this work can also be considered more comprehensive. First, the PML boundary conditions are not limited to the case of normal mean flow but accommodate a mean flow at any angle in relation to the numerical boundary. Second, for the formulation in Cartesian coordinates, a proper treatment has been given for the necessary corner layers, which has not been done in previous attempts to handle an oblique mean flow. Such a treatment has been shown to be stable. The PML equations have also been formulated to handle all three types of waves supported by the Euler equations, rather than focusing on a single type of exiting wave. Furthermore, the Perfectly Matched Layer has also been derived for cylindrical coordinates, an important capability in the handling of many physical situations.

Since the PML equations formulated for Cartesian coordinates and those given for cylindrical coordinates are both capable of absorbing waves traveling with an oblique mean flow, there are several things to consider when choosing between the two formulations. To start, it is clear that the geometry under investigation is an important factor in choosing one of the two formulations. The cylindrical equations might intuitively be chosen if the physical problem involves a circular cylinder or any other radially symmetric object. However, when using a cylindrical grid, an overset grid approach is often necessary to maintain appropriate grid spacing at distances farther from the origin of the coordinate system. The need for overset grids adds complication when programming the system. In this case, it may be just as effective to choose the formulation for Cartesian coordinates.

In an alternate sense, however, the cylindrical PML formulation may be considered simpler in its use of only an r-layer equation, as opposed to the need for x-, y-, and corner layers. Furthermore, there is no concern about the interfaces between side and corner layers, which themselves can be a cause of wave reflections. The need to examine the stability of corner layer equations is also eliminated with the use of cylindrical coordinates. Therefore, the choice to use a cylindrical coordinate system versus a Cartesian coordinate system, or vice-versa, could to some extent be viewed as a trade-off between simplicity of derivation and simplicity of implementation.

Regardless of the coordinate system chosen, the Perfectly Matched Layer has been shown, in this and other works, to be an accurate nonreflecting boundary condition. Whether dealing with linear or nonlinear problems, PML has proven effective in

the absorption of outgoing waves, as numerical results in the present work have demonstrated.

Finally, it is important to point out that despite having accomplished the initial motivating goals, the present work is not entirely comprehensive in its handling of physical systems. First, having derived the PML for the Euler equations only, examples are limited to inviscid flow. At present, the PML have not been given to accommodate problems involving viscosity, mass diffusion, or thermal conductivity, as would be supported by the Navier-Stokes equations. The focus of this work has also been on the two-dimensional problem. Clearly, in most practical situations, three dimensions must be considered. Further, only a linear stability analysis has been provided. Such limitations, however, serve as a motivation for future work, which could include formulating the PML for the three-dimensional Navier-Stokes equations with an oblique mean flow. Even more generally, considerations could be made for a nonuniform mean flow, and various coordinate systems could again be examined. A more complete analysis of stability would also be ideal, with further consideration given to the nonlinear problem. Despite its limitations, however, the present work provides a solid framework for future endeavors in formulating a Perfectly Matched Layer that accommodates more of the complexities found in the physical world.

BIBLIOGRAPHY

[1] Anderson, J. D., Degrez, G., Dick, E., Grundmann, R., Wendt, J. F., "Governing Equations of Fluid Dynamics," *Computational Fluid Dynamics: An Introduction*, 2nd ed., Springer, 1996, pp. 15–51.

[2] Thompson, K. W., "Time Dependent Boundary Conditions for Hyperbolic Systems," *Journal of Computational Physics*, Vol. 68, 1987, pp. 1–24.

[3] Giles, M. B., "Nonreflecting Boundary Conditions for Euler Equations Calculations," *AIAA Journal*, Vol. 28, 1990, pp. 2050–2058.

[4] Poinsot, T., and Lele, S. K., "Boundary conditions for direct simulation of compressible viscous flows," *Journal of Computational Physics*, Vol. 101, 1992, pp. 104–129.

[5] Thompson, K. W., "Time Dependent Boundary Conditions for Hyperbolic Systems, II," *Journal of Computational Physics*, Vol. 89, 1990, pp. 439–461.

[6] Schulze, D., "Far Field Boundary Conditions Based on Characteristic and Bicharacteristic Theory Applied to Transonic Flows," *Fourteenth International Conference on Numerical Methods in Fluid Dynamics*, Vol. 453, Springer, Berlin, 1995, pp. 211–215.

[7] Kim, J. W., and Lee, D. J., "Generalized Characteristic Boundary Conditions for Computational Aeroacoustics," *AIAA Journal*, Vol. 38, 2000, pp. 2040–2049.

[8] Bayliss, A., and Turkel, E., "Radiation Boundary Conditions for Wave-Like Equations," *Communications on Pure and Applied Mathematics*, Vol. 33, 1980, pp. 707–725.

[9] Engquist, B., and Majda, A., "Radiation Boundary Conditions for Acoustic Equations and Elastic Wave Calculations," *Communications on Pure and Applied Mathematics*, Vol. 32(3), 1979, pp. 313–357.

[10] Hagstrom, T., and Hariharan, S. I., "Accurate Boundary Conditions for Exterior Problems in Gas Dynamics," *Mathematics of Computation*, Vol. 51, Oct.1988, pp. 581–597.

[11] Tam, C. K. W., and Webb, J. C., "Dispersion-Relation-Preserving Finite Difference Schemes for Computational Acoustics," *Journal of Computational Physics*, Vol. 107, 1993, pp. 262–281.

[12] Rudy, D. H., and Strikwerda, J. C., "A Non-Reflecting Outflow Boundary Condition for Subsonic Navier-Stokes Calculations," *Journal of Computational Physics*, Vol. 36, 1980, pp. 55–70.

[13] Rudy, D. H., and Strikwerda, J. C., "Boundary Conditions for Subsonic Compressible Navier-Stokes Calculations," *Computers and Fluids*, Vol. 9, 1981, pp. 327–338.

[14] Rai, M. M., and Moin, P., "Direct Simulations of Turbulent Flow Using Finite-Difference Schemes," *Journal of Computational Physics*, Vol. 96, 1991, pp. 15–53.

[15] Colonius, T., Lele, S. K., and Moin, P., "Boundary Conditions for Direct Computation of Aerodynamic Sound Generation," *AIAA Journal*, Vol. 31, 1993, pp. 1574–1582.

[16] Visbal, M. R., and Gaitonde, D. V., "Very High-Order Spatially Implicit Schemes for Computational Acoustics on Curvilinear Meshes," *Journal of Computational Acoustics*, Vol. 9 (4), 2001, pp. 1259–1286.

[17] Liu, C., and Liu, Z., "High Order Finite Difference and Multigrid Methods for Spatially Evolving Instability in a Planar Channel," *Journal of Computational Physics*, Vol. 106, 1993, pp. 92–100.

[18] Israeli, M., and Orszag, S. A., "Approximation of Radiation Boundary Conditions," *Journal of Computational Physics*, Vol. 41, 1981, pp. 115–135.

[19] Freund, J. B., "Proposed Inflow/Outflow Boundary Condition for Direct Computation of Aerodynamic Sound," *AIAA Journal*, Vol. 35, No. 4, 1997, pp. 740–742.

[20] Kosloff, R., and Kosloff, D., "Absorbing Boundaries for Wave Propagation Problems," *Journal of Computational Physics*, Vol. 63, 1986, pp. 363–376.

[21] Bodony, D. J., "Analysis of Sponge Zones for Computational Fluid Mechanics," *Journal of Computational Physics*, Vol. 212, 2006, pp. 681–702.

[22] Streett, C. L., and Macaraeg, M. G., "Spectral Multi-Domain for Large-Scale Fluid Dynamic Simulations," *Applied Numerical Mathematics*, Vol. 6, 1989, pp. 123–139.

[23] Ta'asan, S., and Nark, D. M., "An Absorbing Buffer Zone Technique of Acoustic Wave Propagation," AIAA Paper 95-0164, 1995.

[24] Berenger, J.-P., "A Perfectly Matched Layer for the Absorption of Electromagnetic Waves," *Journal of Computational Physics*, Vol. 114, 1994, pp. 185–200.

[25] Becache, E., Fauqueux, S., and Joly, P., "Stability of Perfectly Matched Layers, Group Velocities and Anisotropic Waves," *Journal of Computational Physics*, Vol. 188, 2003, pp. 399–433.

[26] Becache, E., Bonnet-Ben Dhia, and A.-S., Legendre, G., "Perfectly Matched Layers for the Convective Helmholtz Equation," *SIAM Journal of Numerical Analysis*, Vol. 42, 2004, pp. 409–433.

[27] Hagstrom, T., and Nazarov, I., "Absorbing Layers and Radiation Boundary Conditions for Jet Flow Simulations," AIAA Paper 2002-2606, 2002.

[28] Hagstrom, T., and Nazarov, I., "Perfectly Matched Layers and Radiation Boundary Conditions for Shear Flow Calculations," AIAA Paper 2003-3298, 2003.

[29] Hu, F. Q., "On Absorbing Boundary Conditions for Linearized Euler Equations by a Perfectly Matched Layer," *Journal of Computational Physics*, Vol. 129, 1996, pp. 201–219.

[30] Hu, F. Q., "A Stable, Perfectly Matched Layer for Linearized Euler Equations in Unsplit Physical Variables," *Journal of Computational Physics*, Vol. 173, 2001, pp. 455–480.

[31] Hu, F. Q., "A Perfectly Matched Layer Absorbing Boundary Condition for Linearized Euler Equations with a Non-Uniform Mean Flow," *Journal of Computational Physics*, Vol 208, 2005, pp. 469–492.

[32] Hu, F. Q., "On the Construction of PML Absorbing Boundary Condition for the Non-Linear Euler Equations," AIAA Paper 2006-0798, 2006.

[33] Hu, F. Q., Li, X. D., and Lin, D. K., "PML Absorbing Boundary Condition for Non-Linear Aeroacoustics Problems," AIAA Paper 2006-2521, 2006.

[34] Parrish, S. A., and Hu, F. Q., "PML Absorbing Boundary Conditions for the Linearized and Nonlinear Euler Equations in the Case of Oblique Mean Flow," *International Journal for Numerical Methods in Fluids*, 2007, in review.

[35] Parrish, S. A., and Hu, F. Q., "Application of PML Absorbing Boundary Condition to Aeroacoustics Problems," AIAA Paper 2007-3509, 2007.

[36] Collino, F., and Monk, P., "The Perfectly Matched Layer in Curvilinear Coordinates," *SIAM Journal of Scientific Computing*, Vol. 19, 1998, pp. 2061–2090.

[37] Collino, F., and Monk, P., "Optimizing the Perfectly Matched Layer," *Computer Methods in Applied Mechanics and Engineering*, Vol. 164, 1998, pp. 157–171.

[38] Gedney, S. D., "Anisotropic Perfectly Matched Layer-Absorbing Medium for the Truncation of FDTD Lattices," *IEEE Transactions on Antennas and Propagation*, Vol. 44, No. 12, 1996, pp. 1630–1639.

[39] Petropoulos, P. G., "Reflectionless Sponge Layers as Absorbing Boundary Conditions for the Numerical Solution of Maxwell Equations in Rectangular, Cylindrical, and Spherical Coordinates," *SIAM Journal on Applied Mathematics*, Vol. 60, No. 3, 2000, pp. 1037–1058.

[40] Zhao, L., and Cangellaris, A. C., "GT-PML: Generalized Theory of Perfectly Matched Layers and Its Application to the Reflectionless Truncation of Finite-Difference Time-Domain Grids," *IEEE Transactions on Microwave Theory and Techniques*, Vol. 34, 1996, pp. 2555–2563.

[41] Zhao, L. and Cangellaris, A. C., "A General Approach for the Development of Unsplit-Field Time-Domain Implementation of Perfectly Matched Layers for FD-TD Grid Truncation," *IEEE Microwave and Guided Wave Letters*, Vol. 6, No. 5, May 1996, pp. 209–211.

[42] Appelo, D., Hagstrom, T., and Kreiss, G., "Perfectly Matched Layers for Hyperbolic Systems: General Formulation, Well-Posedness and Stability," *SIAM Journal of Applied Mathematics*, Vol. 67, 2006, pp. 1–23.

[43] Diaz, J., and Joly, P., "A Time Domain Analysis of PML Models in Acoustics," *Computational Methods in Applied Mechanics and Engineering*, Vol. 195, 2006, pp. 3820–3853.

[44] Nataf, F.,"A New Approach to Perfectly Matched Layers for the Linearized Euler System," *Journal of Computational Physics*, Vol. 214, 2006, pp. 757–772.

[45] Hu, F. Q., "Boundary Conditions: Acoustics," In: Wagner, C. A., Hüttl, T., and Sagaut, P., editors, *Large-Eddy Simulations for Acoustics*, Cambridge, New York, 2007, pp. 216–222.

[46] Hu, F. Q., and Atkins, H. L., "A Discrete Analysis of Non-Reflecting Boundary Conditions for Discontinuous Galerkin Method," AIAA Paper 2003-3301, 2003.

[47] Hu, F. Q., Hussaini, M. Y., and Manthey, J. L., "Low-Dissipation and Low-Dispersion Runge-Kutta Schemes for Computational Acoustics," *Journal of Computational Physics*, Vol. 124, 1996, pp. 177–191.

[48] Tam, C. K. W., and Hu, F. Q., "An Optimized Multi-Dimensional Interpolation Scheme for Computational Aeroacoustics Applications Using Overset Grids," AIAA Paper 2004-2812, 2004.

[49] Baysal, O., Fouladi, K., Lessard, V.R., "Multigrid and Upwind Viscous Flow Solver on 3-D Overlapped and Embedded Grids," *AIAA Journal*, Vol. 29, No. 6, June 1991, pp. 903–910.

[50] Baysal, O., Fouladi, K., Leung, R. W., Sheftic, J.S., "Interference Flows Past Cylinder-Fin-String-Cavity Assemblies," *Journal of Aircraft*, Vol. 29, No. 2, Mar./Apr. 1992, pp. 194–202.

[51] Fouladi, K., and Baysal, O., "Viscous Simulation Method for Unsteady Flows Past Multicomponent Configuration," *Journal of Fluids Engineering*, Vol. 114, No. 2, June 1992, pp. 161–169.

VITA

Sarah Anne Parrish
Department of Mathematics and Statistics
Old Dominion University
Norfolk, VA 23529

Education

B.S. Mathematics, Minor in Computer Science, Old Dominion University, 2004
M.S. Computational and Applied Mathematics, Old Dominion University, 2005

Awards and Honors

Governor's Technology Scholarship (2000-2004)
Frieda Young Science and Engineering Prize (2002)
Outstanding Junior, ODU Chapter of the Honor Society of Phi Kappa Phi (2003)
Honors College Award for Academic Excellence (2004)
Alumni Award for the College of Sciences (December 2004)
Dominion Graduate Scholar Award (2004-2005)
Philip R. Wohl Scholarship (2007)

Publications and Presentations

Parrish, S. A., and Hu, F. Q., "PML Absorbing Boundary Conditions for the Linearized and Nonlinear Euler Equations in the Case of Oblique Mean Flow," *International Journal for Numerical Methods in Fluids*, 2007, in review.

Parrish, S. A., and Hu, F. Q., "Construction of Perfectly Matched Layer in Cylindrical Coordinates with Nonzero Mean Flow," APS 60th Annual Meeting of the Division of Fluid Dynamics, Salt Lake City, Utah, November 2007.

Parrish, S. A., and Hu, F. Q., "Application of PML Absorbing Boundary Condition to Aeroacoustics Problems with an Oblique Mean Flow," 28th AIAA Aeroacoustics Conference, AIAA Paper 2007-3509, 2007.

Hu, F. Q., and Parrish, S. A., "On Developing a PML Absorbing Boundary Condition for Computational Aeroacoustics with Oblique Mean Flow," 35th International Congress and Exposition on Noise Control Engineering, Honolulu, Hawaii, December 2006.

Typeset using LaTeX.